UNIVERSITY OF CALIFORNIA,

IRVINE

Faceted Σ11 Grain Boundaries: Unique Migration Mechanisms and the Effects of Alloying

DISSERTATION

submitted in partial satisfaction of the requirements

for the degree of

DOCTOR OF PHILOSOPHY

in Materials and Manufacturing Technology

by

Megan J. McCarthy

Dissertation Committee
Professor Timothy J. Rupert, Chair
Professor Penghui Cao
Professor Lorenzo Valdevit

2021

COPYRIGHT

Sections of this dissertation have been previously published and are re-used here with appropriate permissions:

DEDICATION

To my grandmother Barbara Jeanne Smith and the women of her generation, who had the curiosity, drive, and intellect to thrive in higher education and beyond but had to battle long and hard for the opportunity.

To my wonderful, caring, and extremely patient spouse, who has kept me laughing and grounded through career changes, intercontinental moves, and of course, graduate school.

To all my other incredible family members here and overseas, especially my parents and parents-in-law. You have been an unfailing source of support, love, and inspiration through all the various phases of my education.

TABLE OF CONTENTS

LIST OF TABLES

LIST OF FIGURES

Chapter 1

Chapter 2

ACKNOWLEDGMENTS

First and foremost, I thank my advisor and mentor Professor Tim Rupert, for giving me this incredible opportunity to become a scientist. With his unwavering support and guidance, I have been able to accomplish so much more than I ever thought possible. His enthusiasm for science, dynamism, and generosity are a constant source of inspiration for me and so many others. It has been a true honor to work with him.

I would also like to express my gratitude to the members of my dissertation committee, Professor Penghui Cao and Professor Lorenzo Valdevit. Thank you both for your time and your valuable insights into my work. Professor Valdevit, as the director of my program of study, thank you as well for your scientific and professional mentorship over my time at UCI.

None of this work would have been possible without the high-performance computing center on our campus. I thank all of the very hard-working staff members who have helped me both solve technical issues as well as improve my research efficiency over the years.

Last but certainly not least, I am very thankful to my fellow graduate students and postdocs for all the stimulating conversation, moral support, and fun times that they have given me along the way. A special thanks goes to my excellent lab mates, both past and present. It has been a genuine pleasure working with all of you, and I couldn't have asked for better colleagues.

CURRICULUM VITAE

Megan J. McCarthy

EDUCATION

Ph.D. Materials and Manufacturing Technology 2021
Henry Samueli School of Engineering, University of California, Irvine

M.S. Materials and Manufacturing Technology 2019
Henry Samueli School of Engineering, University of California, Irvine

B.S. Coursework, General Engineering Science 2013 – 2016
Hamburg University of Technology, Hamburg, Germany

B.A. Music Performance in Percussion (minor: Linguistics) 2008
California State University, Long Beach

PUBLICATIONS

McCarthy MJ, Rupert TJ. "Alloying induces directionally-dependent mobility and alters migration mechanisms of faceted grain boundaries". Scripta Materialia **194**, 2021.

McCarthy MJ, Rupert TJ. "Shuffling mode competition leads to directionally-anisotropic mobility of faceted Σ11 boundaries in face centered cubic metals". Physical Review Materials **4**, 2020.

McCarthy MJ, Rupert TJ. "Emergence of directionally-anisotropic mobility in a faceted Σ11 <110> tilt grain boundary in Cu". Modelling and Simulation in Materials Science and Engineering **28**, 2020.

CONFERENCE TALKS

McCarthy MJ, Rupert TJ. "Directionally-anisotropic Mobility of Faceted Boundaries Explained through Interfacial Dislocation Mechanisms". Materials Science & Technology (MS&T), November 2020, Virtual (pre-COVID: Pittsburgh PA).

McCarthy MJ, Rupert TJ. "Anisotropic Mobility in Faceted Σ11 <110> tilt FCC Grain Boundaries and the Effect of Subsequent Doping". The Minerals, Metals, and Materials Society (TMS) Annual Meeting and Exhibition, February 2020, San Diego CA.

McCarthy MJ, Rupert TJ. "Anisotropic mobility of faceted Σ11 <110> tilt grain boundaries in face-centered cubic metals". Materials Science & Technology (MS&T), September 2019, Portland OR.

ABSTRACT OF THE DISSERTATION

Faceted Σ11 grain boundaries: Unique Migration Mechanisms and the Effects of Alloying

by

Megan J. McCarthy

Doctor of Philosophy in Materials and Manufacturing Technology

University of California, Irvine, 2021

Associate Professor Timothy J. Rupert, Chair

Faceted grain boundaries, where grain boundary area is increased in the name of producing low-energy segments, have unique energetic properties and defect structures that have yielded important insights into grain boundary structure-property relationships. However, less information exists about their dynamic behavior. What is known shows that faceted boundaries may impact microstructure evolution in unexpected ways. Recent research showing a variety of faceted Σ3 boundaries in Ni to exhibit new migration trends, motivating a deeper study of other faceted boundary systems. The faceted Σ11 tilt boundaries represent a promising but as yet unexplored set of interfaces with have highly asymmetric, unique geometries, which suggests that they may have similarly unique migration mechanisms and segregation tendencies. The first part of this dissertation is dedicated to exploring this possibility in pure face-centered cubic materials. Molecular dynamics studies across a range of different faceted Σ11 <110> tilt boundaries in Cu and Ni are performed. It is revealed that these boundaries' mobilities are strongly dependent on the direction of the applied driving force, a phenomenon we name *directionally-anisotropic mobility*. This effect generally becomes smaller, but does not disappear completely, as temperature is increased. In contrast, the same faceted bicrystals in Al demonstrate similar mobilities in either direction, illustrating that directionally-anisotropic mobility is a material-dependent phenomenon.

An atomistic migration mechanism related to stacking fault energy is identified as an important mediator of a rate-limiting process. The second part of this dissertation expands the study of faceted Σ11 boundaries to alloy systems. Facet-specific segregation trends are systematically studied through changes in temperature and composition. In the Cu-Ag system, site-specific segregation is found to be related to excess volume and a local tension-compression field discontinuity introduced by the emission of Shockley partial dislocations near facet junctions. Additional mobility simulations using a high-temperature, dilute variant reveals that solute atoms can induce directionally-anisotropic mobility. Finally, similar studies conducted in multi-principal element alloys reveal strong intrinsic segregation tendencies, even up to 90% of the melting temperature of the alloy. A spatial analysis of the elemental composition near facets reveals regions of enrichment beyond what is typically considered a part of the grain boundary structure.

1 Introduction

1.1 Grain boundary character

Interest in accurately modeling microstructure evolution has been a primary goal of materials science for many decades. However, it has proven to be a challenging undertaking, even for seemingly simple phenomena such as grain growth in single phase materials. Initial analytical models of grain growth were developed based on the concept of curvature-driven migration [7–9]. This idea was based on the assumption that the interfacial energy between any two grains is a constant value, meaning that the surface area determines the net energy of the system. Energy can thus be lowered by reducing the overall surface area of the interfacial network, which in a polycrystalline material also means increasing the size of each crystallite. However, these initial models failed to replicate the behavior of real materials [8]. The reason for this was brought to light thanks to advances in theoretical knowledge of crystalline lattices and in the field of electron microscopy, which gave scientists insight into the frequently highly-structured nature of grain boundaries on the atomic scale. Before this point, scientists had believed that grain boundaries were essentially unstructured, or possibly liquid-like [3]. It was soon recognized that each individual grain boundary within polycrystalline microstructures had its own kinetic and thermodynamic character that needs to be accounted for in models of grain growth.

As the importance of individual grain boundaries became apparent, the need for a consistent naming convention for them did as well. A natural way of accomplishing this was to look to the crystallographic relationship between the two grains of a grain boundary. The two crystal lattices of the constituent grains have the same pattern (the unit cell of the material) but are rotated at some angle to one another. At certain angles, some of the lattice sites from both crystals overlap perfectly, creating a superlattice. The grain boundary can then be interpreted as the

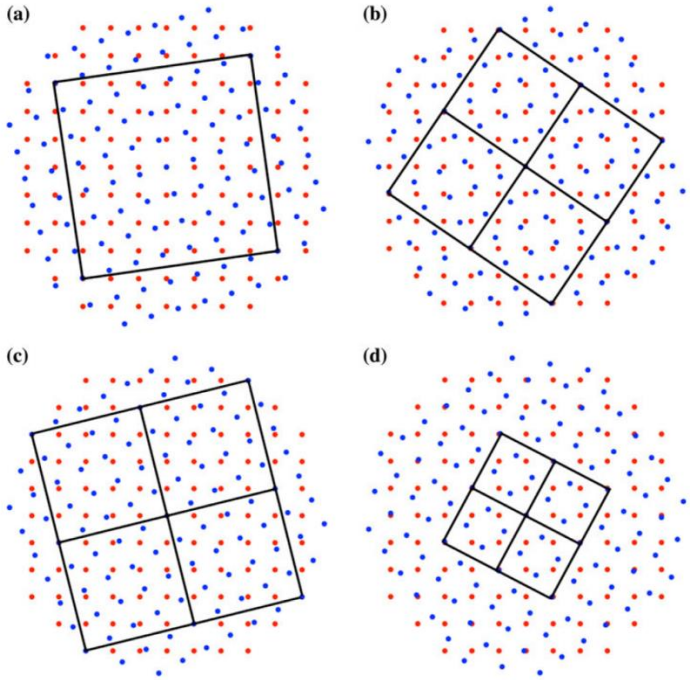

Figure 28.1. Figure from Rohrer *[3]*. Coincident site lattice (CSL) configurations obtained by rotations of the blue square lattice around a common [001] tilt axis normal to the plane of the paper. A CSL is defined as the superlattice formed where the blue and red dots overlap and is outlined in black lines for each rotation. a) Σ25 at 16° b) Σ13 at 22° c) Σ17 at 28° d) Σ5 at 36°.

physical structure corresponding to a plane that contains all the points of the generated superlattice. This is the basic principle behind one of the most common grain boundary characterization methods used up to this day, called the coincidence site lattice (CSL) concept. In its most basic form, this convention labels grain boundaries through a ratio that describes the degree of coincidence between the neighboring grain's lattices, called the Σ value. To determine Σ, one first finds the number of non-overlapping lattice sites (counted from one reference grain) found within the unit cell of the larger superlattice structure and divides that by the number of coinciding sites that make the superlattice. Four examples from Rohrer [3] of coincidence site lattices (blue and red dots) and their superlattices (black squares) in a simple square lattice are shown in Figure 1.1.

In two dimensions (2D), the angle of rotation of one crystal lattice from the other that is required to generate a certain value of Σ is described by one angle, called the *misorientation* or

misorientation angle. However, in three dimensions (3D), boundaries require five independent angles to be uniquely described, also called the five macroscopic degrees of freedom. With five different angles, rotations are far more complex to describe and imagine. The CSL naming convention accounts for this by including the axis of rotation (and sometimes the angle) to describe the lattice misorientation. However, this description only accounts for the first three of the five angular degrees of freedom. The last two angles, collectively called the boundary plane orientation, define the direction of the grain boundary plane normal relative to the rotation axis. They include the *azimuthal angle*, α, and the *inclination angle,* β (also called the polar angle). There are three terms used as a shorthand to describe the grain boundary plane orientations: *tilt*, *twist,* and *mixed.* In tilt boundaries, the azimuthal angle is fixed to be parallel to the misorientation axis of the crystal, and inclination angle can vary. Twist boundaries have the inclination angle fixed perpendicular to the rotation axis and can freely vary the azimuthal angle. Mixed boundaries are, as the name implies, ones in which both boundary plane orientations can vary arbitrarily.

By convention, the boundary plane orientation always corresponds to the highest-symmetry plane (i.e., the plane with the shortest distance between coincident sites in the coinciding superlattice). These planes, which we will refer to as the *symmetric boundary plane* (SBP) have important properties that make them highly worthy of study. They characteristically have very simple structures, and this simplicity has made them critical to the development of theoretical models of grain boundary morphology, such as the structural unit model [7]. However, researchers have increasingly recognized the need to investigate the wide range of *asymmetric* boundaries that can also be generated from a single CSL structure [10–14]. For example, it has been established multiple times that there exists no general connection between properties such as energy and CSL misorientation alone (i.e. the symmetric grain boundary plane) [3, 15, 16]. By including not only

misorientation but also variations in the boundary plane inclination angle, researchers have been able to uncover clear trends in properties such as energy, mobility, and excess volume [17, 18]. These results underscore the fact that all five macroscopic degrees of freedom must be systematically varied in the search for grain boundary structure-property relationships.

The CSL naming convention for grain boundaries is relatively simple, and yet still a powerful means of reducing the enormous complexity of the 5D grain boundary parameter space to a far more manageable size. However, it has important limitations that have affected the trajectory of grain boundary research over time. By its nature, it brings attention exclusively to grain misorientations with coinciding lattices, and especially ones with what are considered low Σ values (< 29). Boundaries in that category often referred to as "special" grain boundaries. However, real grain boundary structures have highly random distributions of grain orientations [19, 20], only a fraction of which can be considered special in that definition. Though adjustments have been made to improve the CSL model's generality, such as the Brandon criteria to identify near-Σ misorientations [21], focus on CSL nevertheless comes at the expense of understanding boundaries with misorientations outside of this schema. One example are *incommensurate boundaries*, which are interfaces with irrational plane spacings, such as {111}/{110}. Because such planes have no coincident sites, they are not described by the CSL convention, but several have been of interest due to acting as examples of quasiperiodicity [22], having unusual defect structure [22, 23], and exhibiting supergliding behavior [24, 25]. In a recently-published work designed to address this gap, Kuhr and Farkas [26] have begun a systematic analysis of the dislocation distribution and character in random high-angle grain boundaries.

Even adjustments to the CSL naming convention cannot change its nature as a purely geometric characterization method. Robust descriptions of grain boundary character and behavior require taking into account the influence of global material properties and thermodynamic parameters. Due to the extra free volume contained at interfaces, grain boundary atoms have a greater range of motion than atoms within the bulk. This collective set of different atomic configurations are called the microscopic degrees of freedom of a grain boundary. Variations in system energy determine how the microscopic degrees of freedom are expressed at any given moment. This means that interfaces with the same name frequently have major structural differences between them. This is perhaps not surprising when observed between two different materials, but it can also occur for a single boundary at different temperatures. An example of this is *grain boundary roughening* [27, 28], where above a critical temperature, a wide range of special, CSL boundaries lose detectable structure and behave more like random grain boundaries. In order to improve the expressiveness and power of the CSL concept, further exploration of the effect of microscopic degrees of freedom on grain boundary properties must also be documented.

Another excellent example of both the importance of investigating asymmetric boundaries, as well as the influence of the microscopic degrees of freedom on boundary morphology, can be found in what are called faceted grain boundaries. The structures and behaviors of these special interfaces have captured the attention of researchers for decades [29–31]. Faceting is a boundary transformation in which an interface decomposes from a flat form into a terraced or two-plane structure. Though the faceting process increases the overall surface area of the boundary, and even introduces new defects, the net boundary energy is still reduced. This is because through faceting, a boundary can maximize the area of the lowest-energy planes. The SBP (again, the symmetric boundary plane) for a particular Σ boundary is typically the lowest-energy one and is therefore a

very commonly seen plane in faceting. Details of faceted boundary structure and further relationships to aspects of grain boundary character described above will be explored in the following section.

1.2 Grain boundary faceting

1.2.1 Faceted boundary structure

To introduce the features of faceted boundaries, an example of a faceted Σ5 <001> tilt boundary in BCC Fe, captured using high resolution transmission electron microscopy (HRTEM), is shown in Figure 1.2, characterized by Medlin et al. [32]. The fact that this boundary has become faceted means that it is, by definition, classified as asymmetric, with an average inclination angle β of approximately 25°. However, neither of the two facet planes corresponds to this inclination angle. Instead, it facets along the {310} plane orientation, which is the SBP of Σ5 with the corresponding inclination angle of β = 0°, and the second plane with an index of {210} at approximately β = 45°. Medlin et al. confirmed using density function theory calculations that these planes have the two lowest energy values for all inclination angles of this boundary plane, which as described is typical for faceted boundaries. The sites where the planes adjoin each other are called *facet junctions*, which contain defects that are geometrically necessary to accommodate the change in plane inclination angle. The defect character of these sites is an important part of regulating the length of the repeating facet pair (called the *facet periodicity)* [33–36].

In addition to their unusual structures, faceted boundaries can also undergo transitions. Figure 1.3 shows an example of one of these behaviors, called a *faceting/defaceting transition*. Like the grain boundary roughening phenomenon described in Section 1.1, these transitions have been of interest in studies of phase-like behavior grain boundaries [31, 36–40], also called complexion transitions [41]. The TEM images from a study by Hsieh and Balluffi [29] show an

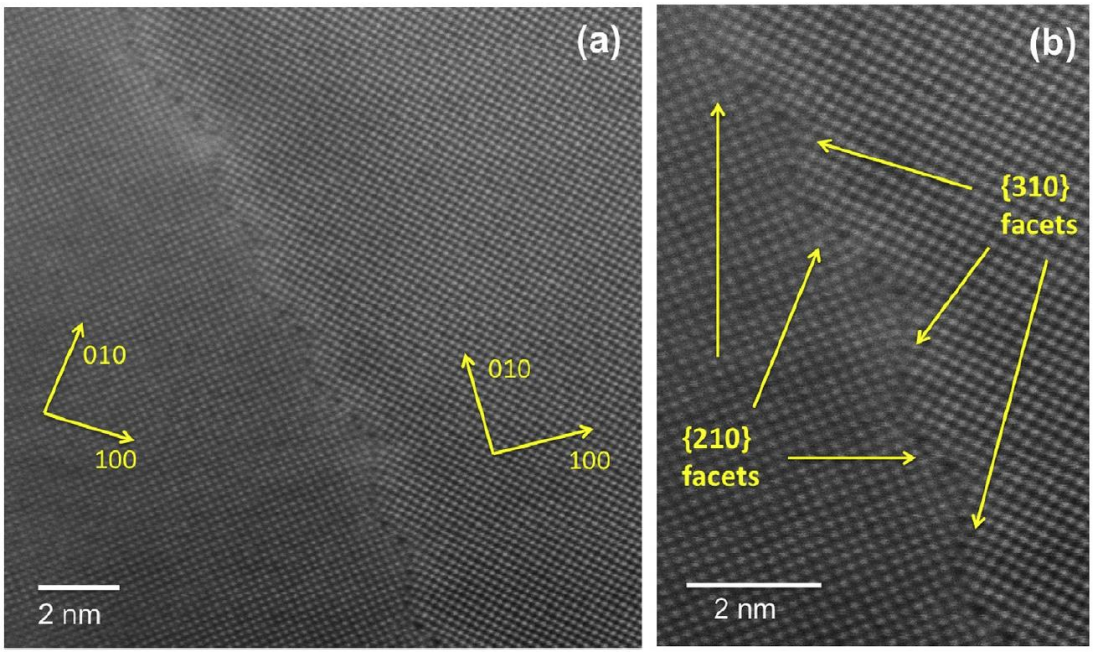

Figure 1.2. Figure from Medlin et al. [37]. HAADF-STEM image showing an asymmetric Σ5 boundary in BCC Fe that has faceted (approximately 25° away from the symmetric {310} inclination). The sites where the facets join are called facet junctions.

example of this process in action in a faceted Σ3 boundary in Al. It is heated in a step-wise fashion (30 min/step) to approximately half of its homologous temperature and cooled again to room temperature. As the boundary is heated, the facets begin to disappear, until by Figure 1.3d the boundary has become mostly flat. The boundary in this state is considered "defaceted" and its boundary plane orientation corresponds to the flat line shown in the schematic of Figure 1.3h. The cooling process brings about the reappearance of the original facets (though in a slightly different configuration than Figure 1.3a). In addition to being fundamentally of interest as an example of a complexion transition in a pure material, there is evidence that faceting/defaceting and similar phase-like changes could have significant impacts on microstructure evolution. Lee et al. [30] observed a faceted boundary in Ni which underwent a defaceting transition similar to that shown in Figure 1.3a-d. The transition of this boundary was found to be directly responsible for an episode of abnormal grain growth. Additionally, experiments on a faceted Σ3 boundary in a Zn

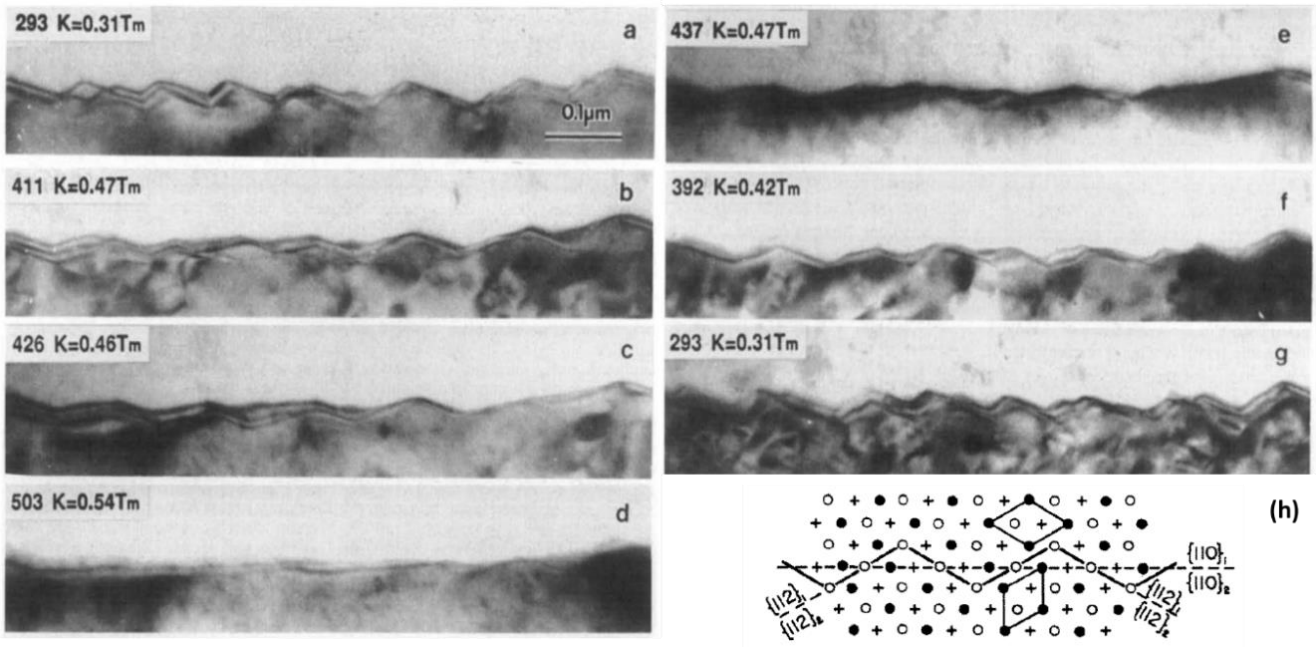

Figure 1.3. (a-g) Images from Hsieh & Balluffi [24] of a faceting/defaceting transition. (h) A schematic of the atomic structure of the faceted Σ3 boundary.

twin plate tip also showed an abrupt increase in facet mobility above T = 623 K. Though itself not a faceting/defaceting transition, it is an example of how facet morphology can influence mobility as well. These results demonstrate the importance of understanding faceted boundaries from a microstructure engineering perspective.

1.2.2 Mobility and faceted boundaries

The grain boundary mobility *M* is a property that describes the speed at which a grain boundary migrates under the influence of a driving force. It is ratio of the observed scalar velocity, *v*, of over the driving force magnitude, *P*:

$$M = \frac{v}{P} \tag{1.1}$$

The driving force can be thought of as a kind of "pressure" acting on boundary atoms, one that may come from a variety of sources, such as interfacial curvature, elastic strains, chemical

gradients, or even magnetic fields [7, 8, 42, 43]. Though as demonstrated in the previous section, faceted boundary structure has been a topic of interest to researchers for a great number of reasons, there exist fewer studies of faceted boundary migration in general. Early theories posited that their mobility might be the average of the individual mobilities of each facet [1], but evidence has not borne this out. Instead, several studies demonstrate that each sub-structure in a faceted boundary plays its own role in boundary migration, and those structures can interact with each other in complex ways [35]. Typically (though by no means exclusively), migration tends to be dominated by the behavior of at least one highly mobile boundary sub-structure, such as the higher-energy facet or facet junctions themselves. The low energy facet (again, typically the SBP of the boundary misorientation) is typically far slower or even immobile [4, 44–47]. The pairing of slow and fast-moving structures can lead to phenomena such as *facet coarsening*, in which the surface area of the low-energy plane is increased dramatically through motion of the more mobile structure over time.

Another remarkable example of the unexplored influence of faceted boundaries in microstructure can be found in the computational literature. Using atomistic simulation techniques, Olmsted and coworkers [11, 51, 52] undertook a wide-ranging survey of multiple grain boundary properties, probing a set of 388 bicrystals in Ni. Especially important amongst their many findings was the discovery that the relationship between temperature and mobility is far more complex than once believed. Typical models of grain boundary motion assume that grain boundary mobility is primarily a thermally-activated property, meaning that boundary migration velocity increases with increasing temperature. However, this mobility survey revealed an incredibly rich variety of behaviors defying original expectation. The range and variety of these relationships is shown in Figure 1.4a, where in addition to classical thermally-activated mobility,

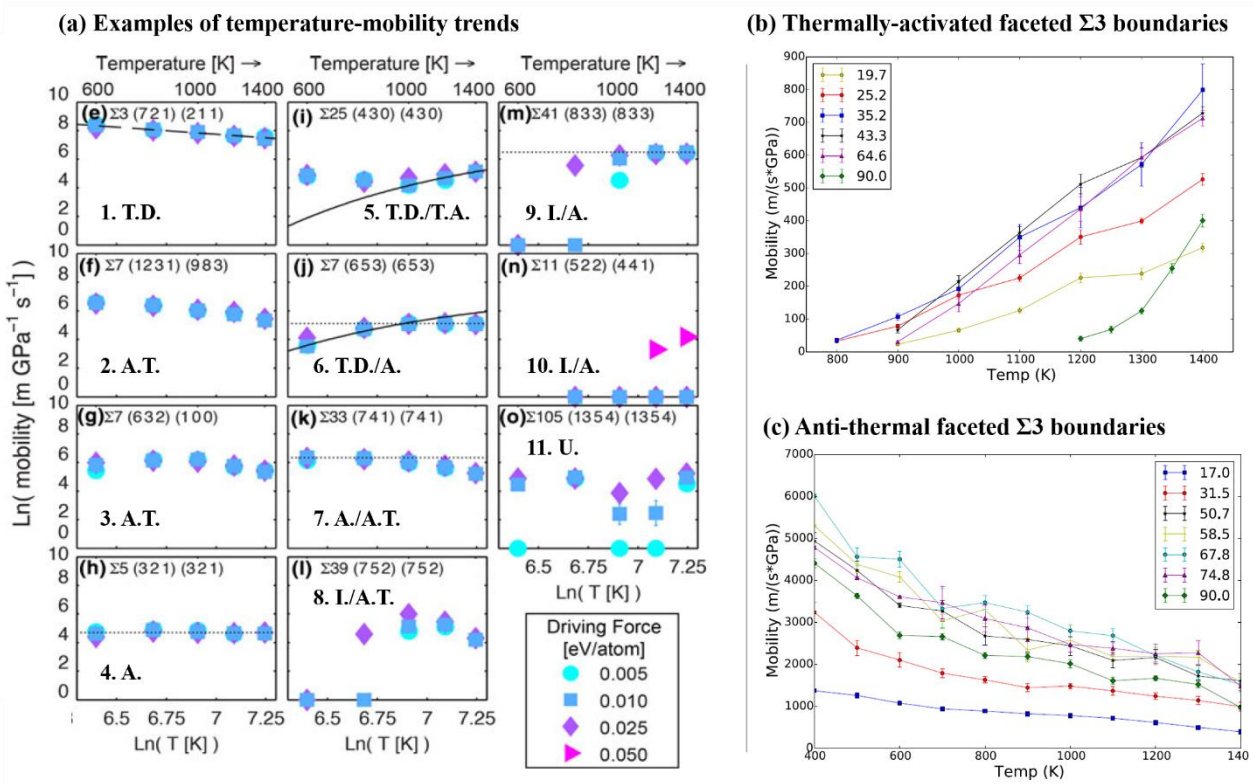

Figure 1.4. (a) Illustration from Homer et al. [1] of a variety of temperature-dependent mobility trends on a log scale. Trends include thermally-activated (T.A.), thermally-damped (T.D.), antithermal (A.T.), athermal (A.), immobile (I.), and unclassifiable (U.). Boundaries that changed trend with temperature are indicated with a forward slash. (b, c) Examples of mobility in faceted Σ3 boundaries in Ni [4]. (a) Conventional thermally-activated grain boundary mobility trends and (b) contrasting unexpected anti-thermal mobility trend.

Homer et al. [1] document trends such as athermal mobility (temperature has no effect on velocity) and antithermal mobiliy, in which boundary velocities decrease with increasing temperature. Antithermally-migrating boundaries are particularly interesting as interfaces that could act to stabilize grain boundary networks at high temperature, but may also be acting to destabilize them at room temperature [44, 48, 49]. Understanding their properties and learning to control them could be of great practical interest. This study also established that even a single boundary can have mixed trends depending on the temperature (indicated in Figure 1.4a with slashes).

Continuing studies on this dataset revealed that a subset of faceted Σ3 boundaries stood out. Research by Humberson and coworkers [4, 44] indicated that, though some of those faceted

boundaries exhibited thermally-activated behavior (Figure 1.4b), a number of others were strongly antithermal (Figure 1.4c). Even more notable, the antithermal faceted boundaries have incredibly high mobility values at near-room temperature. Detailed studies of these boundaries' dynamic structure showed that, due to having differing tilt axes, the thermally-activated and antithermal boundaries' high energy facets moved differently. Though both migrated with the coordinated motion of triplets of Shockley partial dislocations, the ones in the antithermal boundaries are particularly well-ordered and coordinated at lower temperatures. Higher temperatures interrupt their coordinated motion, slowing the mobile facets significantly. Taken together with the defaceting-induced abnormal grain growth noted in the previous section, these studies demonstrate how the unusual behavior and defect structure of faceted boundaries could be responsible for dramatic changes in microstructure across an enormous range of temperatures.

1.2.3 Segregation and faceted boundaries

One of the most important means of altering grain boundary properties, including mobility, is through the tools of alloy design. Interfacial segregation in alloys is a process in which solute atoms leave bulk crystalline regions to populate surfaces or grain boundaries, which increases the concentration of said solute in that region. The amount of segregation is a function of several thermodynamic and kinetic parameters, especially temperature. It's relationship to temperature is frequently quantified in a value called the enthalpy of segregation, or ΔH_{seg}. Most current research indicates a need to develop even more nuanced models, ones based on an atom-by-atom analysis of grain boundary segregation energies. Specifically, Wagih and Schuh [50] have found that treating segregation energy as a spectrum, rather than as an average, greatly improves thermodynamic models of segregation on larger length scales. Investigations into faceted

boundary segregation support their conclusions, as solute absorption has been shown to be highly anisotropic with respect to structure [51, 52]. For example, an atom probe study of a faceted Σ3 boundary in Si by Liebscher et al. [53] showed that impurity and dopant atoms showed a strong tendency to segregate to facet junctions exclusively, creating arrays of long linear defects that are quite different than those that would be predicted from general segregation models.

In addition to faceted boundaries demonstrating marked anisotropic segregation evident in the experimental literature, there are also intriguing examples of segregation altering the process of faceting itself. A study of hydrogen segregation in faceted Σ3 boundaries in Ni by O'Brien and Foiles [52] demonstrated that high H-concentrations frequently resulted in defaceting transitions. Priedeman and Thompson [54] demonstrated that the periodicity of faceted Σ27 boundaries in a pure Pt sample could be altered by the addition of Au dopants. Peter et al. [55] have shown that segregation can even induce faceting in initially flat Σ5 boundaries in Cu. Finally, Yu et al. [56] have shown the same phenomenon to be more universal in nature through experiments demonstrating Bi segregation-induced faceting in Ni for general grain boundaries as well. Such examples of segregation-induced transitions in structure (also from impurities) support the complexion model of grain boundaries, especially faceted ones, as fundamentally phase-like.

Though an understanding of faceted boundaries and their segregation is important from a scientific standpoint, their behavior could also be leveraged to improve microstructural characteristics. The developing field of grain boundary segregation engineering offers new perspectives on microstructural and material property manipulation [57]. The above-mentioned study of faceted Σ3 boundaries in Ni by O'Brien and Foiles [52] have shown that hydrogen preferentially segregates to high-energy facet structures, showing their potential use as getters that may inhibit hydrogen embrittlement. Using atom probe tomography on a dilute Al-Zn-Mg-Cu

alloy, Zhao and colleagues [51] showed that several low-Σ faceted boundaries exhibited anisotropic segregation patterns, resulting in periodic enrichments of Mg and Zn to specific facet planes in each CSL type. They propose that this structure-specific segregation to facets could be as a means to increase boundary cohesion and favorable precipitation behavior. Understanding the phase-like nature of faceted grain boundaries and their segregation could provide nuanced pathways to tuning material microstructure.

Another important and rapidly accelerating area of interfacial segregation research is in the field of multi-principal element alloys (MPEAs), also known as high-entropy alloys or complex concentrated alloys. Through careful selection of elements and composition, a single-phase solution with a random mixture of components can be created. This combination of highly ordered crystalline structure with a highly disordered chemical one frequently introduces a fascinating combination of exceptional properties such as high fracture toughness, crack resistance, and strength at cryogenic temperatures [58–61]. Investigation into the nature of crystalline defects in MPEAs have also shown intriguing changes in dislocation structure [62–65] and vacancy formation [66]. The chemical complexity of MPEAs also means that they have intrinsic tendencies towards local elemental segregation. In bulk crystal regions, this drive to segregate can lead to the formation of domains of short-range order which can introduce solute strengthening effects [67–69]. In larger defects, segregation naturally results in elemental compositions very different from the bulk. Unlike in traditional alloy design paradigms, it very difficult to control the amount of intrinsic segregation occurring in defects in MPEAs. However, this phenomenon can also be leveraged to improve material properties, such as recovery from radition damage [70–72].

Though there have been important advances in the understanding of MPEAs and grain boundary structure and segregation, this research is still in its nascent stage. Existing works point to strong elemental segregation to grain boundaries [73, 74] which has been shown experimentally to be dependent on grain boundary character [75, 76] Atomistic studies have shown there to be highly complex interactions between elements resulting in layered compositions at grain boundaries and surfaces [74, 77]. Given the evidence of highly anisotropic segregation as well as segregation-induced structural transformations in faceted boundaries noted above, a study of the impact of inherent segregation in MPEAs might provide unique insights that could accelerate current research pathways.

1.3 Faceted Σ11 <110> tilt boundaries

Amongst interfaces that facet, the Σ11 <110> tilt boundaries stand out as particularly interesting. Not only do they exhibit faceting/defaceting transitions such as that observed in the Al Σ3 boundary in Section 1.2.1 above (Figure 1.3), but they also have unusual morphologies that have made their study especially fruitful. For one, the Σ11 symmetric boundary on this tilt axis has a very simple structure relative to many boundaries, and also has an extremely low energy relative to other misorientations [15]. It is in fact second only to the (famously) low energy Σ3 boundary for boundaries on the <110> tilt axis. Its secondary faceting plane has an unusual character as well. It is an incommensurate interface, with a plane orientation of {001}/{111},

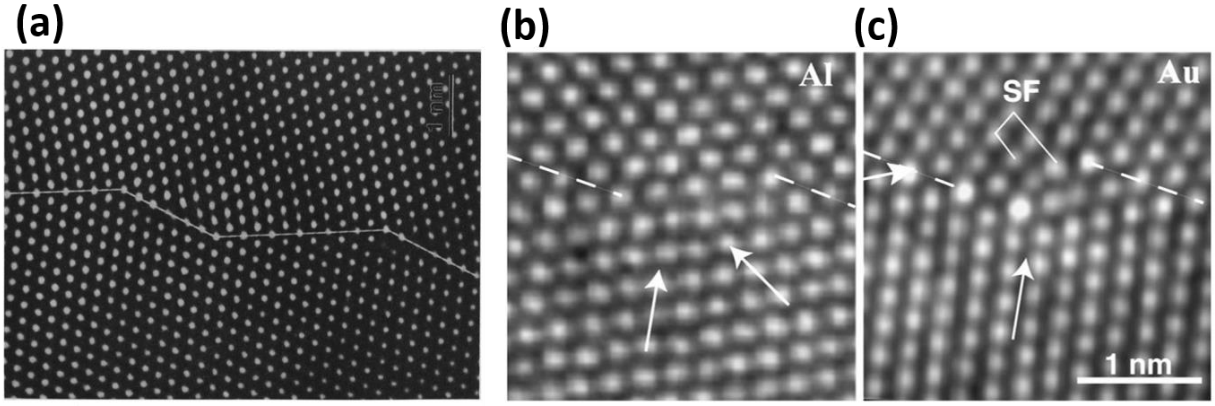

Figure 1.5. HRTEM images from Merkle et al. *[5, 6]*. (a) A faceted Σ11 <110> tilt boundary in Au with long facet lengths (short facet periodicity), highlighting the SBP facets (horizontal) and IBP facets (inclined). (b, c) Facet junction defects found in macroscopically-identical faceted Σ11 boundaries in (left side) and Au (right side) with identical macroscopic parameters.

which as mentioned briefly in Section 1.1 exhibits quasiperiodicity [22]. High-resolution TEM images of this boundary, created by Merkle et al. [5, 6] are shown in Figure 1.5. The two facet planes of the Σ11 boundary in Au are featured in Figure 1.5a, with the SBP facets oriented horizontally, and the IBP facets descending from left to right.

In addition to having unusual facet planes, the defect structures at and near junctions, called *junction defects*, of asymmetric Σ11 boundaries are similarly unusual. The same junction defect in different materials can take on very different forms. An example is shown in Figure 1.5b and 1.5c, which show the facet junctions of two macroscopically identical faceted Σ11 boundaries in Al (4b) and Au (4c). The white lines indicate the site of the SBP facets. Just as perfect dislocations in the bulk of a low stacking fault energy material such as Au or Cu crystal can lower their energy by dissociating into two Shockley partials, grain boundaries can also lower their energy by releasing a Shockley partial dislocation into a neighboring grain. This phenomenon is called *grain boundary stacking fault emission*, a well-documented phenomenon that can strongly influence the structure and mechanical properties of interfaces [78–83]. Because of the low stacking fault energy of Au, the facet junction has relaxed by creating a small stacking fault (denoted with "SF").

In contrast, the Al boundary on the left cannot emit stacking faults due to having a very high stacking fault energy. The contrasting structures shown here highlight once more the importance of understanding interaction between macro- and microscopic degrees of freedom. Though some structures remain relatively unaffected by changes in material (the SBP facets), others can change drastically (the IBP facets and the junctions) in ways that could potentially impact grain boundary kinetics.

Though the static structures of faceted Σ11 boundaries in pure metals have made a regular appearance in structural grain boundary research for many decades [7, 10, 15, 29, 34, 78, 84–88], there is far less information available about their dynamic behavior and chemistry in alloy systems. The existing evidence to date on these boundaries suggests interesting structure-property relationships in several different contexts. Already mentioned above is the documented faceting/defaceting transition observed by Hsieh and Balluffi [29] in Al. Another example of interesting behavior in an Al alloy can be found in the atom-probe tomography data of a faceted Σ11 boundary, in which it was shown that this interface exhibits anisotropic segregation of Mg and Zn. Specifically, one facet plane in particular was found to have roughly double the site of favored segregation in an Al alloy [51]. Further investigation using atomistic simulations revealed that Mg is highly favored to populate the facet junctions and regions near it. There is also evidence that faceted Σ11 boundaries can be created by mechanically-driven grain boundary migration in nanocrystalline materials. In a atomistic simulation of cyclic deformation in nanocrystalline Al, Panzarino and Rupert [89] measured an increase in Σ11 boundary fraction, including observations of faceted Σ11 boundaries. A further investigation of these interfaces, paired with the rich body of knowledge on their structure that already exists, could yield further important insights into the role of this and similar faceted boundaries in general.

1.4 Molecular dynamics and the study of grain boundary properties

As described above, research has consistently revealed the importance of the local motion and interactions of atoms, or in other words, the microscopic degrees of freedom, in determining grain boundary properties. For that reason, *molecular dynamics* (MD) simulation methods are a natural choice to probe grain boundary structure-property relationships in general and is well-suited to faceted boundaries specifically. MD is an atomistic simulation method that models the classic Newtonian equations of motion in order to understand the evolution of groups of atoms through time. An important part of any MD simulation is the choice of *interatomic potential*, which approximate the potential energy field created by a system of atoms. All simulations used in this dissertation use interatomic potentials created using the *embedded atom model* (EAM). Though EAM potentials cannot perfectly emulate all physical properties of metallic materials, they may be created or selected to accurately reproduce properties of interest, such as melting temperature or stacking fault energy.

MD simulations have the advantage of being able to both emulate traditional experimental methods such as curvature-driven grain boundary migration [90, 91] as well as apply techniques that are completely unique. In fact, in the study of grain boundary character, the 'artificial' nature of MD simulations gives scientists a perspective on atomistic properties that would otherwise be impossible. Grain boundaries studied in physical crystals, or in larger-scale polycrystalline computational models, are naturally connected to neighboring boundaries, triple junctions, or free surfaces. These issues confound the search for structures and behaviors which are inherent to boundary itself versus those influenced by local features. A unique solution to this issue is the ability to use partially or fully periodic boundary conditions in simulation cells. Periodic boundary conditions are a mathematical construct used to emulate an "infinite" lattice. For interfaces, this

means that it is only connected to itself across the periodic boundary dimension parallel to the interface norm. In that sense, it is a very 'pure' representation of the grain boundary's character, given that the bicrystal cell is large enough to avoid self-interactions over periodic boundaries. These techniques allow a far clearer observation of the atomistic mechanisms behind a great number of grain boundary properties.

For the above reasons, MD bicrystal simulation is frequently the tool of choice for scientists interested in grain boundary properties [1, 16, 34, 44, 92, 93]. In the following subsections, we provide a brief outline of the MD methodologies used in this dissertation to model grain boundary mobility and segregation.

1.4.1 Modeling grain boundary mobility

Another advantage offered by MD in studies of grain boundary mobility is the ability to apply what is called an artificial driving force (ADF), also called a synthetic driving force. To induce grain boundary motion, the ADF algorithm assigns an orientation-dependent potential energy to every atom of the bicrystal. One of the grains is chosen to grow, which is referred to as the favored grain, represented with blue atoms in the two bicrystals of Figure 1.6. This means that its atoms each receive a negative potential energy. The atoms in the other, shrinking grain (the unfavored grain, represented by red atoms in Figure 1.6) receive a positive potential energy of the same magnitude. The grain boundary atoms, which have orientations somewhere between the two grains, receive a value higher than that in the favored grain, inducing them to reorient themselves towards the lower-energy grain. ADFs induce boundary motion by introducing an energy gradient across the bicrystal, through the assignment of potential energies to each atom based on their local orientation. This is analogous to experimental techniques employing a magnetic driving force [8,

43], as one grain is favored to grow at the expense of the other. Over time, this leads to boundary migration (white arrows in Figure 1.6). The physical principle behind the ADF is that, on the atomic scale, any change in atomic position that can reduce the free energy of the system is favored, regardless of whether it comes from a mechanical, geometric (in the form of curvature), chemical, or magnetic source. The interfacial motion induced by an ADF are thought to accurately reflect the fundamentally atomistic nature of grain boundary migration [1, 94, 95].

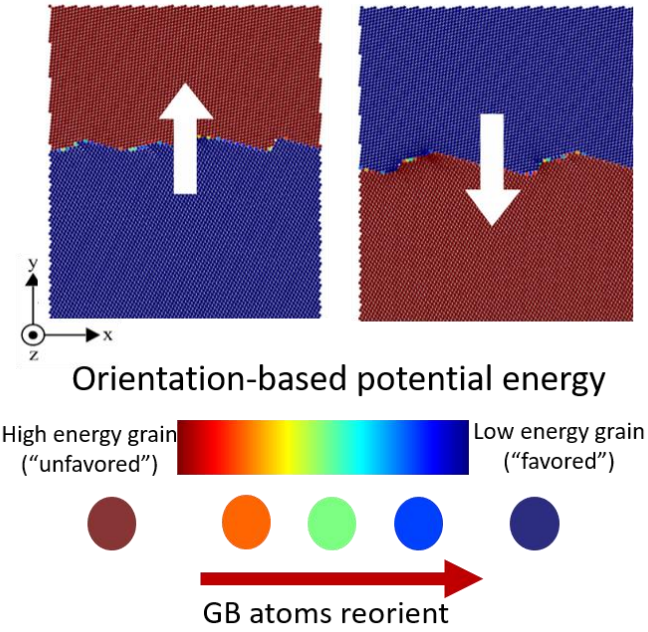

Figure 1.6. Schematic of the artificial driving force in a computational cell.

1.4.2 Modeling grain boundary segregation

As described in Section 1.2.3 above, grain boundary segregation is best modeled as a spectrum of energies [50] , which themselves are taken from the segregation energy of individual atoms making up the interface. Atomistic modeling is thus also an excellent tool for simulating and analyzing segregation patterns in interfaces. However, MD alone cannot be used to simulate segregation. The timescales allowed by MD are far too short to take into account the diffusive motion of atoms. Instead, the issues of timescale and diffusion are sidestepped by applying a

Monte Carlo (MC) algorithm to iteratively swap solute atoms with solvent atoms. MC algorithms are a set of numerical methods that use random sampling to build approximations of a system's behavior. In this case, the atom swaps performed by MC are used to test for changes in energy. In the case of a favorable solute-solvent swap, the solute atom remains at its new site, and is other wise rejected. MD steps are then performed to advance the system through time. The combination of these two methods, called a hybrid MC/MD simulation, allows the alloy system to find both its chemical (MC) and structural (MD) equilibrium.

1.5 Problem statement and research objectives

As described above, there are a number of important open questions in grain boundary research. We believe that a focused study of faceted boundaries, and specifically the faceted Σ11 <110> tilt boundaries, could address several of these questions in an elegant way. Firstly, research into low-Σ grain boundaries has been a fruitful area of study, especially with respect to static structure. However, a general focus on symmetric boundaries over asymmetric ones has created gaps in understanding the dynamic behavior of more topologically complex boundaries. As an asymmetric boundary that pairs a highly symmetric, "classic" low- Σ plane with an even more unusual incommensurate one, the faceted Σ11 boundaries. This boundary set also has been shown to undergo faceting/defaceting transitions in Al, which demonstrates its capacity to act as a technically important factor in microstructure evolution. In terms of mobility, the asymmetric geometry of faceted Σ11 interfaces suggests that they may exhibit unusual migration trends, similar to those of the anti-thermal boundaries featured in the work of Humberson and coworkers [4, 44]. Especially the potential influence of grain boundary stacking fault emission, shown in Figure 1.5c in the Au boundary, is of particular interest with respect to mobility. Defects like emitted stacking

faults in and near facet junctions could also prove to be an important influence in regulating segregation in these boundaries. As described in Section 1.3, junction-specific segregation was already demonstrated in faceted Σ11 boundary in Al.

Through the lens of a set of faceted Σ11 <110> tilt boundaries, we aim to fulfill the following research objectives:

- Chapter 2: Basic tests of mobility are performed on Cu and Al boundaries using the ADF technique (Section 1.4.1). An unexpected migration trend is discovered. Connections between atomistic migration mechanisms and the dynamic atomic structures of the SBP facet, IBP facet, and emitted stacking faults in Cu are explored in detail and characterized.
- Chapter 3: The unique mobility trend and atomistic migration mechanisms that were discovered and categorized in Chapter 2 are tested for their generality. To accomplish this, the range of simulated materials is expanded from two EAM potentials to six, representing three different FCC materials (Al, Cu, and Ni). A model of competition between migration mechanisms is proposed to explain observed behavior.
- Chapter 4: A case study of an individual faceted Σ11 boundary in Cu-Ag is used to investigate the effect of alloying on the migration mechanisms outlined in previous chapters. Facet-specific trends in Ag segregation are also documented.
- Chapter 5: Further explorations of the effects of alloying on faceted Σ11 boundary structures and properties are conducted in the context of two MPEA materials, CuNiCoFeCr and NiCoFeCr.

2 Emergence of directionally-anisotropic mobility in a faceted Σ11 <110> tilt grain boundary in Cu

2.1 Introduction

As established in Chapter 1, a rich body of literature exists on the structure of faceted Σ11 boundaries, but almost none on their migration mechanisms. Their unusual structures, especially the stacking fault emission observed in the TEM Au sample in Figure 1.3c, strongly suggests that these boundaries may have similarly unusual migration mechanisms. In this chapter, we report on the grain boundary migration behavior of one faceted Σ11 boundary (β = 35.3°) using the ADF method described in Chapter 1.4.1. Through three different temperatures, this boundary is probed in two different face centered cubic materials, Cu and Al. These materials were chosen as contrasting examples of the effects of stacking fault energy on boundary mobility. Like Au in Figure 1.3c, the low stacking fault energy of Cu results in very similar defects as those described in Chapter 1.2.1, which do not appear in Al. We explore the origins of an unexpected difference in migration velocity observed in the Cu boundary and propose a characterization scheme for the atomistic motion mechanisms in both the Al and Cu boundaries.

2.2 Methods

Here, the bicrystal methodology for the creation of all grain boundaries studied in this work is outlined and described in detail. For future chapters, readers will be referred to this section. As described in the Introduction (Chapter 1.1), the geometry of a bicrystal can be defined by five angles, which represent the macroscopic degrees of freedom. The misorientation represents the first three needed to bring the two crystals into coincidence and determines the CSL value of the bicrystal (e.g., Σ11). The last two determine the direction of the boundary plane's normal vector.

In tilt boundaries, the azimuthal angle α is parallel to the tilt axis and is thus by definition 90°. The inclination angle β has a range of $0° \leq \beta < 90°$ (a result of four-fold symmetry in cubic structures). By varying β, one may produce a wide array of tilt bicrystal structures. The one with the lowest-energy and highest symmetry is the symmetric boundary plane (SBP) that is found at $\beta = 0°$. The SBP for the $\Sigma 11$ <110> tilt bicrystal is shown in Figure 1a, which has an orientation of $(113)_A/(11\text{-}3)_B$. Visualization of boundaries and parts of the data analysis were performed using the OVITO software toolset [96]. Boundary snapshots are quenched using a conjugate gradient technique that removes thermal noise to allow for detailed structural analysis and then colored according to common neighbor analysis [97], with green indicating local face centered cubic (FCC) orientation, red indicating hexagonal close packed (HCP) orientation, and grey indicating any other or an undetermined orientation. All atomic volume calculations were performed in LAMMPS using the library Voro++ [98].

Faceting is predicted for this type of boundary when β is less than approximately 60° [78]. Boundaries featured in future chapters include this β and a wider variety of angles, spanning a range from $\beta = 46.7°$ in Chapter 3 to a low value of $\beta = 10.2°$ in Chapter 5. For this initial study of mobility, we chose $\beta = 35.3°$, corresponding to the purple dotted line in Figure 2.1a. An asymmetric $\Sigma 5$ <001> tilt boundary ($\beta = 32.5°$) was also generated and probed to provide a boundary from a different CSL orientation that is asymmetric without faceting for comparison. Additionally, two EAM potentials were utilized, with one representing Al [99] and the other modeling Cu [100]. Various properties of the potentials, as well as grain boundary energies calculated from the Tschopp algorithm described above, are included in Table 2.1. The melting temperatures for each potential were confirmed to be within ±5K of the reported values using the method outlined by Wang et al. [101]. Note that the viewing angle of all boundary images in this

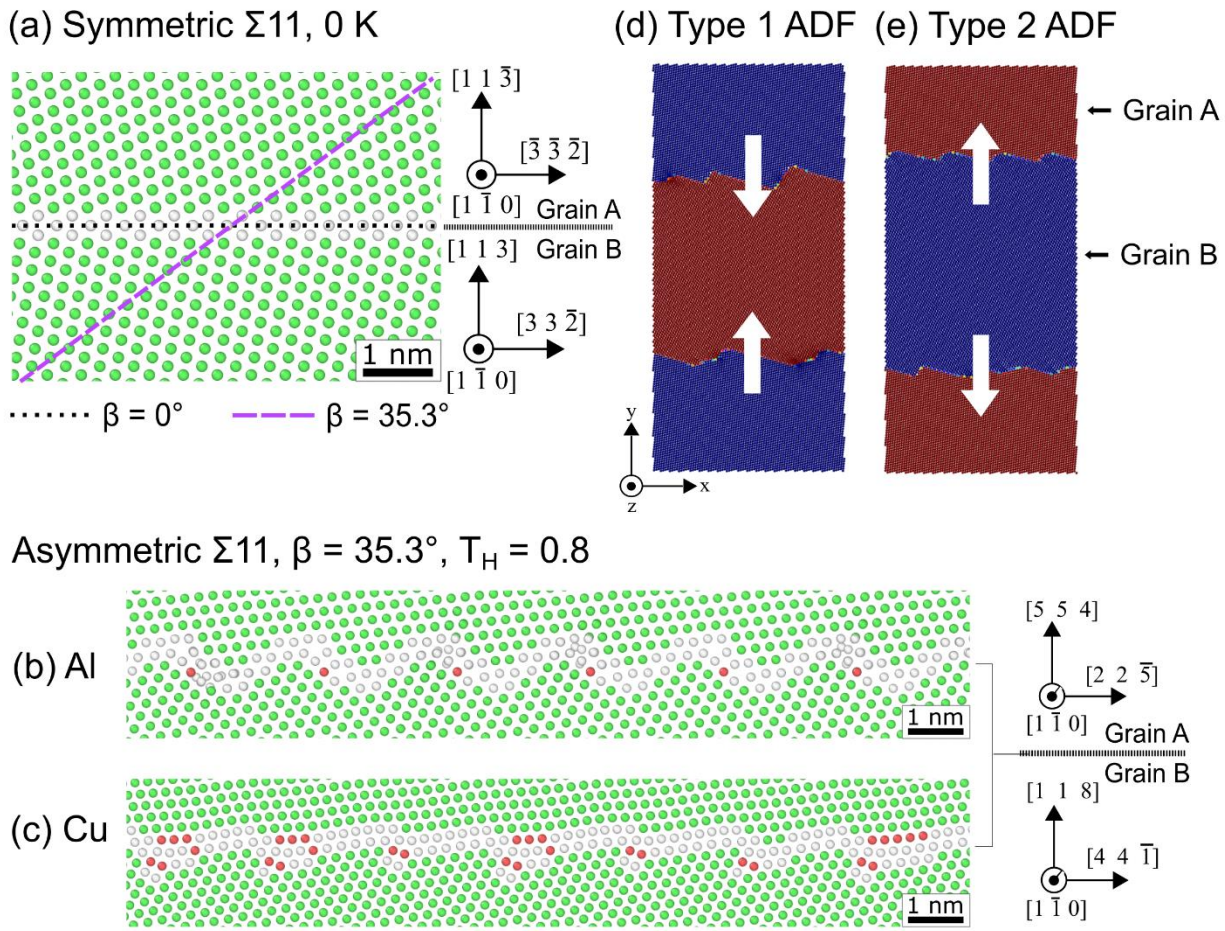

Figure 2.29. (a) The Σ11 symmetric $\beta = 0°$ boundary, indicated by a black dotted line, which has the lowest energy of any Σ11 boundary. The boundary plane with $\beta = 35.3°$ under study here is indicated by the purple dashed line. (b, c) The as-annealed boundaries at $T_H = 0.8$ for $\beta = 35.3°$ in (b) Al and (c) Cu, which have identical crystallography (shown on the right side of both boundaries), where different potentials have different facet morphologies. (d, e) The Type A and Type B ADF, where the favored (blue) and unfavored (red) grains are swapped to change the direction of boundary migration.

dissertation is down the <110> axis, unless otherwise indicated. All bicrystals used in the current work were generated in the Large-scale Atomic/Molecular Massively Parallel Simulator (LAMMPS) [102], using code developed by Tschopp et al. [85] for the identification of minimum energy grain boundary structures. This algorithm probes all possible fully periodic structures for a given crystal orientation by iteratively shifting the boundary plane and deleting different

EAM	a_0 [Å]	T_{melt} [K]	γ_{SF} [mJ m^{-2}]	E Σ11, 0° [mJ m^{-2}]	E Σ11, 35.3° [mJ m^{-2}]	E IBP * [mJ m^{-2}]	E Σ5, 32.5° [mJ m^{-2}]
Al [99]	4.05	1035	146 [99]	150.8	352.2	270.9	526.8
Cu [100]	3.615	1357	44 [100]	309.9	608.7	436.8	986.3
* IBP energy estimated from 80% of the 29.5° boundary energy [78]							

Table 2.2. Selected properties of the potentials, Σ11 boundaries, IBP, and Σ5 boundaries, including grain boundary energies (*E*) and stacking fault energy (γ_{SF}).

combinations of atoms. From the set of generated cells, which are fully periodic, the lowest energy option is selected.

At different points in this dissertation, we refer to EAM potentials as different "materials." When using this term, it is crucial to acknowledge that interatomic potentials are attempting to simulate atomic interactions and are not always capable of replicating all the properties of the named element or alloy. Especially with dynamic behavior such as grain boundary mobility, there can be great variability between potentials representing the same element or material [4]. However, the phenomenon of directionally-anisotropic mobility explored in the first three chapters of this work is shown to be strongly related to stacking fault energy, which correlates with grain boundary dislocation content and faceted Σ11 structure. Therefore, an effort was made to choose interatomic potentials that matched experimental values for stacking fault energy overall, or where not possible, were within reasonable values. For the Cu potential, the calculated stacking fault energy of 44 mJ m^{-2} shown in Table 2.1 agrees very well with the reported experimental value of 45 mJ m^{-2} [100]. The Al potential's stacking fault energy of 146 mJ m^{-2} [99] is an intermediate value within the experimentally-measured range of 120-166 mJ m^{-2}. Therefore, both potentials describe the stacking fault energies well and also represent the differences between the two materials that are important with respect to structure (and thus also directionally-anisotropic mobility). For these reasons, we use the term "material" to describe simulations that use the different interatomic potentials that are approximating atomic interactions in Al and Cu.

System size is an important consideration for grain boundary mobility studies [4, 44, 48, 103–105]. Bicrystals that are too small, specifically those that are too short in the direction of the grain boundary normal, have resulted in problematic mobility artifacts [103–105]. Other recent work has shown that these size considerations may only strictly apply to systems with flat boundaries, and less so to asymmetric or defect-heavy boundaries such as the asymmetric Σ11 and Σ5 boundaries studied here [106]. However, in this Chapter as well as Chapters 3 and 4, we conservatively choose to ensure that the boundary is large enough to avoid common mobility artefacts introduced by periodic boundary conditions, but also small enough to optimize computational efficiency. For both the Σ11 and Σ5 boundaries, the total height perpendicular to the grain boundary normal, L_y, was made equal or greater than 30 nm to alleviate any concerns. The generated Σ11 bicrystals had heights of 33.4 nm for Al and 35.8 nm for Cu, within the acceptable zone outlined by Deng and Deng [104]. The minimum tilt-axis thickness, L_z, was fixed to be ten repeats of the lattice parameter, a_0, giving thickness values of 4.1 nm and 3.6 nm for Al and Cu, respectively. The minimum length for L_x, the direction parallel to the grain boundary plane, was set to 9 periodic repeats of the generated facet structure, producing a length of 21.2 nm in Al and 19.1 nm in Cu. The total number of atoms in each simulation cell was 166,068 for Al and 198,576 for Cu. Both the Σ5 in Al and in Cu had 143,400 atoms, with Al measuring 17.4 nm by 34.8 nm by 41.0 nm (L_x, L_y, L_z), and Cu measuring 15.6 nm by 31.2 nm by 36.9 nm (L_x, L_y, L_z).

Once generated, boundaries were relaxed using an NPT ensemble with a Nosé-Hoover thermostat and barostat to regulate temperature and ensure zero pressure on the cell. Annealing runs were initialized by adding a randomized velocity to atoms in the minimized bicrystals corresponding to half the target temperature. Heating was then applied for 120 ps, with a ramp to

bring the temperature to its target value within approximately the first 10 ps. Three simulation temperatures were chosen, corresponding to homologous temperatures of approximately 0.8, 0.85, and 0.9. Examples of as-annealed Σ11 boundaries for each potential at T_H = 0.8 are shown in Figure 1b and c, demonstrating that faceting occurs for both Al and Cu but the local structure is different. These structures will be discussed more thoroughly in the Results and Discussion section. At least 6 equivalent configurations were created for each combination of temperature, potential, migration direction, and CSL, using unique, randomly-generated velocity seeds for the initial temperature.

After equilibration at the target temperature, the energy-conserving orientational ADF developed by Ulomek et al. [95] was applied for a minimum of 120 ps and up to 1 ns for very slow/immobile boundaries. A cutoff value of 1.1 a_0 was chosen to capture first and second nearest neighbors. The ADF functions by adding an orientation-dependent energy to one grain of the bicrystal (i.e., the 'unfavored' grain). This added energy creates an energy gradient across the interface with the second, 'favored' grain. At each timestep, atoms in the favored grain are given potential energy values of $-\Delta E/2$, and atoms in the bulk of the other, unfavored grain are given values of $\Delta E/2$, resulting in a potential energy difference with an average magnitude of ΔE (in units of eV/atom). Grain boundary atoms, which are assigned energy values between those of the two neighboring grains, are driven to shift towards the lower-energy orientation. Over time, these shifts allow the favored grain to grow at the expense of the other. In this study, the choice of the favored and unfavored grain is swapped to observe differences in boundary migration direction. Thus, a clear designation of which grain is the favored or growing grain is important. For the remainder of this work, we refer to the growth of Grain A as *Type A* behavior and growth of Grain

B as *Type B* where Figures 2.1d and 1e show the two different options. The blue-colored region is the favored grain in these figures, and it is growing in the direction of the white arrows.

To ensure clarity, the visualization of boundaries will only show the topmost boundary of each bicrystal, meaning that Grain A will always appear above Grain B, although we note that all actual measurements were made using both boundaries. Type A migration will thus always imply that the boundary shown in any figure is moving in the negative Y-direction. The opposite is true for Type B migration, which will always refer to the bottom grain in snapshots growing, meaning that the boundary moves in the positive Y-direction.

Similar to problems with system size in molecular dynamics, periodic boundaries using ADFs can be sensitive to ΔE [35, 44, 103, 105]. Driving force values in the range of ΔE = 10-25 meV/atom were initially tested. Because some boundaries at the lowest homologous temperature of 0.8 are relatively immobile, the higher value of 25 meV/atom was used. This choice is reasonable because the boundaries studied here are non-planar and have a high defect content. Several prior studies indicate that both of these features can strongly impact a boundary's sensitivity to high driving forces [103, 105, 106]. In addition, Race et al. [106] found that a driving force of 25 meV/atom, the same as was used here, did not alter the fundamental migration mechanisms of heavily defected boundaries, including a faceted boundary. In addition, molecular dynamics studies of Σ3 <110> tilt boundaries have shown that especially slow moving boundaries require higher driving forces for appreciable motion [4, 107]. Grain boundary velocities, *v*, were measured by tracking the mean position of each of the two boundaries separately for at least 50 ps of steady-state motion. As stated in Chapter 1.2.2, the grain boundary mobility, *M*, was then calculated as:

$$M = \frac{v}{P}, \qquad 2.1$$

where P is the pressure experienced by the boundary (in this case, through the artificial driving force). The units of M are m GPa^{-1} s^{-1}. P is related to the ADF's energy gradient value, ΔE, through the average atomic volume, Ω (found using the lattice constants listed for each potential in Table 2.1), and the conversion of eV to GPa, such that:

$$P = \frac{\Delta E}{\Omega} \cdot \frac{1.602 \cdot 10^{-28}\ GPa}{eV}. \quad 2.2$$

2.3 Results and Discussion

2.3.1 Detailed boundary structure in Al and Cu

We begin with a detailed description of the equilibrium structures of the boundaries in Al and Cu in Figures 2.2 and 2.3, respectively. In addition to atomic snapshots of each boundary, these figures contain schematics highlighting local structural units, relevant crystallographic planes, and other important features. To better show these planes, atom coloring includes lighter and darker shading which indicates the approximate plane height with respect to the tilt axis. Darker atoms are one {110} plane height lower than lighter ones. In order to simplify the characterization of boundary structure, we will utilize a common tool for identifying grain boundary structures, the structural unit model (SUM) [7].

Two facets of the as-annealed and quenched Σ11 boundary in Al are shown in Figure 2.2a, with brackets indicating the location of each. They have a clear faceted shape, with significant variations in the location of the boundary in the Y-direction and multiple distinct planes. Going from left to right in the X-direction, the ascending sides are facets oriented along the SBP, which are comprised of diamond-shaped C units shown in Figure 2.2b. The C unit is the characteristic unit for Σ11 <110> tilt boundaries in the SUM [15]. The descending side is comprised of a pair of E units (also sometimes referred to as kite-shape structures), which are characterized by a

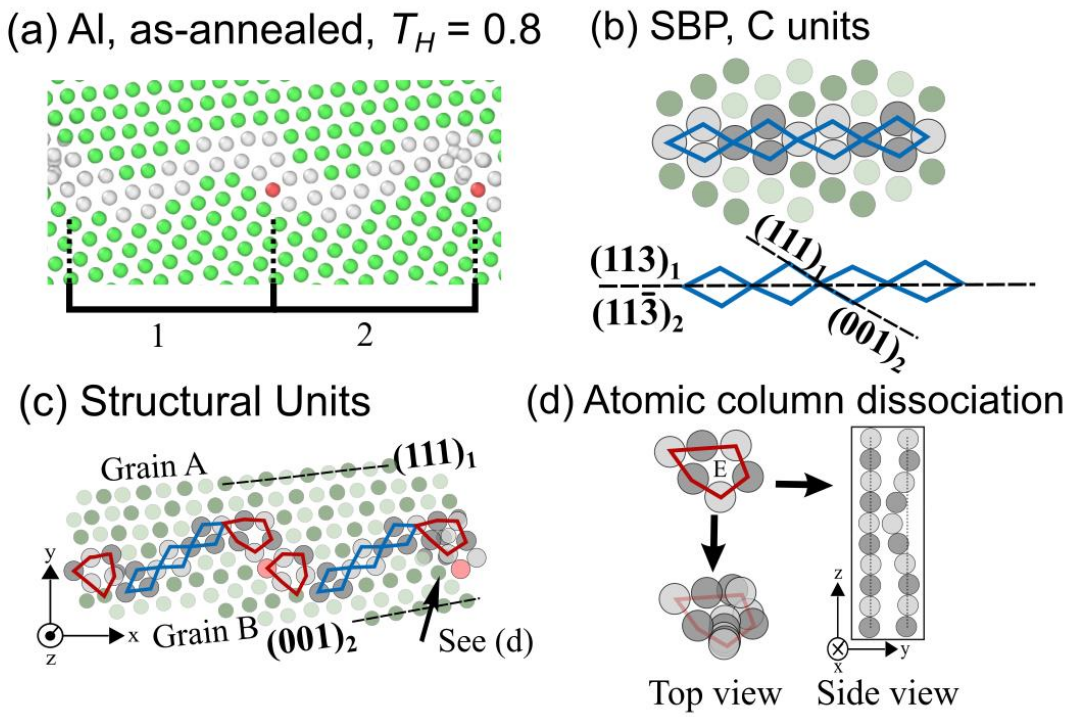

Figure 2.30. (a) Two facets are shown in more detail from the Σ11 boundary in Al. (b) C units that characterize the Σ11 symmetric boundary. (c) Analysis of the facets, with structural units outlined and important planes indicated. (d) Atomic column dissociation, where one or more columns in an E unit buckles into the free volume at the E unit's center.

column of free volume in their center [10]. Figure 2.2c shows the E unit pairs outlined in red as well as their location with respect to the C units on the SBP facets. Though E units are at times categorized into two variants [108], one standard (E) and one elongated (E'), the high temperatures and dynamic boundary behavior in this study make distinguishing the two from each other challenging and we will refer to both types simply as E units. We also note that OVITO common neighbor analysis does not always show all six atomic columns as 'other,' such as in the case of the lower E units in Figure 2.2c. During annealing, the atomic columns that comprise E units dissociate at times, buckling so that there is less free volume at the E unit's center. A schematic example of this process is shown Figure 2.2d. This process, which we call atomic column dissociation, is a fundamental component of boundary migration in Al.

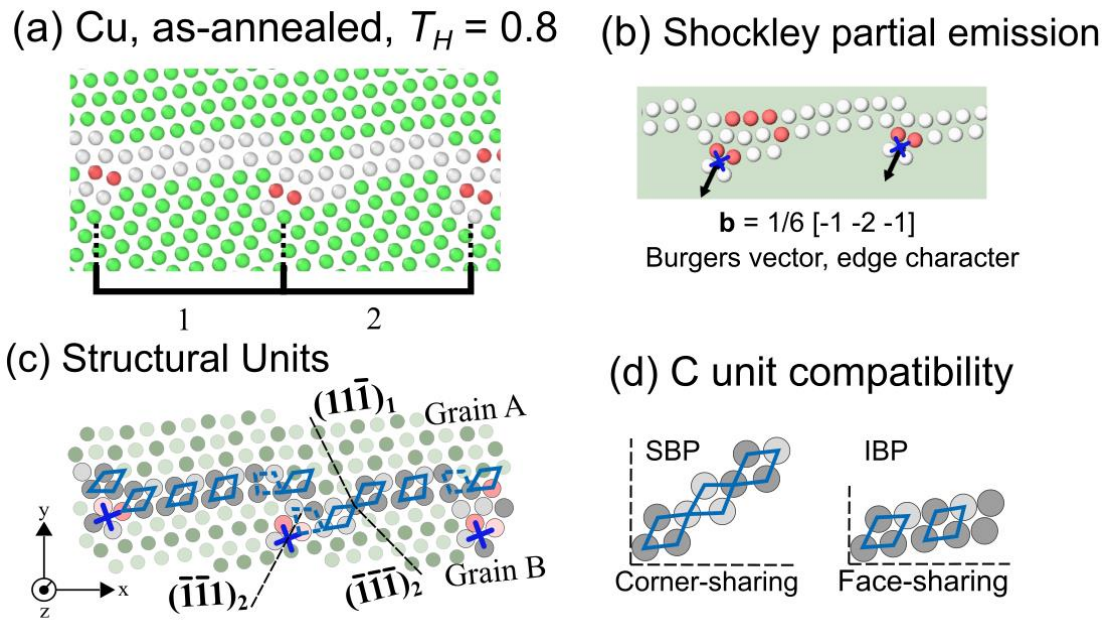

Figure 2.31. (a) Two facets are shown in more detail for the Σ11 boundary in Cu. (b) Shockley partial dislocations are emitted from facet nodes, with their location indicated by a blue X. (c) Analysis of the facets from (a), with structural units outlined and important planes indicated. (d) C unit compatibility between the symmetric boundary plane facet and the incommensurate boundary plane facet.

Figure 2.3a shows two facets of the as-annealed Σ11 boundary in Cu. As described in the Introduction (Chapter 1.3), these boundaries facet along a different plane orientation, namely an *incommensurate boundary plane* (IBP) with an orientation of $(111)_A/(001)_B$. Recall that the term incommensurate indicates that the ratio of the plane spacings between two component planes is irrational, in this case, $\sqrt{(3 / 1)}$. Since boundaries in CSL systems must have rational plane spacing ratios (such as the SBP, which has a plane spacing ratio of $\sqrt{(11 / 11)} = 1$), this means that an IBP interface by itself could not form a Σ11 grain boundary. In fact, the misorientation needed for an IBP is different than the Σ11 misorientation, requiring the other facet segment to have the correct misorientation. In this case, the SBP facet correctly reflects the misorientation associated with a Σ11 interface. The fact that the IBP appears as a preferred facet plane in this asymmetric Σ11 boundary in Cu is a result of it being locally energetically favorable, even though it would not

globally satisfy the misorientation between the grains. Details of the IBP facet structure will be discussed shortly in this section, while information on their energetics, formation, and faceting patterns can be found in other studies, such as those by Brown and Mishin [78] or Wu et al. [34].

At the bracket markings in Figure 2.3a, it can be seen that IBP facets are separated by one or two $(111)_A$ steps on top and a small defect that impinges into Grain B by a few Å. The impinging pattern and the presence of HCP-coordinated atoms (colored red) are evidence of Shockley partial emission from the boundary, which create an array of non-planar defects. It is a relaxation mechanism common to many <110> tilt boundaries in low stacking fault energy materials, including many asymmetric Σ11 boundaries [10, 15, 78]. The presence of Shockley partials was confirmed using the dislocation analysis (DXA) algorithm in OVITO [109], shown in Figure 2.3b.

Structurally, the IBP has been previously interpreted as a quasi-periodically repeating series of E units [78], and the sites of Shockley origin as a special variant of them, the E'' unit [110]. There is another possible interpretation of its structural units that highlights a special crystallographic relationship between the IBP and the SBP facets which is relevant to migration. The IBP's defining $(111)_A/(001)_B$ planes are the also constituent planes of individual C units from the SBP. Where C units in the SBP facets of Al from Figure 2.2b and c are corner-sharing, C units in the IBP could be described as face-sharing. This means that IBP facets and SBP facets are crystallographically compatible with each other.

The detailed schematic of structural units shown in Figure 2.3c shows how these units line up in an IBP facet, and the crystallographic compatibility between corner-sharing and face-sharing C units is highlighted in Figure 2.3d. This structural relationship can be observed in the different facet variants that populate the as-annealed boundary in Cu. Starting from the facet node at the emitted Shockley, Facet 1 in Figures 2.3a and c contains 5 face-sharing C units. One of these units

has an angular distortion indicated by using dashed instead of solid lines. In its neighbor Facet 2, the Shockley partial has migrated down one $(001)_B$ plane, creating a pair of corner-sharing C units. Facet 1 represents the simplest variant of IBP facet with only face-sharing C units, while Facet 2 has a combination of face- and corner-sharing C units.

The geometric compatibility between SBP and IBP facet C units has important implications for mobility. The fact that the C unit is shared between both facet types means that the transitions left-to-right from an SBP facet into an IBP facet are relatively smooth, but the transition right-to-left from an IBP facet to an SBP facet is considerably more structurally complex, encompassing the emitted stacking fault. The C unit compatibility, along with the fact that stacking fault emission only occurs into one grain (which is not always the case [80]), gives the Cu boundary a distinct geometric directionality as compared to Al. The effects of this directionality will be explored further when examining specific migration mechanisms in Section 2.3.3.

To conclude our introduction of Σ11 boundary structure, we address the topic of facet junctions and facet junction defects. The structural complexity of the Σ11 boundaries, the use of two different materials, and the study of dynamic boundary structure (next section) makes the definition of a facet junction somewhat complicated. E unit pairs could be interpreted in several ways, for example as defect-heavy facets by themselves (since they have a relatively clear plane orientation) or as two junction defects, one upper and one lower, that link SBP facets. In the case of the Σ11 boundary in Cu, variations in facet types via C unit unfolding also make the strict identification of the facet junctions complicated. Therefore, instead of defining facet junctions and facet junction defects explicitly, we will instead refer to *facet nodes*. The dashed lines above the brackets in Figures 2.2a and 2.3a show the sites of each facet node. The facet node in Cu is defined as the site between the two $(-1\ -1\ 1)_A$ planes surrounding the emitted Shockley partial.

The facet node in Al is defined as the site between the two E units. The defects that appear at facet nodes (E units and Shockley partials) will be referred to as *facet node defects*. The term 'facet' by itself will exclusively apply to IBP and SBP facets during the coming discussion.

2.3.2 Overview of directionally-anisotropic mobility

Figure 2.4 shows mean grain boundary displacement as a function of time for the six unique simulations at T_H = 0.8, for both potentials (rows) and migration types (columns) over a time of 70 ps. Since the ADF magnitude is kept constant, the slope is directly related to mobility, with a steep slope signaling a high mobility. The slopes of both Al boundaries in Figure 2.4a and b are very similar to each other in magnitude. The slope for Type A Cu in Figure 2.4c roughly resembles what was observed in Al, but the Type B curve in Figure 2.4d is completely flat, signaling that the Cu boundary is initially immobile in one direction (when the ADF is applied to Grain B) within the same time span. Given enough time, the boundaries do eventually move, but with significantly lower velocities (slopes) than those of Type A. Figure 2.4e shows the two different modes of behavior by examining the displacement of a longer time. On the left side is the immobile phase, which is at least 100 ps long for T_H = 0.8. On the right side is the mobile phase, which shows the trajectories used to calculate mobilities (shifted to 0 ps in 'mobile time' to facilitate comparison). The clear difference between the Type A slopes for Cu in Figure 2.4c and the Type B slopes in the mobile phase of Figure 2.4e show that the Σ11 Cu boundary mobility cannot be uniquely defined by one mobility value, instead requiring two separate mobility values M_A and M_B to accurately capture its behavior.

Figure 2.5 shows the temperature-related mobility trends for both boundaries, first with mobility plotted as a function of temperature in Figures 2.5a and b and then with the same data

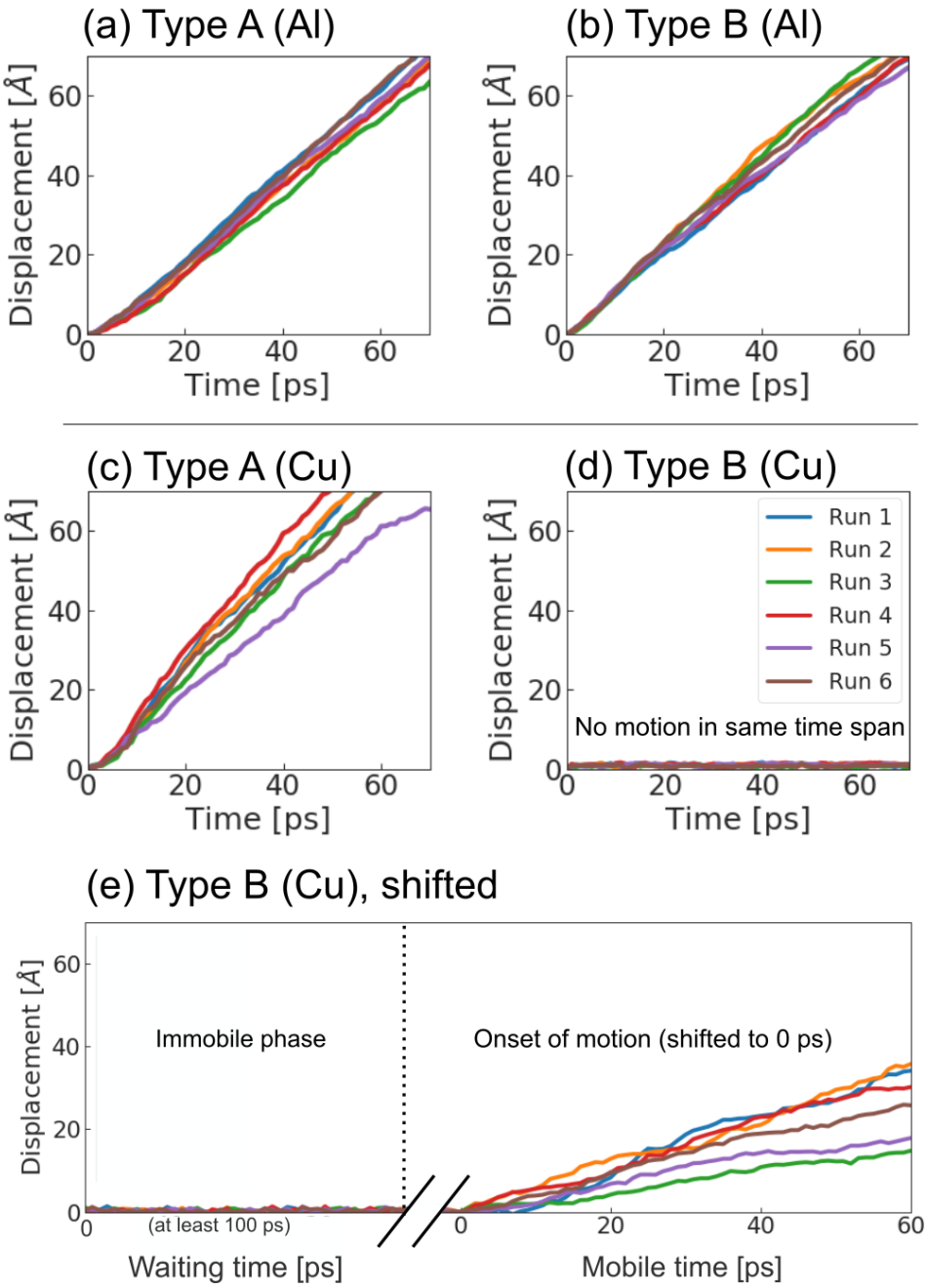

Figure 2.32. Trajectories of the Σ11 boundary in Al for (a) Type A and (b) Type B motion at T_H = 0.8, providing an example of directionally-isotropic mobility. (c) The trajectory of the Σ11 boundary in Cu undergoing Type A motion at T_H = 0.8. (d) The Type B trajectory for the Σ11 boundary in Cu over the same time shows a lack of migration. (e) Trajectories from longer time simulations of Type B motion in the Σ11 boundary in Cu show that the interface eventually moves but with a much lower slope/mobility. This boundary has an immobile phase (left) and a mobile phase (right). The axis is broken to indicate that the waiting times varied for different runs, and trajectories are shifted to the onset of steady-state velocity.

replotted in Arrhenius coordinates (log(M) as a function of inverse temperature) in Figures 2.5c and d. Error bars in all figures show the standard deviation around the mean value. For Al in Figure 2.5a and b (blue squares), mobility increases with increasing temperature in an essentially identical manner for both Type A and Type B motion. The Cu boundary (red circles) by contrast has varying temperature trends with motion type. In Figure 2.5a, the Type A first remains relatively constant and then decreases with increasing temperature. In contrast, Type B mobility increases with increasing temperature in Cu.

Though our study does not include a large enough temperature range to thoroughly analyze temperature-related mobility behavior in these faceted boundaries, there are a few trends from T_H = 0.8 to 0.9 worth exploring in more depth. The Arrhenius plots in Figure 2.5c and d allow for a clearer visualization of these trends. The different inverse temperatures for each material are shown on different axes, with Al on top in blue, and Cu on bottom in red. The Al curves in Figure 2.5c and d are both linearly decreasing Arrhenius curves that that appear to be consistent with thermally activated grain boundary motion [1, 16]. In contrast, the Cu curves have more complex temperature-mobility trends. To quantify these behaviors, we extract activation energy barriers (Q) from the mean values of these Σ11 curves, as well as those from a similar Arrhenius analysis of the Σ5 boundaries (not shown), with the results displayed in Table 2.2. According to the thermal classification criteria set up by Homer et al. [1], boundaries classified as thermally activated have values ranging from 0.01 to 1 eV. Since the majority of energies fall within this range, most of the boundaries studied here can be classified as thermally activated as well.

The major exception is the anisotropic Σ11 Cu boundary (first two rows of Table 2.2). Like the other boundaries mentioned above, the Type B-driven Σ11 boundary in Cu is also thermally activated. However, both of its energy barriers are a great deal higher than all other activation

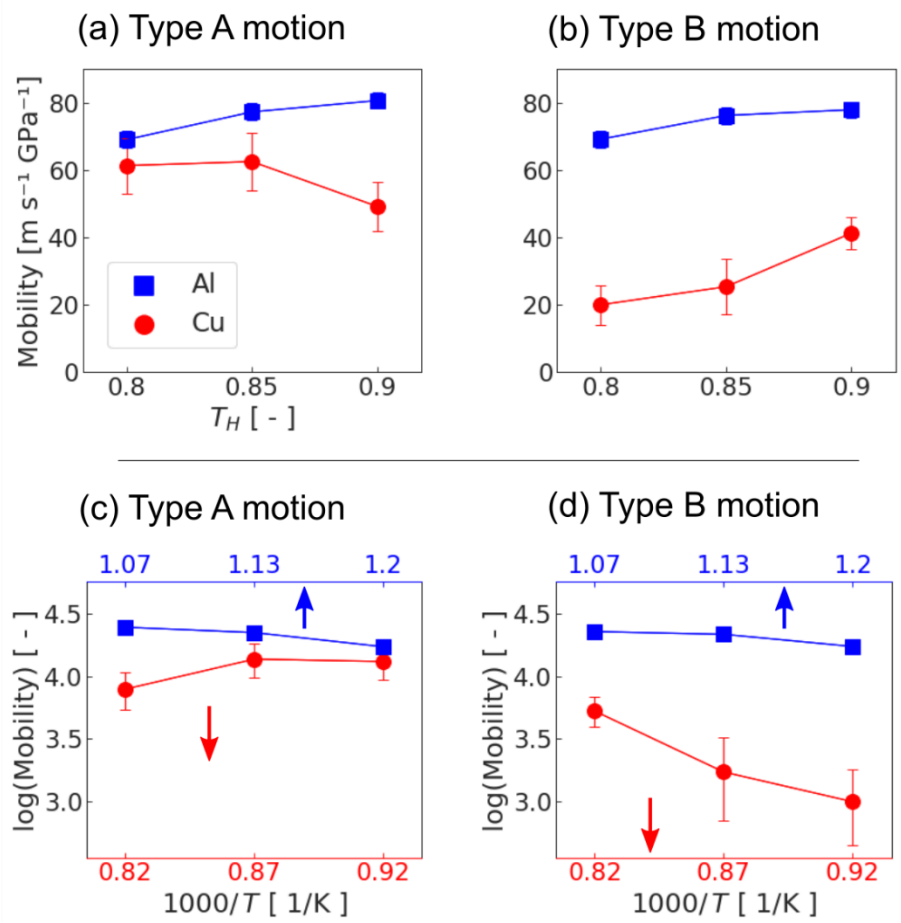

Figure 2.33. (a, b) Type A and Type B mobilities at different temperatures for Σ11 boundaries in Al (blue) and Cu (red). (c, d) Arrhenius plots showing the mobility for the same boundaries as a function of 1,000 / *T* for each material. The bottom (red) and top (blue) axes show the values for Cu and Al, respectively.

CSL type	Potential	Migration Type	Q [eV]
Σ11	**Cu**	**1 (faster)**	**-0.19**
		2 (slower)	0.65
	Al	1	0.10
		2	0.08
Σ5	Cu	1	0.10
		2	0.09
	Al	1	0.17
		2	0.14

Table 2.2. Activation energy barriers (Q) derived from Arrhenius analysis of mobility vs. temperature data for the Σ11 and Σ5 boundaries for each potential. Values of between 0.01 and 1 eV indicate that the boundary is thermally activated [1]. The negative activation energy of the anisotropic Type A-driven Σ11 boundary in Cu (bold) is consistent with thermal dampening.

energies observed here. While the Σ11 boundary in Al and the Σ5 boundaries all have activation energies lower than 0.2 eV, the Type B boundary has a significantly higher value of 0.65 eV. By contrast, the energy barrier for Type A (faster) migration has a negative value of -0.19, characteristic of thermally-damped motion. These contrasting behaviors in the Cu boundary indicate that it is not only directionally-anisotropic with respect to mobility, but also with respect to thermal motion behavior.

Though asymmetric tilt boundaries have been a part of many mobility studies (see, e.g., [1, 92, 93, 103, 104]), there have been few that mention mobility in different directions specifically. It is important therefore to establish a baseline of what is expected for typical asymmetric boundaries, by comparing the mobility trends of a relatively unremarkable asymmetric boundary to a faceted one. To accomplish this, we chose a non-faceted, asymmetric Σ5 <001> tilt boundary, shown at T = 0 K in Figure 2.6a and b for Al and Cu, respectively. The minimized structures are made of E units/kite-shape structures similar to those of Σ11 boundary in Al, as shown schematically in Figure 2.6c and d. Σ5 tilt boundaries have a predictable structure while also having energies similar to those of general high-angle interfaces [85, 108], which can be found in Table 2.1. Figures 2.6e and f show the as-annealed structures, where the addition of temperature leads to a qualitative loss of structural definition that the Σ11 boundaries do not undergo at the same homologous temperature, which can be partially explained by their relatively high energies compared to Σ11 boundaries (Table 2.1) and the interconnectivity of free volume between E units [10]. Simulations for the asymmetric Σ5 boundaries were run using identical parameters to those used for the Σ11 boundaries. In terms of mobility, shown in Figure 2.6g for Type A and Figure 2.6h for Type B, neither boundary exhibits the large differences that were observed for the

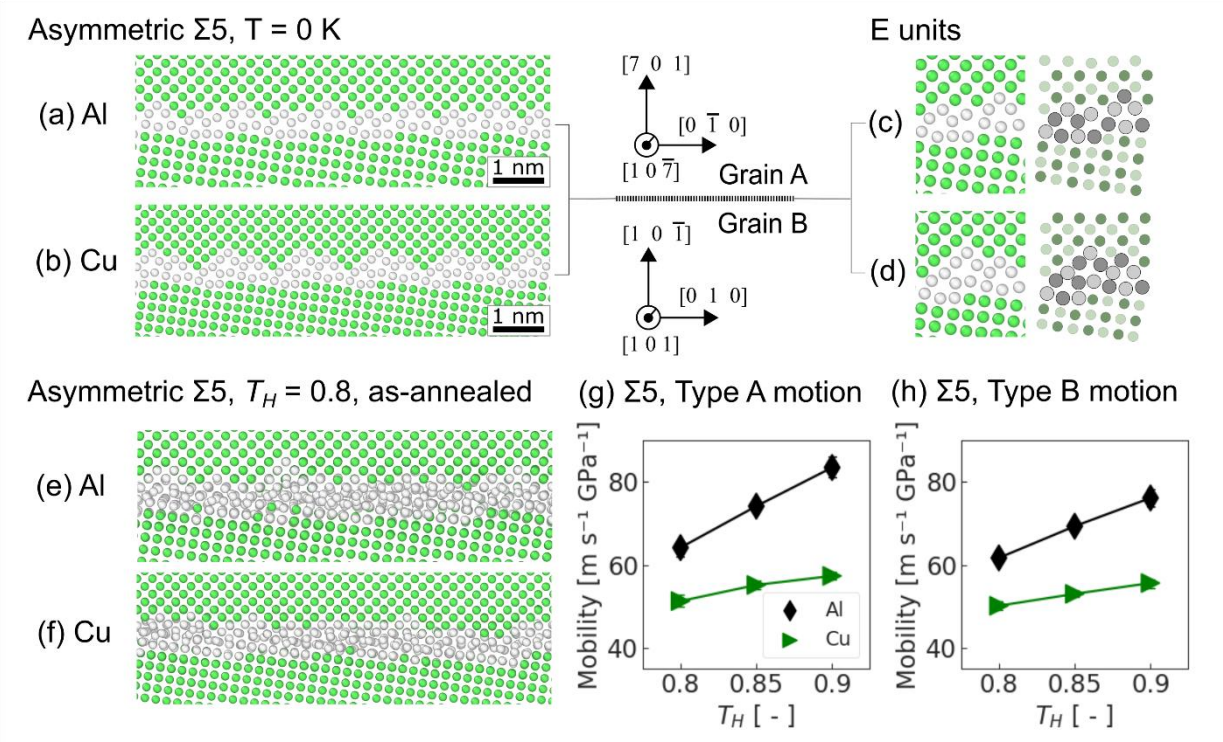

Figure 2.34. (a, b) The minimized (T = 0 K) asymmetric Σ5 boundaries in Al and Cu that are used as baselines for comparison. (c, d) Zoomed views show that both boundaries contain a series of E units. (e, f) The as-annealed asymmetric Σ5 boundaries at T_H = 0.8, where the structure becomes more disordered at elevated temperature. (g, h) Mobilities of asymmetric Σ5 boundaries in Al (black) and Cu (green) as a function of homologous temperature. All boundaries here demonstrate thermally-activated mobility trends.

Σ11 boundary in Cu. Analysis of temperature-mobility trends using Arrhenius plots (not shown) suggest that all of these boundaries move by a thermally activated mechanism.

The existence of boundary migration that is different in the two opposite directions means that two values mobility values, M_A and M_B, are needed based on the direction of boundary migration. To quantify and thus more precisely compare the relationship between Type A and Type B mobilities, we define the mobility anisotropy ratio, A, as:

$$A = max\left(\frac{M_A}{M_B}, \frac{M_B}{M_A}\right) \quad 2.3$$

In this form, *A* expresses how many times faster motion in one direction is than in the other. A mobility anisotropy ratio of 1 indicates that the mobilities of Type A and Type B-driven boundaries are identical. Values larger than 1 than that indicate the factor of increase or decrease for Type A mobility relative to Type B. The mobility anisotropy ratios for the various homologous temperatures and materials are plotted in Figure 2.7. The average anisotropy ratios in the Σ11 Cu boundary at T_H = 0.8 and 0.85 are far higher than the other boundaries, with average magnitudes of 3.3 and 2.8. Though this anisotropy is reduced significantly at T_H = 0.9, it is still somewhat elevated with a value of 1.2. A zoomed view of anisotropy values below 1.4 is shown in Figure 2.7b. All of the anisotropy values of the Σ11 boundary in Al and both Σ5 boundaries are below ~1.1. Overall, the Σ11 boundary in Al has the lowest anisotropy values, all lower than 1.05. The data shown in Figure 2.7b suggests that a typical or unremarkable asymmetric boundary would have mobilities that vary by 10% or less in the two opposite directions. The large deviation of the Σ11 boundary in Cu is therefore notable. Since the anisotropy values of the Σ11 boundary in Al

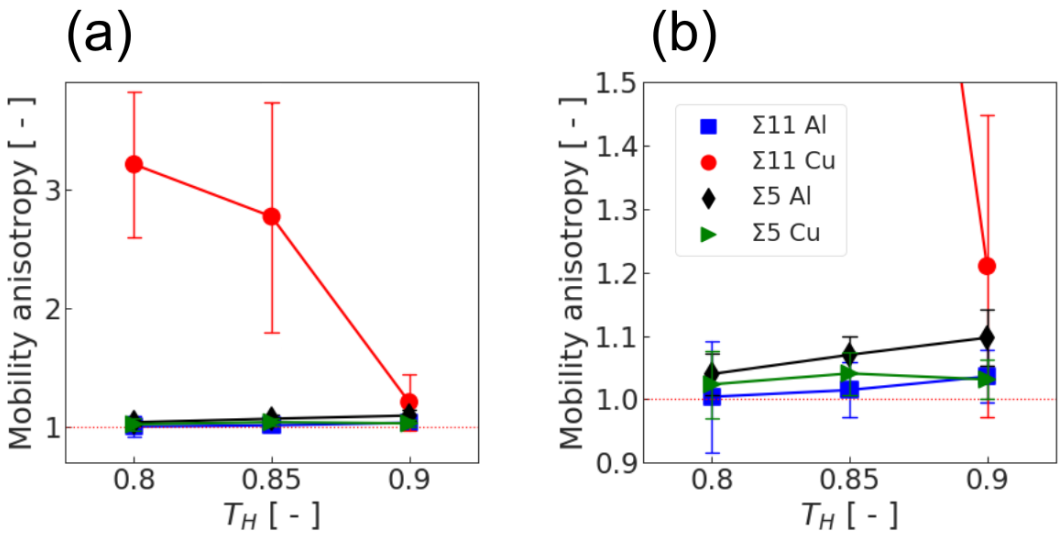

Figure 2.35. (a) The mobility anisotropy, A, as a function of temperature for both faceted Σ11 boundaries and asymmetric Σ5 boundaries in Al and Cu. (b) A zoomed view of the values with lower anisotropy, around *A* = 1.

lie close to 1, and beneath those of the Σ5 Al boundary, its anisotropy values fall within the range expected for a general asymmetric boundary. These findings align with the structural trends already observed above in the as-annealed boundaries shown in Figures 2.1 to 2.3. The E unit pairs present in the Σ11 boundary in Al are similar to those seen in the Σ5 boundaries for both potentials. The Σ11 boundary in Cu by contrast has the unique feature of emitted Shockley partials, and a uniquely high mobility anisotropy.

2.3.3 Introduction to faceted Σ11 shuffling modes

In this section, migrating Σ11 boundaries are observed in order to explore possible relationships between boundary structure and mobility anisotropy, with an initial focus on shared mobility mechanisms. Figure 2.8 presents a snapshot of Σ11 boundaries after the application of the ADF for 65 ps at T_H = 0.8. The Type A-driven and Type B-driven boundaries in Al in Figure 2.8a and b, respectively, are outlined in blue and the Type A-driven boundary in Cu in Figure 2.8c are outlined in red. The large gray arrows on the right side of each image indicate the direction of the applied driving force. In each image, one representative SBP facet and IBP facet have been labeled for reference. As with the as-annealed boundaries of Figures 2.2a and 2.3a, facets have been marked with brackets beneath each image and numbered from left to right. Each image is also labeled with the calculated mobility value for the boundary that is shown.

Figure 2.8 provides an overview of the evolution of structure in migrating Σ11 boundaries. In general, it is the defects at facet nodes, indicated by brackets beneath each boundary snapshot similar to those shown in Figures 2.2 and 2.3, that provide most of the boundary displacement. Even after significant migration, many features of the as-annealed boundary structures are still recognizable, but structural units originally native to only one element type now appear in both

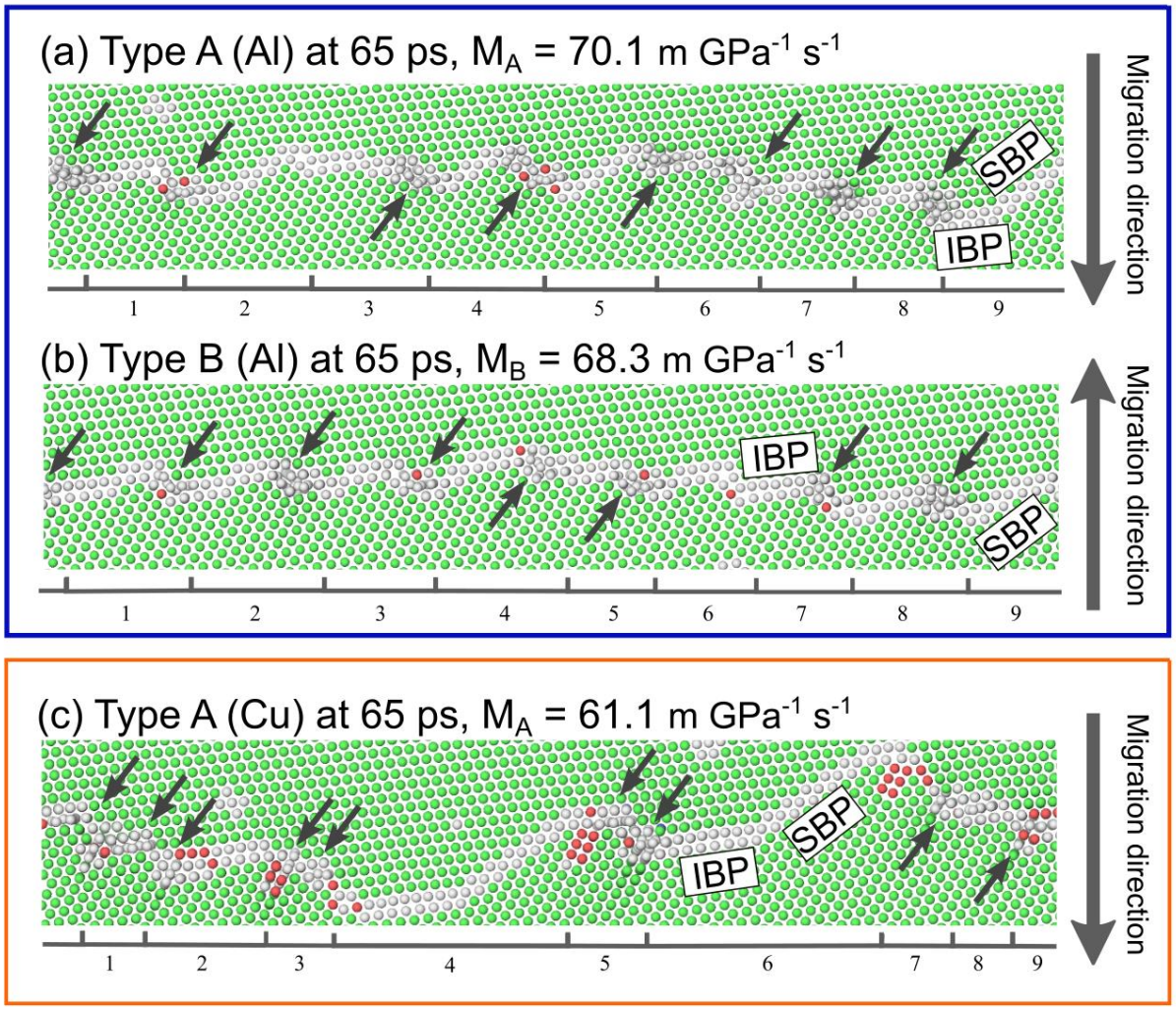

Figure 2.36. Snapshots of boundary motion at $T_H = 0.8$ for (a) a Σ11 boundary in Al undergoing Type A motion, (b) a Σ11 boundary in Al undergoing Type B motion, and (c) a Σ11 boundary in Cu undergoing Type A motion. These boundaries all move relatively smoothly and have 'normal' migration. The brackets beneath each snapshot indicate the location of facet nodes, and the numbers the respective facet period. The black arrows indicate facet nodes where atomic column dissociation has occurred.

elements with a high frequency. For example, the IBP facets, favored by Cu in the starting structure, are regularly observed in the Al boundaries during both Type A and Type B motion. Likewise, the Cu boundary has formed two SBP facets that were not present in the starting structure, likely as a consequence of the C unit compatibility between the two facet types mentioned above in Figure 2.3. In addition, the Type A-driven boundary in Cu has formed several

E units similar to those in the Al boundary, whereas it only had emitted Shockley partials in the as- annealed form. The black arrows in Figure 2.8 indicate facet nodes that have undergone atomic column dissociation, shown originally in Figure 2.2d, and recognizable by the disregistry of atoms along the tilt axis (Z-axis). The dissociation isn't unique to E units but can also be observed at Shockley partial emission sites in the facet nodes of the Cu boundary as well in Figure 2.8c. By comparing the boundaries of Figure 2.8, we learn that the only phenomenon truly unique to the Type A-driven boundary in Cu is the emission of Shockley partial dislocations. The atomic column dissociation seen in the as-annealed Σ11 boundary in Al is present at Shockley partial emission sites in the Cu boundary as well (black arrows in all snapshots), recognizable by the disregistry of atomic columns along the tilt axis (Z-direction). The only structures unique to the Type A-driven boundary in Cu are the emitted Shockley partials.

To better understand mobility anisotropy, two of the most common means of facet node migration are outlined. The first, common to the Σ11 in both Al and Cu and in both directions, is a complex atomic shuffle taking place in and near facet node defects, . This shuffling occurs when one or more atomic columns in a facet node defect dissociate as described earlier (Figure 2.2d), and when this occurs during migration it could be described as *disordered shuffling*. Two common variations of disordered shuffling are shown in Figure 2.9 at two different nodes, labeled Node 1 and Node 2. Tracking Node 1 in Figures 2,9a-c provides an example of an entire facet node involved in disordered shuffling, which is commonly observed in migrating Σ11 boundaries in Al. These facet nodes move somewhat slowly but only rarely re-associate into E unit pairs. Their local activity can encourage very slow-moving, non-dissociated E units, such as Node 2 in Figure 2.9a, to begin atomic column dissociation. Sometimes, as is the case here for Node 2 in Figure 2.9b to c, the dissociation starts on one column but does not propagate further and the node returns to its

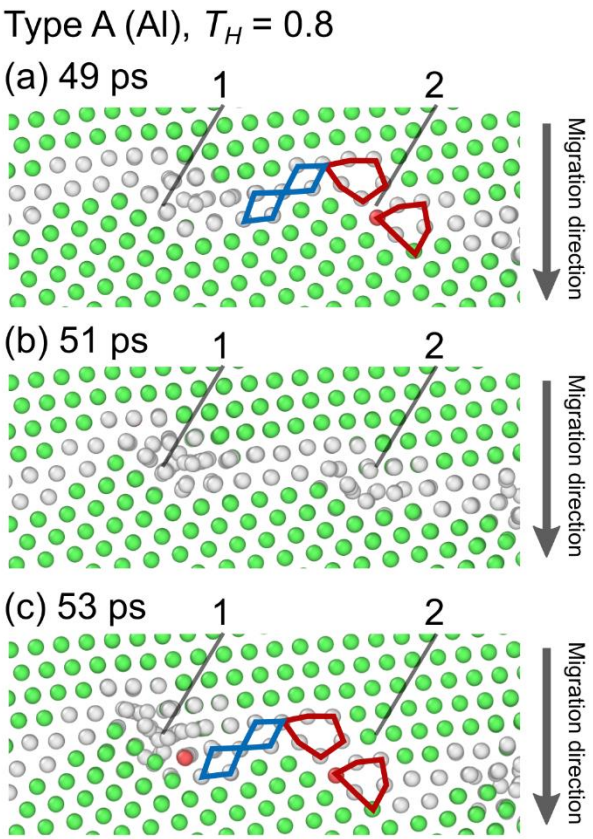

Figure 2.37. Demonstration of two kinds of disordered shuffling that may occur during facet node migration in the Σ11 boundary in Al during Type A migration at T_H = 0.8.

original form. Though the disruption of Node 2 does not result in a longer disordered shuffling process, the dissociation event in Node 2 does allow it to migrate it one plane height lower into Grain B by Figure 2.9c.

Disordered shuffling is common to all migrating boundaries and is the only means of facet node migration seen in the Σ11 boundaries in Al. The facet nodes of Σ11 boundaries in Cu migrate using this mechanism as well but also move via cycles of Shockley partial dislocation emission and contraction. Shockley partial contraction, also called stacking fault constriction, is a process in which an emitted Shockley partial recedes into the interface, forming a new E unit pair in the process. One full cycle of Shockley emission and contraction at a facet node, which could be

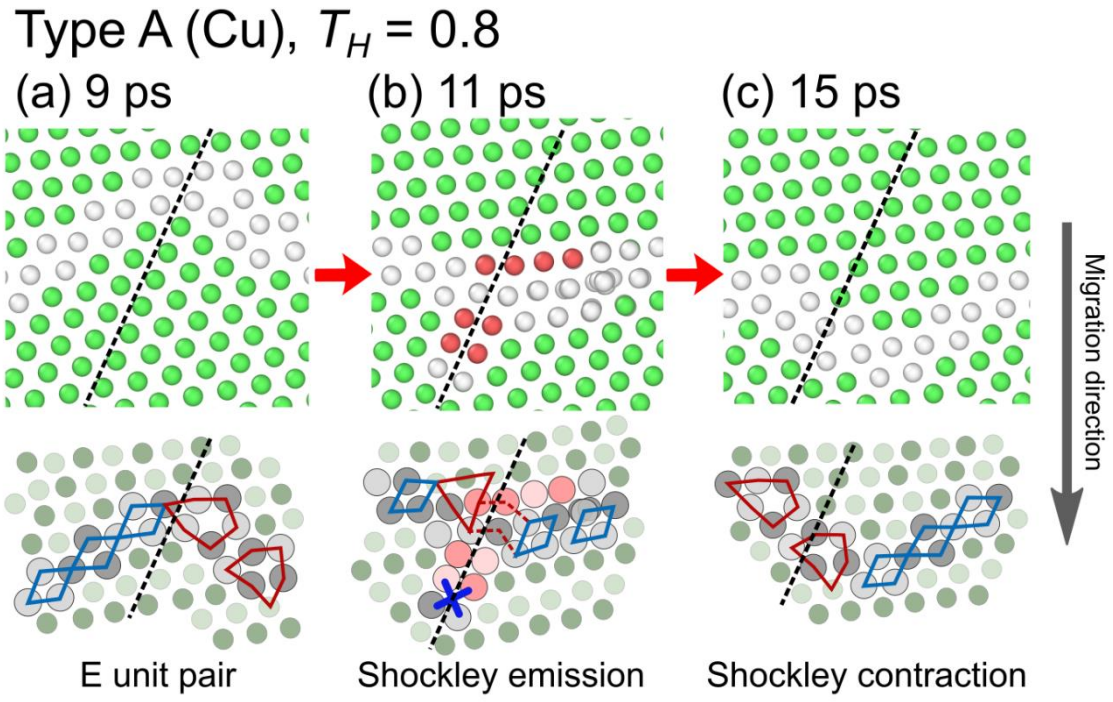

Figure 2.38. Demonstration of the Shockley partial emission/contraction process at a facet node (Shockley shuffling) during Type A migration of a faceted Σ11 boundary in Cu at T_H = 0.8.

called *Shockley shuffling* to distinguish it from disordered shuffling, is shown in Figure 2.10. The black dotted line indicates the orientation of the (-1 -1 1) plane in Grain B along which stacking faults are emitted, and also serves as a reference to mark the initial position of the nodes. To begin a cycle, an E unit must be present, such as that shown in Figure 10a at 9 ps. At 11 ps, the E unit has emitted a Shockley partial, creating a short stacking fault in Grain B (Figure 2.10b). Finally, the Shockley partial contracts back into the boundary, re-forming an E unit pair centered around the site of Shockley emission (Figure 2.10c). From this point, the E unit may undergo atomic column dissociation and begin moving via disordered shuffling or begin another cycle of Shockley shuffling. Like disordered shuffling, the stages of Shockley shuffling process are the same for both Type A and Type B motion.

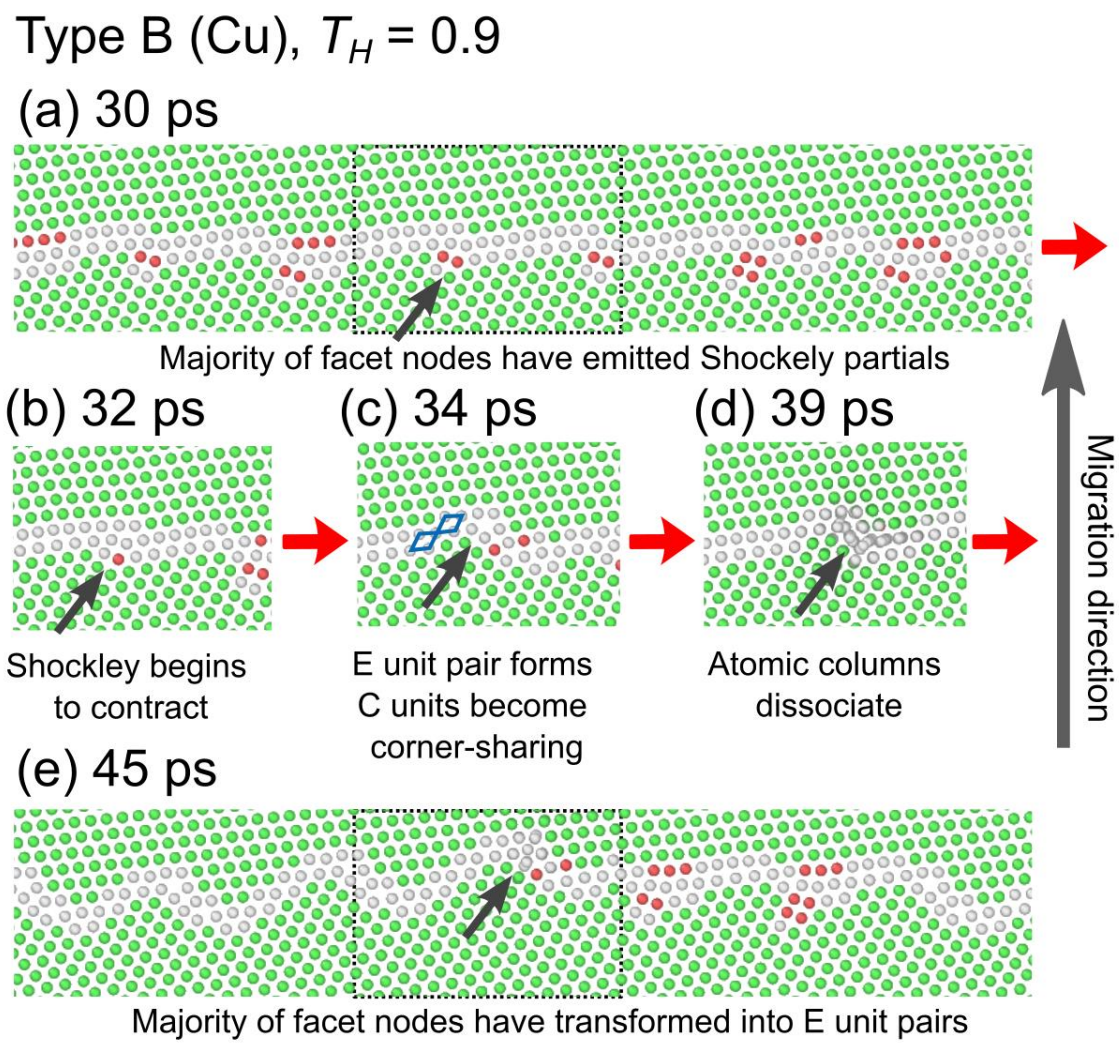

Figure 2.39. The transition from the immobile phase to the mobile phase for Type B motion in a Σ11 boundary in Cu at T_H = 0.9 is shown. (a) The end of the immobile phase, 2 ps before the transformation of a Shockley partial into a dissociated atomic cluster (b)-(d). € A snapshot of the boundary at the beginning of the mobile phase.

Having understood the general means of facet node defect migration in Σ11 boundaries in Al and Cu, we now move to understand the immobile and mobile phases of Type B-driven motion in Cu. Figure 2.11a shows one such boundary at the very end of its immobile phase. The boundary morphology remains near identical to that of the as-annealed form in Figures 2.1c, 2.3a, and 2.3c. In order to begin motion, one or more Shockley partials has to contract into the boundary, as shown

in Figures 2.11b and c, resulting in E unit pairs appearing a few step heights above the original site of Shockley partial emission (Figure 2.11c). Once in steady-state motion, as seen in Figure 2.11e, it takes on the same structures observed in the other mobile boundaries in Figure 2.10, moving via the same Shockley and disordered shuffling processes at facet nodes.

As can be seen in Figure 2.11b and c, the precipitating event to the beginning of Type B migration is the contraction of the Shockley partial dislocation at a single facet node back into the boundary. This suggests that the length of the immobile phase is correlated with the kinetics of Shockley partial contraction. Work by Bowers et al. [23] on a boundary similar to the IBP provides experimental and computational data that is useful for understanding the contraction reaction in a boundary with very similar defect morphology. Using HAADF-STEM, Bowers et al. observed the migration mechanisms of a disconnection traveling along a {001}/{110} incommensurate <110> tilt boundary in Au. These boundaries are populated by a series of what are described as a "five-fold defects," which in the SUM interpretation would be E (or E') units. Like the E units at facet nodes in the current work, the E units at certain disconnection sites in the Au boundary could emit Shockley partials to relax, which pin the disconnection until the partial contracted to form an E unit once more. Inspection of the HAADF-STEM images in the frames before the contraction reaction revealed blurring of atomic columns near the base of E units surrounding the disconnection, which Bowers et al. postulated was due to agitated atoms fluctuating in the local free volume. We note the similarity of this blurring description to atomic column dissociation seen in the boundaries studied in this work. The fact that Bowers et al. hypothesized that these fluctuations were associated with point defect diffusion within the E unit would also be consistent with atomic column dissociation, as we have also observed atomic hopping between grains within the E unit's volume during dissociation.

Bowers et al. also undertook a detailed molecular dynamics study of the emitted Shockley partial's transition to an E unit. They speculated that the observed atomic fluctuations in and around local E units leads to kink nucleation, which in turn initiates Shockley partial contraction. An analysis of the energetic transition path from emission to contraction and back to emission revealed that the contraction occurred at the peak of the energy curve (with an energy barrier of approximately 0.42 eV), meaning that contraction is the rate-limiting process to beginning disconnection migration. Though there are important crystallographic differences between the incommensurate boundary disconnections in Au and the Σ11 facet nodes in Cu, we believe that the same basic rate-limiting mechanism operates in our boundary as well. The initial immobile phase preceding migration (shown in Figure 2.4e) could then be understood as the time necessary to nucleate the initial Shockley contraction event in a single facet node such as that in Figure 2.11b. That event then leads to a cascade of structural changes (Figure 2.11c through e) which could theoretically lower the initial energy barrier for Shockley contraction at other facet nodes.

Since Type A migration begins with the same array of emitted Shockley partials at facet nodes, it could theoretically also have an immobile phase and the same Shockley partial contraction reaction at a facet node to begin motion. However, Type A-migrating boundaries have no immobile phase and move on average with a much higher velocity. This suggests that there may be another mechanism operating in this direction of motion. After investigating multiple migrating boundaries in great detail, one can observe that the Type A motion in Cu not only migrates via shuffling at the facet nodes, but also takes advantage of the C unit compatibility outlined in Figure 2.3d to migrate the facet directly. This process allows the boundary to migrate by replacing an IBP facet with a stacking fault in Grain A via C unit unfolding, which in turn is accomplished through small shuffles of each atomic column in the C units. Because the creation

of these stacking faults is enabled by the presence of the $(111)_A$ slip plane within the IBP facet, this mechanism could be described as *slip plane shuffling*. This mechanism is the primary means of boundary migration in the first 10-20 ps after application of the Type A ADF in the Σ11 boundary in Cu. The initial step of slip plane shuffling is shown in Figure 2.12a at the very beginning of a Type A simulation. The process continues in Figure 2.12b with the unfolding of another C unit, creating a full SBP facet and elongating the growing stacking fault. The third step is the contraction of the Shockley partial into the boundary in Figure 2.12c, leading to the creation of an E unit pair and SBP facet that are very similar to those observed in the as-annealed boundary in Al. Figure 2.12d shows an example of the high frequency of slip plane shuffling already present at 5 ps. From this point onward, facet migration may proceed in several different ways, through Shockley or disordered shuffling). In most cases, the stacking fault disappears upon further motion (denoted by the black arrow). Slip plane shuffling can also be observed in Type A and Type B migrating boundaries when moving facet nodes are at approximately the same height with respect to the Y-direction, as shown in the boundary snapshot of Figure 2.12e at 43 ps.

2.3.4 Slip plane shuffling and directionally-anisotropic mobility

Taken together, Figures 2.11 and 2.12 can provide an explanation as to why slip plane shuffling is not a mechanism available during Type B migration in Cu. The directionality of the C unit (which is oriented along the inclination angle $\beta = 35.3°$) restricts the ways in which IBP and SBP facets can connect to each other. Specifically, they both may only act as ascending planes (going from left to right in the figures of this paper) along the $(111)_A$ slip plane of the IBP facet and C unit folding/unfolding must necessarily follow the same rules. As shown in Figure 2.12 above,

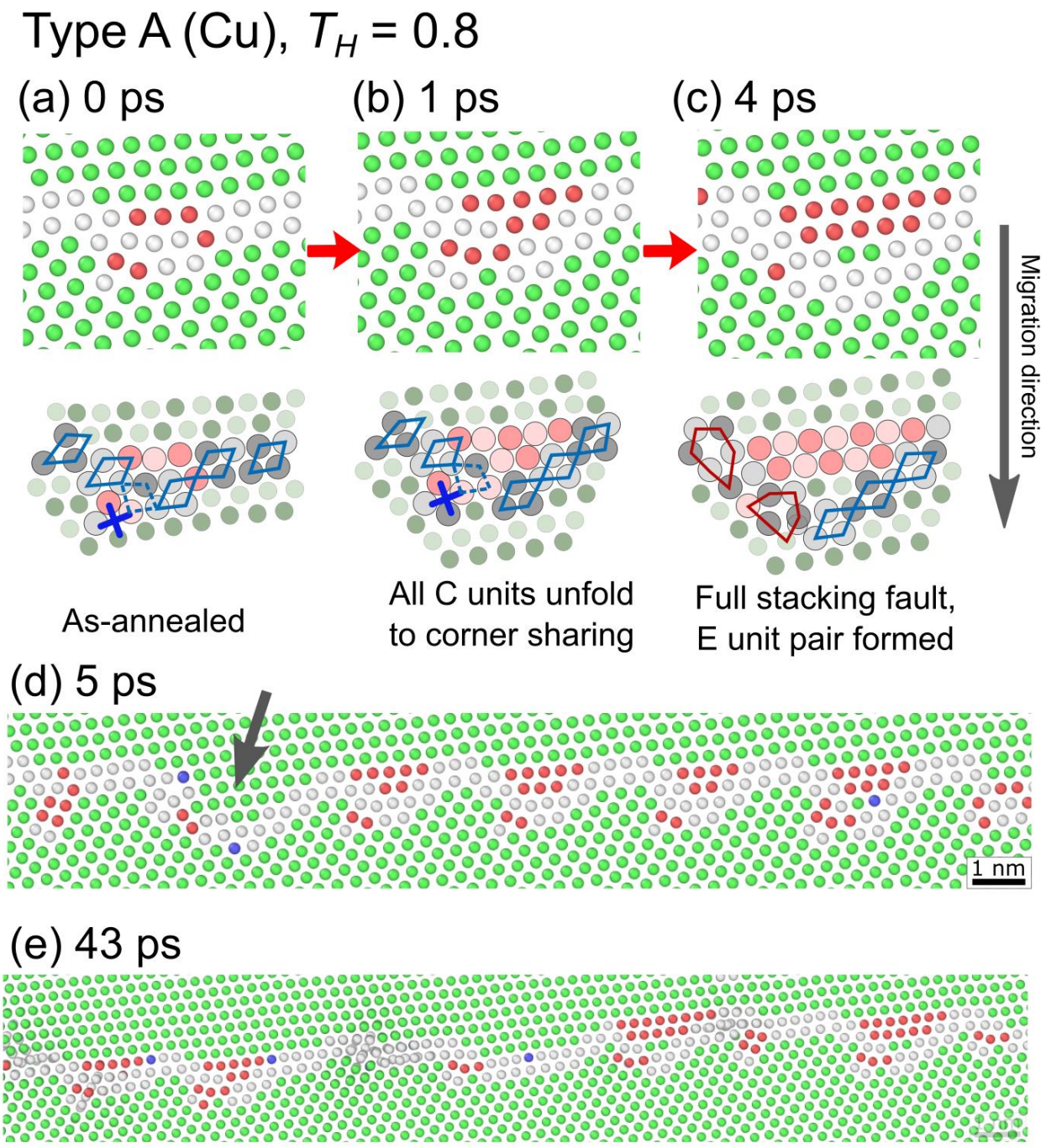

Figure 2.40. An overview of the process of stacking fault shuffling, which (a)-€ dominates Type A motion in the first 5 ps but (h) also occurs throughout all Type A migration simulation runs. Type A motion in a Σ11 boundary in Cu at T_H = 0.8 is shown.

the unfolding of an IBP facet from left-to-right preserves this ordering. Type B migration on the other hand would be attempting to refold the C units in reverse order (going from the state shown in Figure 2.12c to the state in Figure 2.12a). At that point, since C units in the IBP's center or right side cannot move without breaking up the IBP (and creating forbidden descending facet segments), it is the facet node which must migrate, necessitating a transformation of the node defects. This was observed directly in Figures 2.11b-d, where the boundary is immobilized under the Type B ADF until Shockley partial contraction occurs at a facet node.

The slip plane shuffling mechanism can also explain the isotropic mobility of the Σ11 boundary in Al. This interface has identical boundary asymmetry in terms of C units and IBP facets and must therefore follow the same migration rules. However, its higher stacking fault energy means it does not emit stacking faults. Its mobility is thus limited only by the rate of E unit-based disordered shuffling. This implies that directionally-anisotropic mobility in Σ11 boundaries in Cu is not a result of Type B being slower than Type A, but rather a result of Type A migration being faster. The Type A-specific slip plane shuffling mechanism allows facet nodes to bypass a Cu-specific rate-limiting facet node migration step that can slow movement, namely Shockley partial contraction.

To confirm that slip plane shuffling is occurring at a rate that is able to influence mobility during steady-state migration, we used the fact that it creates, per facet, more HCP-coordinated atoms than Shockley shuffling does. A typical emitted Shockley partial contains approximately 24 to 56 HCP-coordinated atoms per facet (2 to 4 atomic columns with 14 HCP atoms per column), while facets undergoing slip plane shuffling tend to create between 42 to 154 HCP-coordinated (3 to 11 columns) per facet, depending on the part of the cycle they are in (see Figures 2.12a-c). Using this reasoning, the statistics of atom types can be investigated to get a sense of how

frequently slip plane shuffling is occurring during the simulation. If this kind of shuffling is occurring at an increased rate compared to Shockley shuffling during Type A motion, one would expect to observe that the number of HCP atoms is higher than that of Type B.

Figures 2.13a-c show the number of HCP-coordinated atoms for the Σ11 boundaries in Cu for each homologous temperature (columns) and motion type (colors). The first 20 ps after the start of each run is left out to exclude the initial increased rate of slip plane shuffling shown in Figure 2.12g and atom counting was only conducted during steady-state mobility regimes. Each plot contains the information of 12 samples (6 bicrystals with 2 boundaries) for each boundary motion type over a span of 50 ps, with the number of HCP atoms measured every 1 ps. Therefore, any number quoted in this figure is an instantaneous measurement of the number of HCP atoms in grain boundaries of the simulation cell. Except for emitted Shockley partials, out-of-boundary HCP atoms were not counted. The top row shows histogram of HCP atom count for each motion type, while the bottom row shows the cumulative distribution functions for this same data. For the two lower homologous temperatures (Figures 2.13a and b), Type A motion (red) results in a wider distribution of HCP-coordinated atom counts than that of the Type B motion (blue). The mean HCP atom counts for Type A migration (red vertical lines) are also higher than those of Type B (blue vertical lines). This trend can also be observed in the cumulative distribution functions for Type A motion, where the red curves have shifted to the right of the Type B curves, indicating that more HCP atoms have appeared on average during Type A motion. We can therefore conclude that slip plane shuffling is occurring at a significantly higher rate during Type A migration than in Type B for the two lowest temperatures studied here. Given the connection between slip plane shuffling and boundary asymmetry, it is likely that this increased occurrence of shuffling is also the source of the higher velocities seen in Type A migration versus Type B. Thus, slip plane

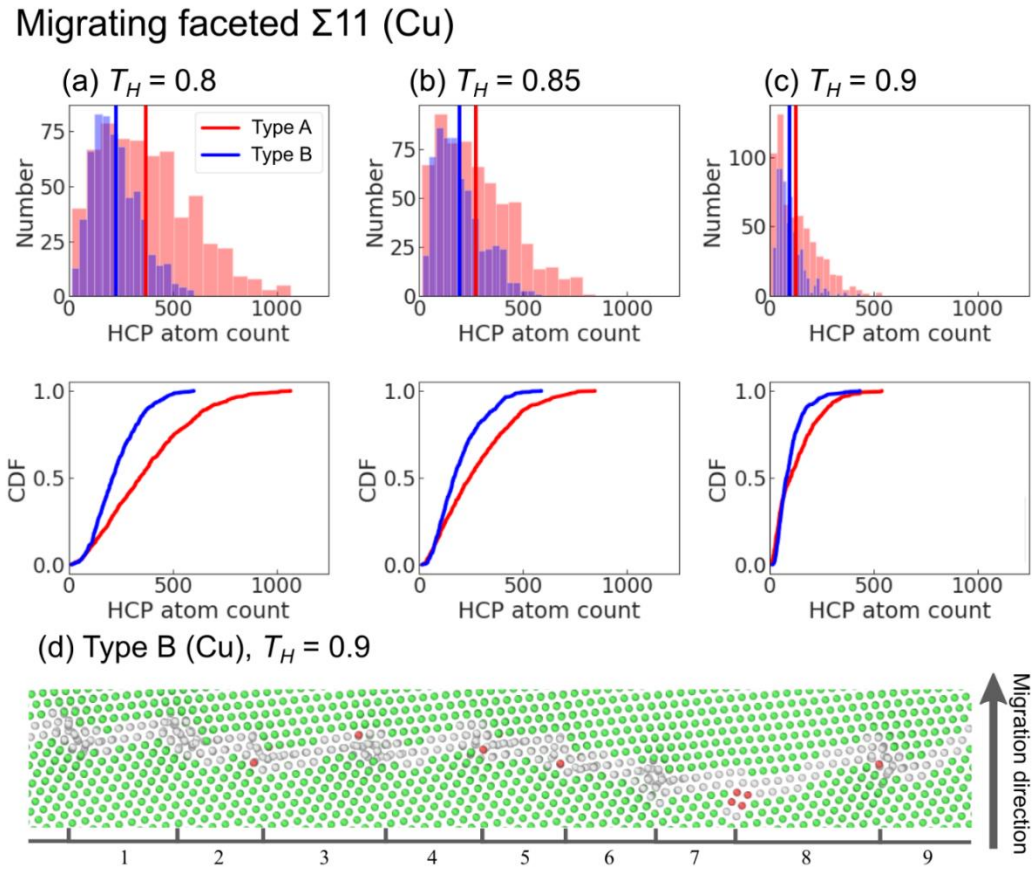

Figure 2.41. (a-c) Tracking the population of HCP atoms in the simulations at specific times during migration, in both histogram and cumulative distribution function form for Type A (red) and Type B (blue) motion. The solid colored lines in the histograms show the mean values for each direction. Wider distributions and mean values that are shifted to the right indicate that slip plane shuffling is more active during Type A motion. (d) A moving Type B-driven boundary where Shockley shuffling is suppressed, allowing for rapid migration.

shuffling can be identified as the primary mechanism responsible for the directionally-anisotropic mobility in the Σ11 boundaries in Cu at T_H = 0.8 and 0.85.

2.3.5 Temperature-mobility trends and directionally-anisotropic mobility

Figure 2.13c reveals a possible explanation for the reduction in mobility anisotropy at T_H = 0.9. At this temperature, the distribution of HCP atoms during Type A motion undergoes a noticeable shift when compared to the two lower homologous temperatures. Overall, the number of HCP-coordinated atoms shifts towards the lowest range of the histogram and the Type A and

Type B curves in the cumulative distribution function beneath it begin to overlap. The boundary snapshot in Figure 2.13d shows that the majority of facet nodes consist of E unit pairs with atomic column dissociation. In other words, the nodes in Cu at the highest homologous temperature resemble those of the Σ11 boundary in Al at lower homologous temperatures, which has little to no mobility anisotropy and no Shockley shuffling. The stark decrease in Shockley partial emission at facet nodes due to increased temperature is consistent with what was physically observed in the hybrid HAADF-STEM/molecular dynamics study of disconnection motion by Bowers et al. [23] discussed above in Section 3.3. Recall that an analysis of Shockley contraction in the incommensurate Au boundary supported the idea that this feature is nucleated by point defect diffusion within the free volume of E units. Since increasing temperature also increases point defect diffusion, energy barriers to Shockley contraction are more rapidly overcome. Additional evidence for an increase in Shockley partial contraction (and decrease in Shockley partial emission) can be found when comparing the cumulative HCP atom counts for both Type A and Type B migration at each temperature, or the area under the curves. The areas of each histogram plot become smaller with increasing temperature, indicating a decrease in the total number of HCP atoms counted during migration. Because the number of Σ11 facet nodes remains constant, we conclude from this data that Shockley and slip plane shuffling are suppressed. This makes disordered shuffling the dominant migration mechanism in the Σ11 boundary in Cu (as it is in the Σ11 boundaries in Al), leading in turn to a corresponding reduction in the mobility anisotropy.

The structural transitions from Shockley and slip plane shuffling modes to disordered shuffling can also explain the directionally-dependent temperature-mobility trends in the Σ11 boundary in Cu noted above in Figure 2.5 and Table 2.2. Recall that the activation energy barriers from Table 2.2 revealed Type A motion to be thermally damped (decreasing mobility with

increasing temperature) and Type B motion to be thermally activated. One possible explanation for both trends could be that the transition to disordered shuffling represents a "facet node roughening" analogous to the well-documented phenomenon of boundary roughening [27, 28, 39]. Above the 'roughening temperature' T_R, boundaries generally see an increase in their mobility, which is what is observed for the Type B-driven boundary to occur by T_H = 0.9. However, roughening can also lead to decreases in mobility like that observed in a variety of thermally-damped and anti-thermal boundaries [48, 106, 111, 112]. Studies of the dynamic structures of these interfaces uncover highly ordered atomic shuffling mechanisms that enhance mobility [48]. In those cases, thermal roughening leads to a decrease in mobility when the ordered atomic shuffling becomes disrupted. Similarly, increased temperatures lead to the loss of the ordered, IBP-based slip plane shuffling mechanism in the Type A motion direction in Cu, causing it to also lose its mobility advantage over Type B (which only has Shockley and disordered shuffling at facet nodes). The intriguing similarities between atom-level shuffling activity on slip planes (such as microrotation around CSL atoms ([43, 44]) and shuffling involving entire slip planes and Shockley dislocations (such as the shuffling in the faceted Σ11 boundaries in Cu, or the anti-thermal boundaries explored by Humberson et al. [4, 44]) invite future exploration of the role of {111} planes in asymmetric boundary mobility.

2.4 Summary and conclusions

In this chapter, molecular dynamics simulations were used to uncover the phenomenon of directionally-anisotropic mobility in a faceted <110> tilt Σ11 boundary in Cu with an inclination angle of β = 35.3°. By comparing its features to boundaries with isotropic mobility, namely a

faceted Σ11 boundary in Al and asymmetric Σ5 boundaries in both Cu and Al, the following conclusions can be drawn:

- Asymmetric Σ11 boundaries in Cu can exhibit clear variations in boundary mobility depending on the direction of migration. Motion in one direction was found to be up to three times slower than migration in the other direction. In addition, an immobile phase that was characterized by a long time lag before migration began was observed in many of the slow boundaries. The different motion directions also exhibit different temperature-mobility trends.
- Faceted Σ11 boundary structures, both when stationary and while in motion, can be characterized using only two structural units: (1) C units and (2) E units. The Cu potential with its lower stacking fault energy also emits Shockley partials, which can contract to form the same E unit pairs seen in the facet nodes of the Σ11 boundary in Al.
- SBP and IBP facets are comprised of C units with different relative alignments. This makes boundary transformations between SBP and IBP facets relatively easy, but with a strict orientation set by the inclination angle, β.
- There are three distinct ways in which facet migration can occur in the faceted Σ11 boundaries in general, which we define with the term *shuffling modes*. Each mode is associated with transformations of C units, E units, and emitted Shockley partials, alone or in combination:
    - *Disordered shuffling* is a process in which E unit pairs, which appear in both Al and Cu, can undergo atomic column dissociation, which then moves the facet node.
    - *Shockley shuffling* occurs only in the Σ11boundaries in Cu and is named after the cycles of Shockley partial emission/contraction that can occur at facet nodes (along with disordered shuffling).

- *Slip plane shuffling* is migration via the transformation of the IBP facet itself via the folding/unfolding of C units. It accomplishes this in combination with Shockley shuffling. It is unique to Type A motion in the Σ11 boundary in Cu, which arises from the orientation and compatibility of C units shared between the SBP and IBP facets.

- The slip plane shuffling mechanism provides a clear explanation for the pronounced directionally-dependent mobility observed at T_H = 0.8 and 0.85.
- The magnitude of the mobility anisotropy ratio A is much smaller in the Σ11 boundary in Cu at T_H = 0.9. We conclude that this is caused by thermal roughening at facet nodes, which increases the rate of Shockley contraction and appears to also inhibit slip plane shuffling. Without slip plane shuffling, the "fast" boundary becomes slower. The roughening simultaneously increases the mobility of the slower boundary, leading to a significant drop in A.

The directionally-anisotropic mobility observed in this faceted Σ11 boundary in Cu underscores the need for atomistic-level study of grain boundary migration. This anisotropy arises directly from the atomic structure of the boundary, motivating a deeper exploration of faceted boundaries in general. The role of {111} grain boundary planes in faceting and mobility could be a particularly fruitful topic of future study. Understanding the impact of unusual migration behavior such as antithermal/athermal mobility trends and anisotropic mobility on microstructural evolution could provide useful insights into phenomena such as abnormal grain growth.

3 Shuffling mode competition leads to directionally-anisotropic mobility of faceted Σ11 boundaries in face centered cubic metals

3.1 Introduction

In the previous chapter, the concept of shuffling modes was established to describe the primary motion mechanisms of one faceted Σ11 boundary in two different materials, namely Cu and Al. Additionally, the phenomenon of directionally-anisotropic mobility was discovered in Cu, and found to be a function of the unique geometry of the Σ11 facets at β = 35.3°. Though intriguing, it is unclear whether these results are generalizable beyond the single boundary and potentials used. To expand on the insights gained in Chapter 2, a systematic study of mobility is undertaken. By varying the inclination angle, temperature, and FCC potentials (Al, Cu, and Ni) used, we investigate whether the three shuffling modes outlined in Chapter 2 remain active in the new, larger dataset, with an aim to further explore the physical underpinnings of directionally-anisotropic mobility.

3.2 Methods

Chapter 2 explored grain boundaries generated from a single inclination angle. Recall that faceting in that chapter was induced by maintaining the Σ11 misorientation, but tilting the boundary plane inclination angle away from the SBP (from β = 0° to β = 35.3°). The same process was used in this work to generate three additional inclination angles, for a total of four unique bicrystal configurations spaced approximately 10° apart from each other (β = 15.8°, 25.5°, 35.3°, and 46.7°), shown in Figure 3.1 with the SBP snapshot for reference. An example of a Ni-1, β = 15.8° boundary at a homologous temperature of T_H = 0.8 is also shown with its potential energy

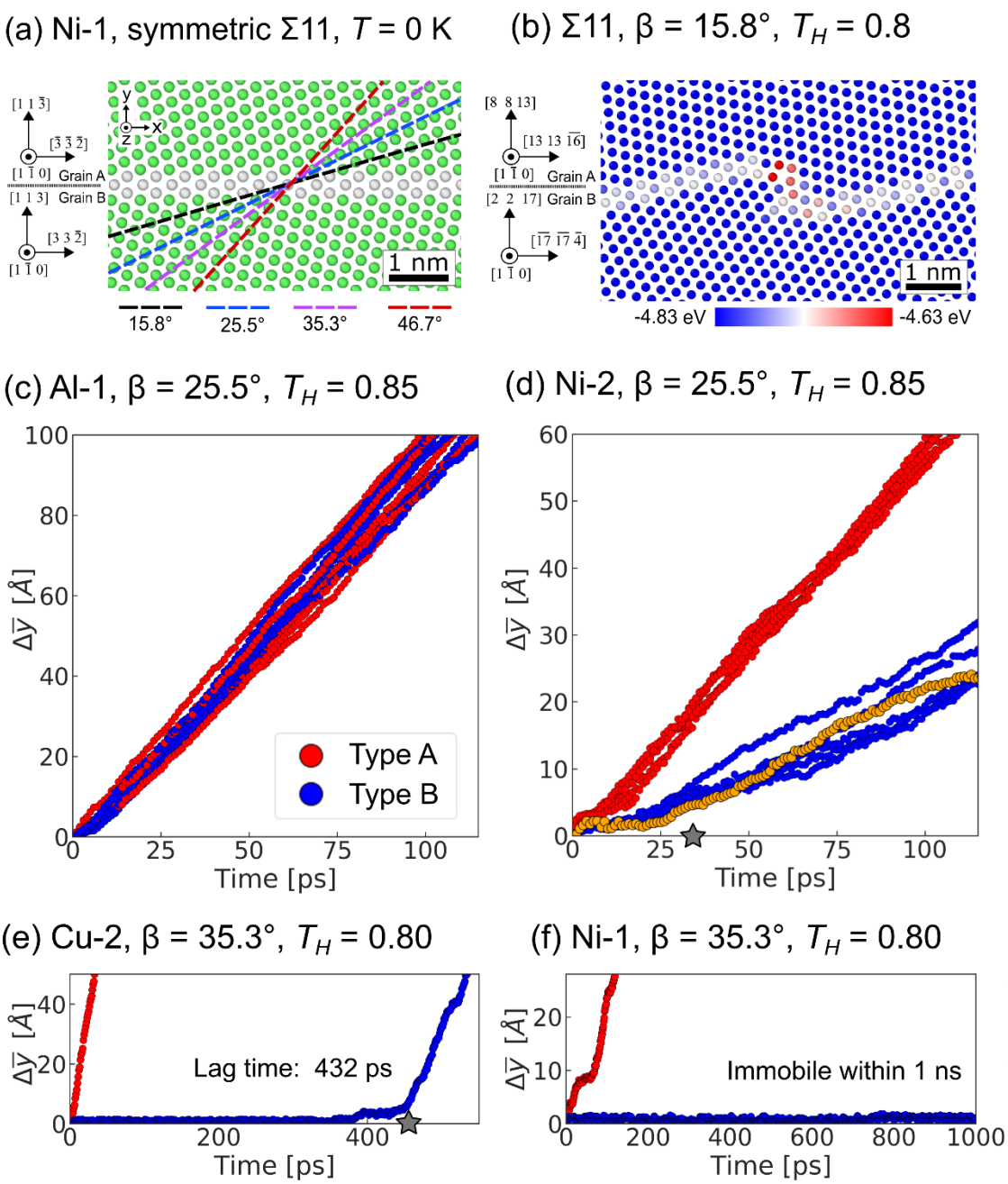

Figure 3.42. (a) Symmetric Σ11 <110> tilt boundary. Asymmetric boundaries were created by varying the boundary plane inclination angle β from the 0° symmetric configuration to the four angles indicated by the colored dashed lines. (b) Potential energy profile of a faceted boundary with β = 15.8° (black dashed line in (a)). (c) Average boundary displacement versus time in which Type A (red) and Type B (blue) have the same mobilities (i.e. slopes are the same). (d-f) Examples of directionally-anisotropic mobility, where the red and blue slopes are different. Many Type B boundaries have significant immobile phases (t_{lag}), as indicated by grey stars. An example of a simulation run with a lag time in (d) is highlighted in orange. (f) A Ni-1 boundary that is immobile within the time frame chosen for this work (1 ns).

profile in Figure 3.1b. As in Chapter 2, one asymmetric, but not faceted, Σ5 <100> tilt bicrystal was created and tested as a control sample.

Three different face centered cubic elements (Al, Cu, and Ni) were selected and each represented with two different embedded-atom model (EAM) potentials, for a total of 6 materials, probed in this study. We refer to these potentials as Al-1 [113], Al-2 [99], Cu [1]-1 [114], Cu-2 [100], Ni-1 [115], and Ni-2 [113] in the subsequent text. The variety of metals was selected to sample materials with a shared face centered cubic crystallography but provide variation in other properties such as lattice constant, grain boundary energy, and stacking fault energy. A selection of their properties is included in Table 2.1. The numbering per element is assigned based on ascending order of stacking fault energy. For example, the Al-1 potential has a stacking fault energy of 117 mJ/m^2, which is lower than Al-2's at 146 mJ/m^2. Melting temperatures were calculated using the method outlined by Wang et al. [101], and the symmetric Σ11 (β = 0°) boundary energies calculated using the methodology of Tschopp et al. [85] outlined in Chapter 2.2.

We make special note here that the data of the two boundaries studied in Chapter 2 is included in this dataset as well. Recall that both boundaries in that chapter were at an angle of β = 35.3° (the third of four inclination angles studied), and the equivalent interatomic potential names would be Cu-2 and Al-2 for the Chapter 2 Cu and Al boundaries, respectively. That relationship is also noted in Table 2.1 with doubled asterisks (**).

The four bicrystal variants were created using the methods outlined in detail in Chapter 2.2. As described there, using the criteria provided by Deng and Deng [104], we determined that a minimum Ly length of 30.0 nm would be acceptable for the four Σ11 bicrystals under study (actual range used was 31.4 nm to 42.8 nm). The length of the dimension parallel to the boundary

Potential Name	**a_0 [Å]***	**γ_{SF} [mJ/m^2]***	**T_{melt} [101] [K]**	**Energy, Σ11, β = 0° [mJ/m^2]**
Cu-1 [114]	3.639	26	1352	353.3
Cu-2** [100]	3.615	44	1357	309.9
Ni-1 [113]	3.52	82	1995	533.1
Ni-2 [99]	3.52	103	1635	465.9
Al-1 [113]	4.05	117	850	104.1
Al-2** [99]	4.05	146	1035	150.8
* Values taken from reference in first column ** Interatomic potentials used in Chapter 2 of this work				

Table 3.1. Basic properties of the six EAM potentials utilized in this study. Lattice constants and stacking fault energies were taken from the references for each potential, included in the first column. Melting temperatures and boundary energies were calculated using the methods of Wang et al. [31] and Tschopp et al. [12], respectively.

plane, L_x, determines the number of repeating units in faceted boundaries (also called the facet periodicity). The four Σ11 boundaries studied here have facet periodicities that vary significantly. For the minimum periodicity, which yields long repeating structures, 4 repeating units were used, and for the maximum, 12 repeating units were used. This yielded a range of L_x values between 16.7 nm and 25.0 nm. The minimum tilt-axis thickness, L_z, was fixed to be 7 repeats of the lattice parameter a_0, giving a range of 3.6 nm to 4.1 nm across the potentials. These size parameters, paired with the six separate EAM potentials, resulted in 24 bicrystals containing between ~150,000 to ~250,000 atoms.

All simulations were run using an NPT ensemble at three different T_H values of 0.8, 0.85, and 0.9, the same values and the same ensemble parameters used in Chapter 2.2. As before, temperature was regulated and a zero pressure was maintained using a Nosé-Hoover thermostat and barostat. Annealing runs were first initiated at half the target temperature by giving each atom a randomized velocity. The system was then allowed to ramp over approximately 20 ps to the target temperature, then held at this temperature for a further 100 ps to allow for relaxation of the

interfacial structure. At least 6 unique (in terms of initial randomized velocity) configurations were run for each temperature-potential-bicrystal combination.

As described in Chapter 2 (section 2), after relaxation, the energy-conserving orientational artificial driving force (ADF) [95] was used to drive boundary motion. To capture first and second nearest neighbors, a cutoff value of 1.1 a_0 was selected. The ADF was applied for a minimum of 120 ps and a maximum of 1 ns. Grain boundary velocities were measured by tracking the mean boundary position of each of the two boundaries separately and calculating the average displacement from their starting position. All simulations were run for at least 120 ps, which was adequate to obtain a steady-state velocity for the majority of bicrystals. Tracking was stopped either when the favored (growing) grain had consumed approximately 75% of the unfavored grain (to avoid boundary interactions) or when 1 ns had been reached, whichever came first. However, many boundaries in this data set are essentially immobile or begin moving only after a long lag time. To ensure a steady-state velocity for boundaries with significant lag times, collection of boundary statistics was begun only after the averaged boundary position had changed by an amount greater than twice the highest displacement recorded in the immobile phase, leading to values between 5–10 Å. Statistics for the boundaries that were relatively immobile were sampled from the final 100 ps of the simulation. Mobility was then calculated using Equation 1.1, $M = v/P$. Recall that v represents the boundary's velocity, P is the driving pressure experienced by the boundary (in this case, through the ADF), and M is the term that relates the two, with units of m/(GPa·s).

3.3 Results and Discussion

3.3.1 Trends in directionally-anisotropic mobility

Figure 3.1c-f shows the mean Y-direction displacement, $\Delta\bar{y}$, plotted against time to show the different migration patterns that are observed in this study. The top two plots feature boundary trajectories of Al-1 (Figure 3.1c) and Ni-2 (Figure 3.1d) at β = 25.5° and T_H = 0.85. The red and blue curves show the displacements for Type A and Type B migration, respectively. Though the Al-1 and Ni-2 faceted boundaries have macroscopically identical crystallography and the same simulation parameters, there are significant differences in their migration behaviors. For the Al-1 data in Figure 3.1c, the slopes of the red and blue curves are very similar to each other, indicating that Type A and Type B migration have similar velocities, and thus mobilities since the same driving force was used in each direction. By contrast, the slopes of the red and blue curves in the Σ11 Ni-2 data in Figure 3.1d are very different from each other. In this case, Type A migration proceeds at a much faster rate (2-3.3 times faster) than Type B migration.

In addition, there are differences between the materials in how migration begins. The longer immobile phase noted in the Cu boundary of Chapter 2, Figure 3.2. In the Al-1 example (Figure 3.1c), all boundaries moved a significant distance within a few picoseconds of application of the ADF. However, in the Ni-2 example (Figure 3.1d), there is a considerable delay between ADF application and the onset of motion, which can be quantified as a lag time, t_{lag}. It is especially apparent in the blue Type B trajectory lines but can also be observed to a more modest extent in the red Type A data as well. The simulation run with the longest lag time of approximately 35 ps (gray star) has been highlighted in orange after the boundary position has changed by approximately 5 Å. Figure 3.1e and f show two other common trends in lag time observed throughout the Cu and Ni dataset. Figure 3.1e shows a Cu-2 boundary at β = 35.3° and T_H = 0.8

with a lag time of 432 ps, which was typical for some inclination angles and lower temperatures. Several other boundaries appear to be either completely immobile or have lag times beyond the 1 ns run time limit, such as the example trajectory for Ni-1 at β = 35.3° in Figure 3.1f.

Figure 3.2 presents the mobility data for all materials, temperatures, and inclination angles used in this study, presented in three different columns. Each row represents one potential, with the stacking fault energy indicated underneath the potential label. Within each plot, the X-axis displays the inclination angle β in degrees and the three data sets in each plot corresponding to the three homologous temperatures that were tested (T_H = 0.8, 0.85, 0.9). The Y-axes of the left-most and center columns show the calculated mobility values for Type A and Type B migration (M_A and M_B), respectively. The right-most column contains the anisotropy ratio A from Equation 2.3, shown on a log scale. Error bars here and in all future plots show the standard deviation around the mean value. Figure 3.2 reveals that the anisotropic mobility seen in the Ni-2 boundary in Figure 3.1d is observed for many of the Cu and Ni boundaries. In fact, for Cu and Ni isotropic mobility is the exception, only observed in Cu-1 and Cu-2 at β = 15.8° for all three temperatures and at β = 46.7° for the highest temperature. In the majority of other angle-potential combinations of Cu and Ni, Type B mobility is considerably lower than Type A mobility. In the case of Ni-1 in Figure 3.2c, at T_H = 0.8 there are even multiple examples of very sluggish boundaries at β = 25.5° and 35.3°, leading to extreme anisotropy values of ~202 and ~50, respectively, which are outside the limits of the plot. In contrast, the two Al potentials have far lower anisotropy values overall, being close to 1 in most cases and never higher than 1.36.

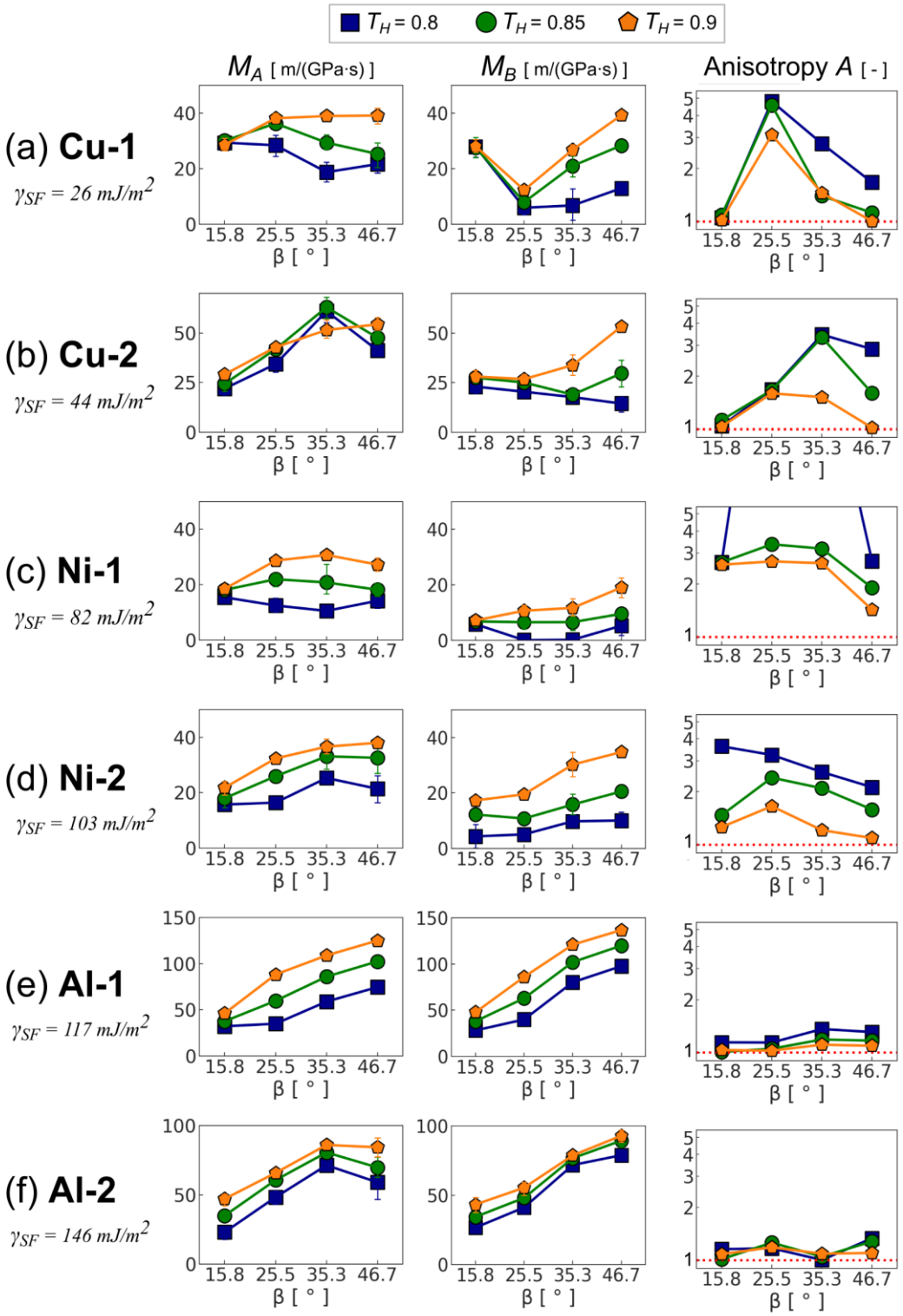

Figure 3.2. Type A mobility (leftmost column), Type B mobility (center column), and anisotropy ratios (represented by A, rightmost column) for each potential (rows), plotted against the inclination angle β (X-axis) and showing the data for three different homologous temperatures (different-colored curves).

Though a thorough investigation of the effect of temperature is outside the scope of this work, some general mobility trends and thus also anisotropy trends can be established with the three homologous temperatures studied. Increased temperature generally increases the mobility of both Type A and Type B-driven boundaries, suggesting that both migrate via thermally-activated mechanisms [1]. However, mobility increases more quickly in the Type B boundaries, meaning that anisotropy values generally decrease with increasing temperature, though commonly remain elevated even at the highest homologous temperature of 0.9 (orange curves). The most obvious exceptions to this trend are the β = 15.8° boundaries, where mobility is insensitive to temperature for both Cu potentials and the Ni-1 potential. With respect to the thermal dampening observed in Chapter 2 for the Cu-2 at β = 35.3° (Figure 3.2b, first column), where higher temperatures lead to lower boundary mobility for Type A motion, it can be seen here that it is a unique phenomenon in this dataset.

As mentioned earlier and shown in Figure 3.1b-f, almost all of the boundaries with elevated anisotropy values also had a significant phase of immobility in Type B migration before reaching a steady-state velocity. Figure 3.3 presents these Type B lag times, t_{lag}, as a function of inclination angle for the Cu and Ni boundaries, with the colors again indicating the different homologous temperatures. The lag times track fairly well qualitatively with the trends in anisotropy for each homologous temperature. The angles and temperatures with peak anisotropy values also tend to be those with the longest or near-longest lag times measured. Also of interest are temperatures and angles where, despite having low anisotropy values, the lag times are still elevated, for example at 46.7° in Cu-1. Relationships between lag times and boundary structure will be discussed in the following sections of this work.

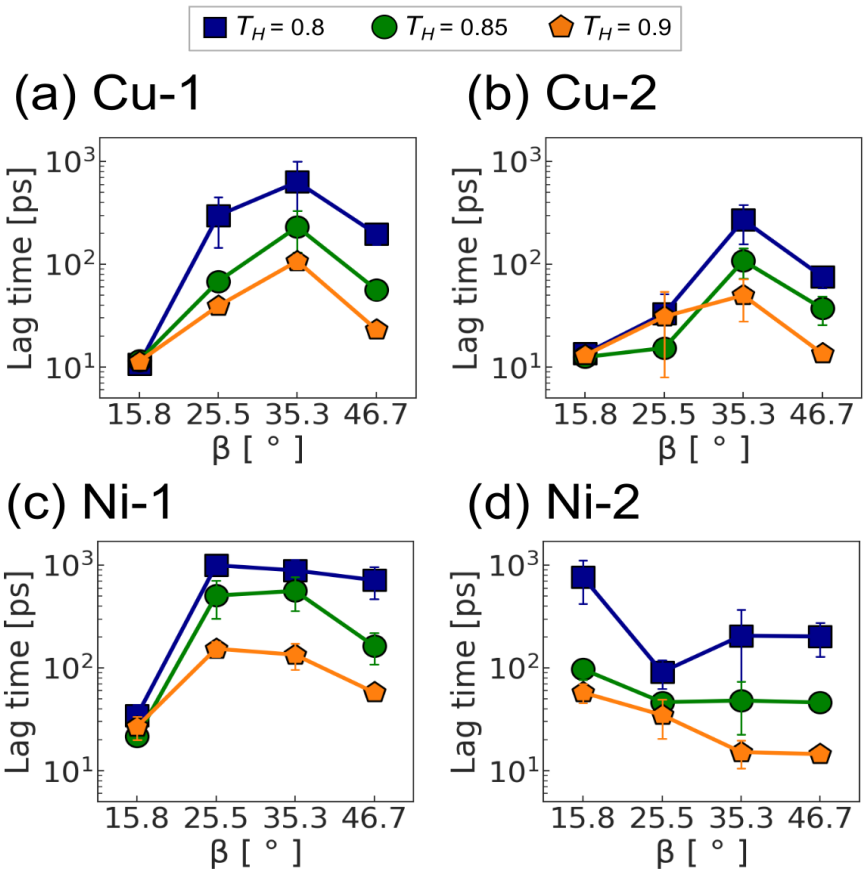

Figure 3.3. Lag times (t_{lag}) as a function of inclination angle β for Type B-migrating boundaries in (a, b) Cu and (c, d) Ni boundaries, for three different homologous temperatures.

As mentioned in the Methods section, and also conducted for the two boundaries of Chapter 2, an identical set of simulations were run on an asymmetric Σ5 tilt bicrystal (per element) in order to provide a control data set. Both the Σ5 and Σ11 boundaries are asymmetric, but the Σ5 lacks the ordered nature of facet planes and facet junctions. The results of these auxiliary simulations are not shown but gave anisotropy ranges between 1.00 and 1.09 for Σ5 boundaries over all homologous temperatures and across all potentials studied. Based on those results, a value of A = 1.1 (or a difference of 10% in mobility) was chosen to represent a boundary between directionally-anisotropic and isotropic mobility in the faceted Σ11 boundaries. By this standard,

it is clear that the great majority of Cu and Ni boundaries shown in Figure 3.2 can be categorized as strongly anisotropic.

3.3.2 Common structures of Σ11 boundaries

The 72 unique Σ11 bicrystals included in this dataset all share a small number of characteristic units that remain present both during annealing and migration, even at the highest homologous temperature of T_H = 0.9. These units agree well with structures defined in the structural unit model (SUM) [7], so we will utilize this formalism here as well. Because of the similarities between all boundaries, a small selection are used to introduce the entire set. Figure 3.4 shows two facet periods of as-annealed (T_H = 0.8) boundaries for two different materials at β = 25.5°. Starting with Al-2 in Figure 3.4a, the ascending segment is oriented along a plane which we have already seen in Figure 1a, the Σ11 symmetric boundary plane (SBP). As described in Chapter 2.3, and shown in Chapter 2.3, Figure 3.2, SBPs consist of a chain of diamond-shaped structural units called C units, which are denoted in this boundary the schematic on the right side of Figure 3.4a. The descending segment in Figure 3.4a also consists of the same pair of E structural units from the SUM. Recall that E units are comprised of 6 atomic columns enclosing a region of excess free volume in their centers, making them the largest structural unit that remains fully ordered [10, 88]. Though as noted, the E unit's kite-like shape can come in several variants, it becomes challenging to distinguish subtle variations in structure at high temperature during migration, especially across six different materials. Thus, we will, as in the earlier chapter, refer to all of them simply as E units. The schematic on the right side of Figure 3.4a shows the E units outlined in red. It is important to note that, especially given the wide variety of materials and boundary morphologies featured in this Chapter, the Adaptive Common Neighbor Analysis

algorithm in OVITO does not always identify all 6 atomic columns of the E unit as 'other' type (colored white in snapshots). As seen in the β = 35.3° boundary in Chapter 2.3, Figure 3.2d, a common occurrence in E units both during annealing and migration is the dissociation of one or more atomic columns. This process is shown again as a boundary snapshot in Figure 3.4a at the right-most bracket edge and in isometric view in Figure 4(c). Dissociated E units are indicated in schematics with dashed red lines in the former figure.

Figure 4b shows the crystallographically-identical boundary in a different material, Cu-2. Instead of two relatively simple ascending and descending boundary segments as seen in the Al-2 boundary of Figure 4a, there are 3 different segments in the Cu-2. The first of them is also an SBP facet, made of three C units instead of the five seen in the Al-2 boundary. The second feature is a terrace-like flat segment, which is once more the IBP facet of the Σ11 boundaries (which again, is oriented along the $(111)_A/(001)_B$ planes of each grain). The third feature which connects the IBP facets to the SBP facets are evidence of grain boundary stacking fault emission, just as was seen in the Cu boundary featured in Chapter 2.3, Figure 3.3. As shown in the isometric view of the boundary in Figure 3.4d, OVITO's dislocation analysis algorithm [109] identifies the ends of these defects as Shockley partial dislocations (vertical green line) with Burger's vectors of **b** = [-1 2 -1] (blue arrow, scaled up by 2.5). For both the Al-2 and Cu-2 boundaries, the fact that they share the C unit between them mean that they align well geometrically, something which is shown once more in Figure 3.4e and 4f. However, we stress here once more that this compatibility is also a function of direction lateral to the boundary. The transition from corner-sharing C units to face-sharing ones only works from the left-to-right direction (positive X-axis) due to the nature of the two planes involved.

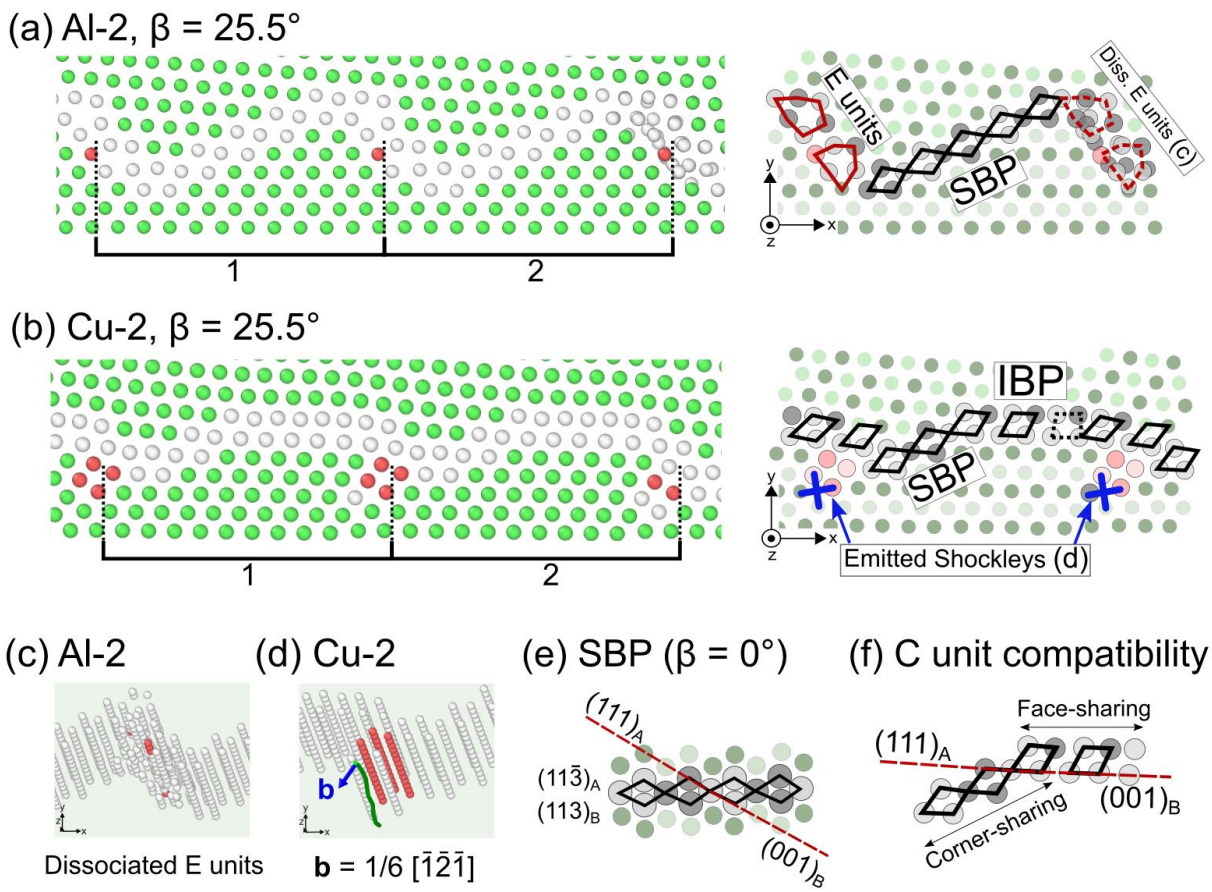

Figure 3.4. Representative structures for (a) an Al-2 boundary and (b) a Cu-2 boundary, each at β = 25.5° and T_H = 0.8. To the right of each are schematics showing the characteristic structural units for each boundary type. (a) The Al boundaries are made of pairs of E units (red) connected by a chain of corner-sharing C units (black). Atomic columns within E units can dissociate, as shown in the E units on the rightmost side of (a) and shown more in detail in the isometric view of (c). (b) In addition to SBP and IBP segments, Cu and Ni boundaries emit Shockley partial dislocations at facet nodes (blue X). An example of one in isometric view is shown in (d). Cu and Ni boundaries also generally have a higher fraction of IBP facet segment formation, which can also be described using C units in a face-sharing configuration as shown in (f).

In Chapter 2 it was demonstrated that the structures unique to Cu (here, Cu-2 at β = 35.3°) were also responsible for directionally-anisotropic mobility. Expanding the range of materials and inclination angles studied makes possible an analysis of the trends in stacking fault energy, and their relationship to the anisotropy ratio *A*. The plot in Figure 3.5 illustrates these relationships between anisotropy (Y-axis), material and stacking fault energy (X-axis), and inclination angle (symbols/colors) for T_H = 0.8. Potentials are placed in order of increasing

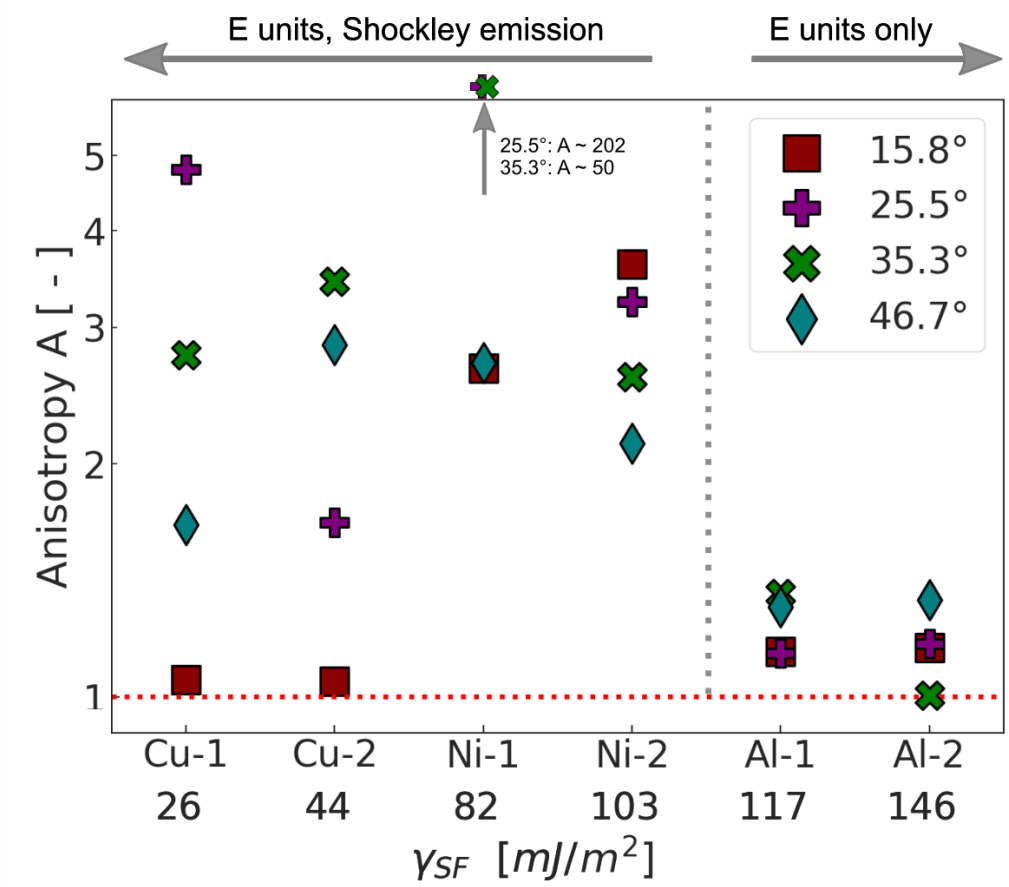

Figure 3.5. Anisotropy ratio values for T_H = 0.8 for different materials/potentials, placed in order of increasing stacking fault energy and with the inclination angle shown by the data symbols. The Cu and Ni potentials on the left side have low enough stacking fault energies to be able to emit Shockley partials at facet nodes and have higher overall anisotropies than the two Al potentials, which only have E units at facet nodes. The exceptionally high anisotropy values for β = 25.5° and 35.3° for Ni-1 lie out of the bounds of the Y-axis.

stacking fault energy. The two Ni-1 markers which are off the chart are a reminder of the two very high anisotropy values for β = 25.5° and 35.3° that exist outside the Y-axis limits (at ~202 and ~50, respectively). The highest values of anisotropy exist on the left side of the plot in the Cu and Ni materials, while only very low anisotropy is found for the two Al potentials on the right side (separated by a dotted grey line). This separation clearly corresponds to the main structural difference between the anisotropic boundaries and the reasonably isotropic Al boundaries, namely stacking fault emission at facet nodes. Beyond this critical difference, the relationship between

anisotropy and stacking fault energy does not appear to be straightforward. For example, the Ni potentials, which both have higher stacking fault energies than Cu, have consistently higher anisotropy values on average. There also do not appear to be any clear relationships between inclination angle and anisotropy. While only $T_H = 0.8$ is shown in Figure 3.5, the same conclusions are drawn from the anisotropy data for the other temperatures. This suggests that stacking fault energy may only contribute to anisotropy in allowing phenomena such as grain boundary stacking fault emission to take place. The magnitude of anisotropy likely depends on other geometric or material-dependent parameters that come into play during boundary migration, rather than the static structures of the interfaces by themselves.

3.3.3 Shuffling modes and directionally-anisotropic mobility

The results from Chapter 2 on the Cu and Al boundaries (equivalent to Cu-2 and Al-2, both at $\beta = 35.3°$ in this chapter) revealed that facet migration mechanisms could be sorted into three distinct categories, which we termed shuffling modes. Recall that this term referred three different types of motion mechanisms found in the Al and Cu boundaries: disordered shuffling, Shockley shuffling, and slip plane shuffling. Observation of the migrating $\Sigma 11$ boundaries for the remaining material-angle combinations reveals that, in general, the same three shuffling modes can be clearly identified in the larger dataset as well. As before, the only mode active in the Al-1 and Al-2 boundaries is disordered shuffling, while all three can be active in the found Cu and Ni materials. An example of this is shown in Figure 3.6a, which is a snapshot of a Cu-1, $\beta = 35.3°$ boundary undergoing Type B (slower) motion at $T_H = 0.85$. Facet nodes are indicated once more by dotted lines at the ends of brackets. E units have been outlined as earlier in red lines (with dashed red lines for dissociated E units) and emitted Shockley partials have been marked with a blue X.

Unlike the as-annealed facet node structures seen in the Cu-2 boundary of Figure 3.3, this snapshot demonstrates that the E unit node, the dissociated E unit (leftmost junction), and the emitted Shockley node can be present simultaneously in migrating boundaries.

We review in this section once more the major features of each of the three shuffling modes, beginning with disordered shuffling in Figure 3.6b. The initial dissociation of one E unit at 0 ps leads to a cascade of dissociations throughout the rest of the facet node over the following few ps, forming a cluster of disordered atoms. Observing the progression of the migrating Cu-1 cluster shown in the snapshots of Figure 3.6b shows how it shifts approximately three $(1\text{-}1\text{-}1)_A$ planes to the right over the course of 5 ps, with the black bar indicating the original position of the facet node. Once formed, these disordered clusters can exist for varying amounts of time before re-associating into E units. From that point, those E units in Cu and Ni may migrate either via Shockley shuffling (which can in turn result in slip plane shuffling during Type A migration, if circumstances favor it) or dissociate once more and begin a new phase of disordered shuffling. Disordered shuffling is the only mode available to facet nodes in Al boundaries in either direction.

Though disordered shuffling can be observed in all three materials, the two remaining ones occur only in the Cu and Ni boundaries due to their lower stacking fault energies. Shockley shuffling, which occurs in both motion directions, is shown in Figure 3.6e. As described in Chapter 2, and restated here, this mode begins when the top-most E unit at a node releases a Shockley partial dislocation (Figure 3.6e, 5 ps). Returning the emitted Shockley to the node, also called Shockley contraction, leads to the formation of a new pair of E units one $(1\text{-}1\text{-}1)_B$ plane (the Shockley partial emission plane, parallel to the grey reference line) to the left of the previous E unit. The third mode, slip plane shuffling, occurs almost exclusively during Type A motion. An example is shown in Figure 3.6d for a Cu-2 boundary ($\beta = 35.3°$ at $T_H = 0.8$). If a Shockley partial

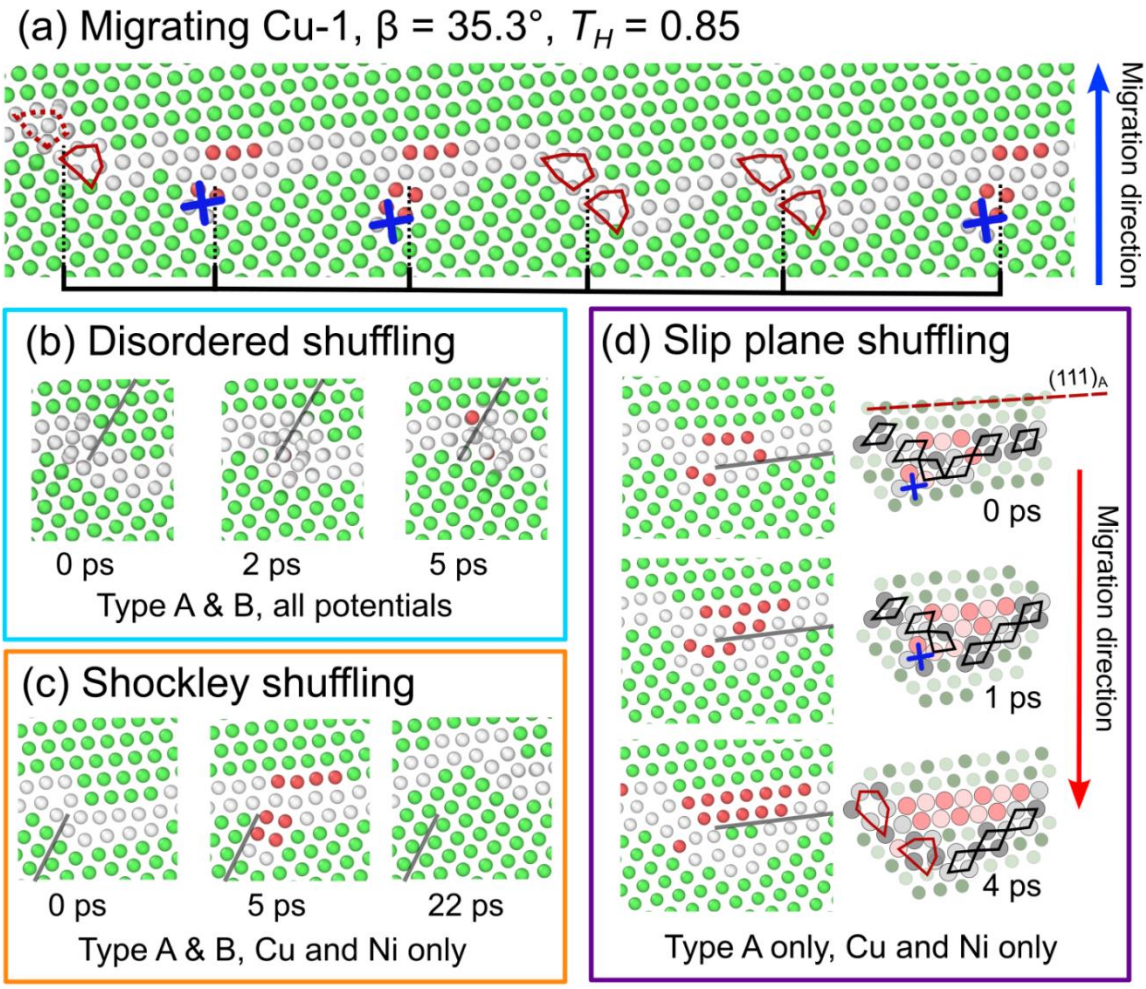

Figure 3.6. (a) Snapshot of a Cu-1 boundary during Type-B migration at T_H = 0.85 containing the three different facet node types: E units (red outlines), dissociated E units (dashed red outline on left-most node), and emitted Shockley dislocations (blue X). (b) An example of disordered shuffling beginning at an E unit after an atomic column dissociation. (c) An example of Shockley shuffling. Note the delay between Shockley emission at 5 ps and Shockley contraction, 17 ps later at 22 ps. (d) An example of slip plane shuffling, in which an IBP facet transforms into an SBP facet. In certain boundaries, a stacking fault (red atoms) in Grain A can also form between two facet nodes. This mode is only possible during Type A motion in Cu and Ni boundaries.

has been emitted at a node and that node has an IBP facet to its right side as is the case in the second facet node of Figure 3.6a, the facet itself can migrate without requiring Shockley partial contraction to occur beforehand. This migration is accomplished by unfolding its C units from a face-sharing configuration into the corner-sharing one of the SBP in the manner shown from 0 ps to 4 ps in Figure 3.6d. Essential for this process is the presence of the $(111)_A$ slip plane parallel to

the boundary, which is part of why the transition from face-sharing to corner-sharing C unit is relatively easy to accomplish.

In the previous chapter, we were able to establish that directionally-anisotropic mobility is a direct result of slip plane shuffling being available only during Type A migration. This is because slip plane shuffling allows the affected node to lower the activation energy for subsequent step migration through Shockley partial contraction. The observation of the extended dataset allows us to confirm that slip plane shuffling is responsible for directionally-anisotropic mobility as it was in the single Cu-2 boundary of Chapter 2, also giving an opportunity to explore this transformation in more detail. Figure 3.7 shows a facet node transformation taking place in the two different migration directions for an anisotropic Ni-1 β = 15.8° boundary. The three snapshots in Figure 3.7a show the transformation for a node undergoing Type A migration, while the bottom three in Figure 3.7b show it for Type B. The colored arrows between snapshots indicate the direction of migration while the dotted gray lines are fiducial markers denoting the starting positions of the nodes. The initial state at 0 ps of the facet nodes in the first panels of Figures 2.7a and b are virtually identical, with IBP facets and emitted Shockley partials. The final states at 2 ps in the third panels are also extremely similar, with both junctions having transformed into a pair of E units. However, looking at the transition states at 1 ps shows that Shockley partial contraction is occurring at different times in each transformation and thus under different conditions. With pure Shockley shuffling shown in 7(b), the contraction takes place in the first half of the transformation. Note that, though only Type B migration is shown here, the same transformation can occur through pure Shockley shuffling (i.e., without slip plane shuffling) during Type A migration as well, but in the reverse order. In contrast, during slip plane shuffling, Shockley contraction takes place in the

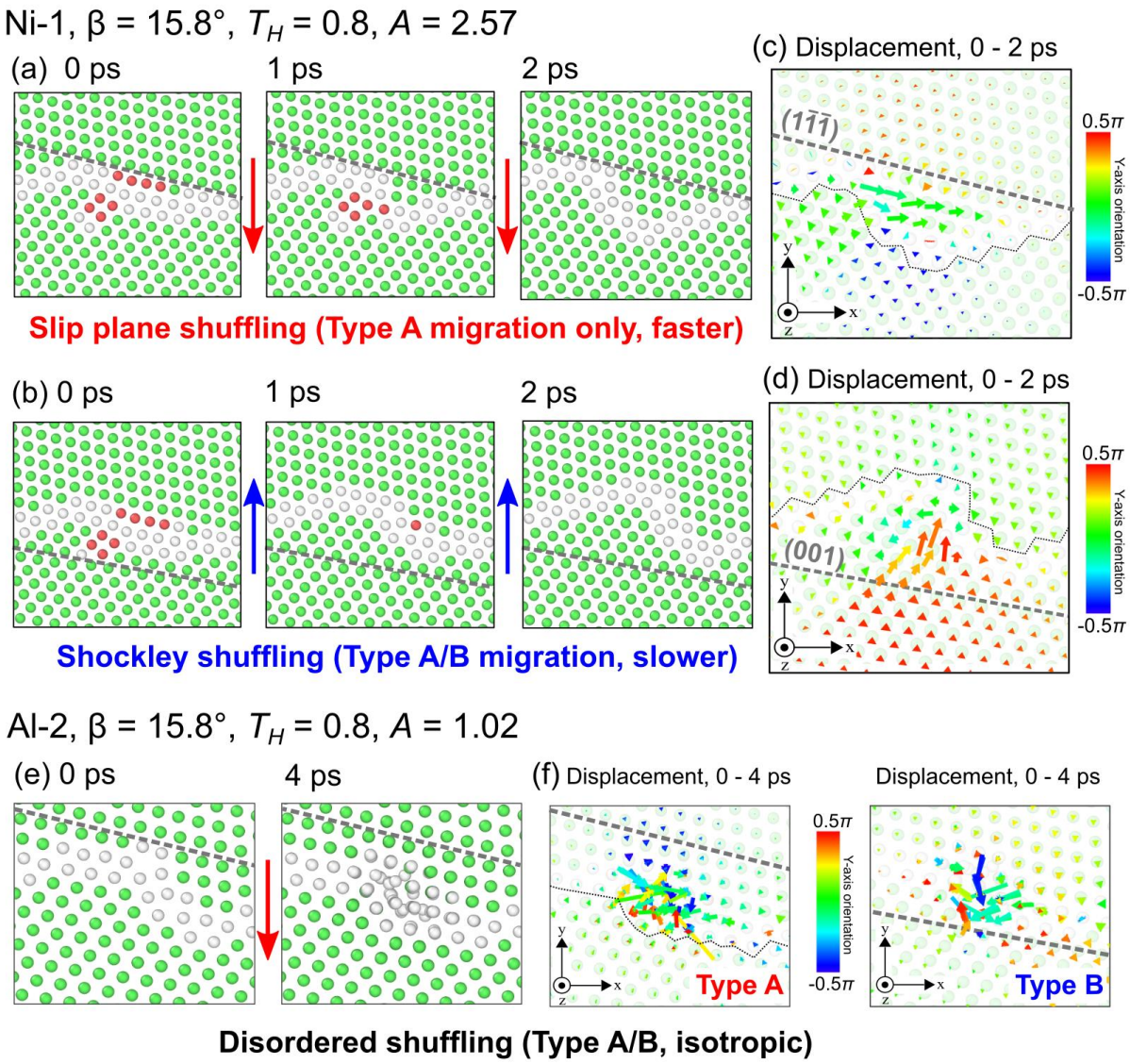

Figure 3.7. (a, b) Comparison of a node transformation that starts and ends in the same form in (a) Type A and (b) Type B migration but have different intermediate stages and (c, d) displacement histories. Shockley partial contraction also occurs at different times in each transformation. € Illustration of disordered shuffling during Type A motion. Its displacement map in € closely resembles that of a similar 4 ps displacement in Type B. All displacement vectors have been scaled by 2.5 for visualization and are colored by their orientation relative to the Y-axis.

second half of the transformation, after the process of C unit unfolding has already begun transforming the neighboring IBP facet into an SBP facet.

The significance of this asymmetry in the timing of Shockley partial contraction becomes clear when observing the initial portion of Cu and Ni simulations, where the as-annealed boundaries have primarily emitted Shockley partials and IBP facets are present at almost every facet node. Recall that most Type B-migrating boundaries have extended immobile phases like those shown in Figure 3.1(d-f) and Figure 3.3. Recall in Chapter 2.3.5, we explored the implications of the results of a hybrid experimental and computational study by Bowers et al. [23]. In their work, Bowers et al. found that defects very similar to E units in Au strongly suggested that Shockley partial contraction is a thermally-activated process. Thus, all facet nodes in the initial structure of a Cu or Ni boundary will be pinned until the activation energy barrier for contraction is overcome. In contrast, the identical as-annealed boundary can immediately begin structural transformations with a Type A driving force, since it will initiate migration in IBP facets before requiring facet nodes to unpin. The final Shockley contraction is then easier to accomplish because the majority of local structural transformation (the creation of a new segment of SBP facet) has already occurred.

To illustrate this process in greater detail than shown in Chapter 2, displacement maps based on the starting and ending positions of each transformation are shown in Figure 3.7e for slip plane shuffling and Figure 3.7d for Shockley shuffling. Displacement vectors are colored by their angle relative to the Y-axis, with red and blue indicating motion in the positive and negative Y-directions, respectively, and green arrows indicating motion along the X-axis. The vectors have also been scaled by a factor of 2.5 to enhance visualization. For slip plane shuffling in Figure 3.7d, the largest displacement vectors are those directed along the IBP facet, which is not only already

in Grain A but is also oriented along the $(1\text{-}1\text{-}1)_A$ slip plane. Figure 3.7d shows how this process is quite different in Shockley shuffling. The contraction must both immediately transform a region of Grain A and also acts perpendicular to the same $(1\text{-}1\text{-}1)_A$ slip plane (red arrows) that enable slip plane shuffling. Though the impact of these differences in timing and displacement are most obvious at the start of a simulation, where most Type A facet nodes move due to slip plane shuffling, the same process is also occurring at different points during Type A migration when IBP facets are present near facet nodes. The cumulative effect of this is manifested in the generally faster migration velocities seen in Type A moving boundaries in Cu and Ni.

Comparing the displacement maps of Shockley and slip plane shuffling to those illustrating disordered shuffling offers an explanation as to how directionally-anisotropic mobility is avoided in Al. Figure 3.7e shows a facet node moving via disordered shuffling in the Type A direction (red arrow between images) over the course of 4 ps, with the associated displacement map shown in Figure 3.7f. The second displacement map in Figure 3.7f was created using a very similar disordered shuffling event occurring over 4 ps, but in the Type B direction. The two disordered shuffling displacement maps in this figure are notably different to those showing slip plane and Shockley shuffling. Atomic column dissociation means that individual atoms can move and hop relatively easily within the free volume of E units, leading to crossing of displacement vectors in the map and a clustered appearance, demonstrating that shuffling is highly localized to the area immediately within the free volume of the E units in the facet node. By contrast, slip plane and Shockley shuffling involve shifts of entire atomic columns not only in the grain boundary itself, but also in the neighboring bulk crystals, requiring a larger degree of coordinated motion. Shifts involving atomic columns are restricted by the characteristics of local crystallographic planes, while atomic column dissociation releases the disordered nodes from those restrictions.

Disordered shuffling can thus explain in large part why the Al boundaries generally migrate isotropically and offers a potential means of explaining the differing magnitudes of anisotropy observed in the Cu and Ni boundaries of Figure 3.5.

3.3.4 Connections between directionally-anisotropic mobility and disordered shuffling

The preceding sections expanded and confirmed the results from Chapter 2, which showed that that directionally-anisotropic mobility in Cu and Ni is a result of having a directionally-dependent shuffling mode (slip plane shuffling) that allows facet nodes to bypass Shockley partial contraction when migrating in one direction. This also allows Type A migrating facet nodes to shift more quickly between different shuffling modes, which includes disordered shuffling. Since Type B nodes are pinned by emitted Shockley partials for longer times, they are likely to have comparatively fewer E unit dissociation events and thus fewer occurrences of disordered shuffling per node. There is also a noted decrease in anisotropy and lag times with increasing temperature in the Cu and Ni boundaries (Figures 2.2 and 2.3), which we hypothesize is correlated with disordered shuffling becoming the dominant mode for both Type A and B motion at the highest homologous temperatures. Based on this reasoning, we propose that tracking the frequency of E unit dissociation and formation of disordered clusters occurring during migration can provide a means of quantifying how shifts in shuffling mode modulate directionally-anisotropic mobility in the Cu and Ni bicrystals.

To quantify the amount of disordered shuffling occurring per facet node during migration, an algorithm that tracks facet node dissociation events was developed. A representative example of the process for a Ni-1, 35.3° boundary during Type A motion is shown in Figure 3.8. First, the potential energy distribution of the grain boundary atoms is collected (Figure 3.8a). It was

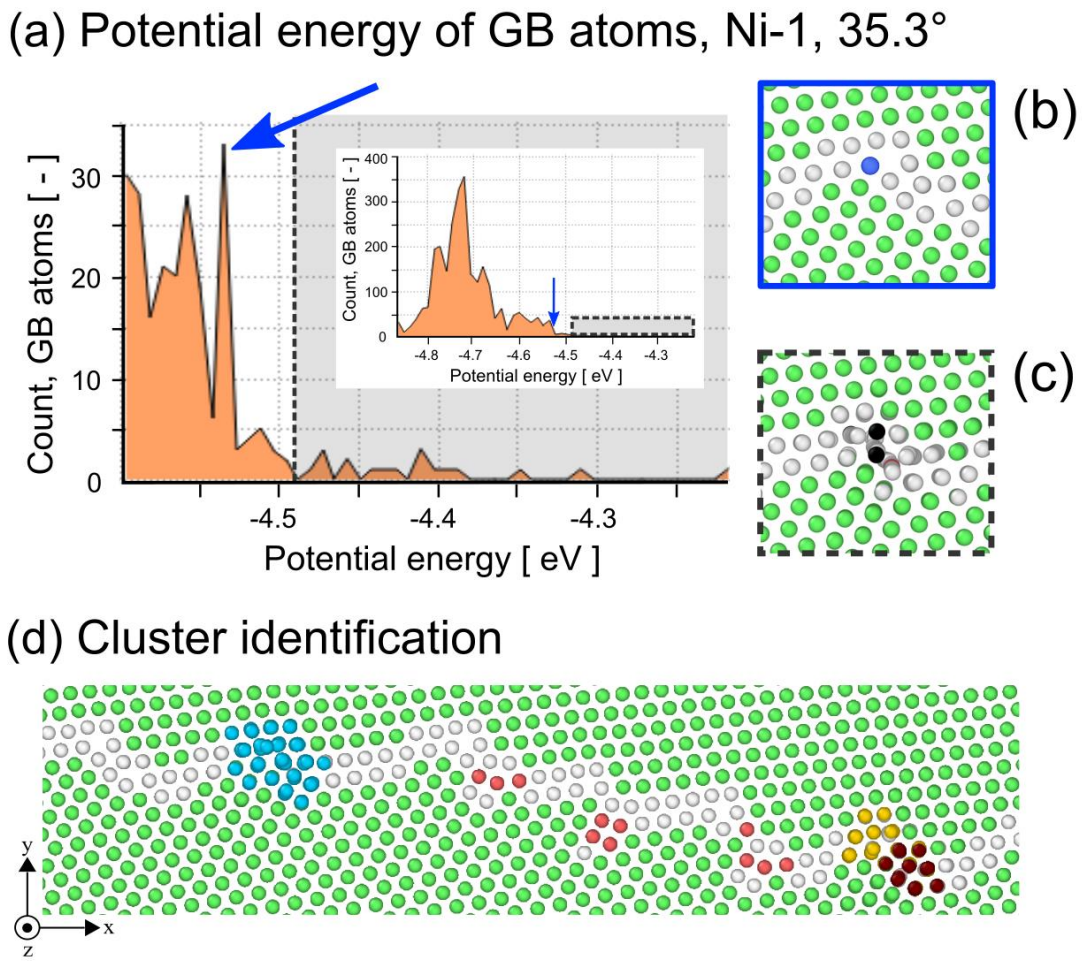

Figure 3.8. Overview of the disordered cluster identification algorithm used to track trends in disordered shuffling through all boundaries. (a) Example histogram showing the distribution of potential energies of a migrating Ni-1 boundary. The spike indicated by the blue arrow corresponds to the highest-energy fully intact atomic column in E units, shown in (b) as a blue atom. Atoms with higher potential energies above this spike tend to be involved in disordered shuffling events, which form clusters at facet nodes. (d) Final result of the cluster identification process for a particular boundary.

observed that, for each material, there is a particular atomic column within E units that has high potential energy but remains completely ordered. This atomic column for Ni-1 is shown in Figure 3.8b colored in blue, with an energy of approximately -4.58 eV (shown with a blue arrow in Figure 3.8a). Atoms with potential energies above this value tend to be involved in atomic column dissociation, shown in the grey shaded region in Figure 3.8a. An example of a node with

dissociation and selected high-energy atoms (black) is shown in Figure 3.8c. In order to confine tracking only to completely disassociated atomic columns, atoms that are +0.1 eV higher than the intact atomic column are selected, which generally excluded partially-dissociated columns and shifts the focus to single high-energy/disordered atoms in the long tail of the potential energy distribution. Because dissociation events involve groups of atoms, the high-energy atoms may be spatially correlated and lead to an over- or under-counting of facet node clustering. To account for this, the Cluster Analysis algorithm in OVITO [116] is applied with a $1.1a_0$ cutoff to consolidate the spatial information. An example snapshot is shown in Figure 3.8d, which identifies three separate clusters at two different nodes. From this analysis one may gain measure of the number of dissociation events occurring per timestep.

Results from this analysis for three example boundaries are shown in the plots of Figure 3.9a-c, which each show the count of disordered clusters per node as a function of homologous temperature. As in earlier figures, the red data points show the counts for Type A motion and the blue curves those of Type B. The insets show each boundary's anisotropy ratio plots from Figure 3.2, with the data for the relevant inclination angle outlined in blue and highlighted. From Figures 2.9a and b, it is clear that Type A migration has a consistently higher cluster count than Type B for all homologous temperatures. This data supports our hypothesis that there are directionally-dependent differences in the occurrence of E unit dissociation events, implying that disordered shuffling is occurring at a higher frequency in Type A migration. For both curves, increasing temperature leads to an increase in the counted clusters per node, which is also consistent with an increased rate of disordered shuffling for both motion directions. As mentioned earlier, Shockley partial contraction is a thermally-activated process and there is also a corresponding decrease in the Type B lag times shown in Figure 3.3. Most notably, there is a far more dramatic increase in

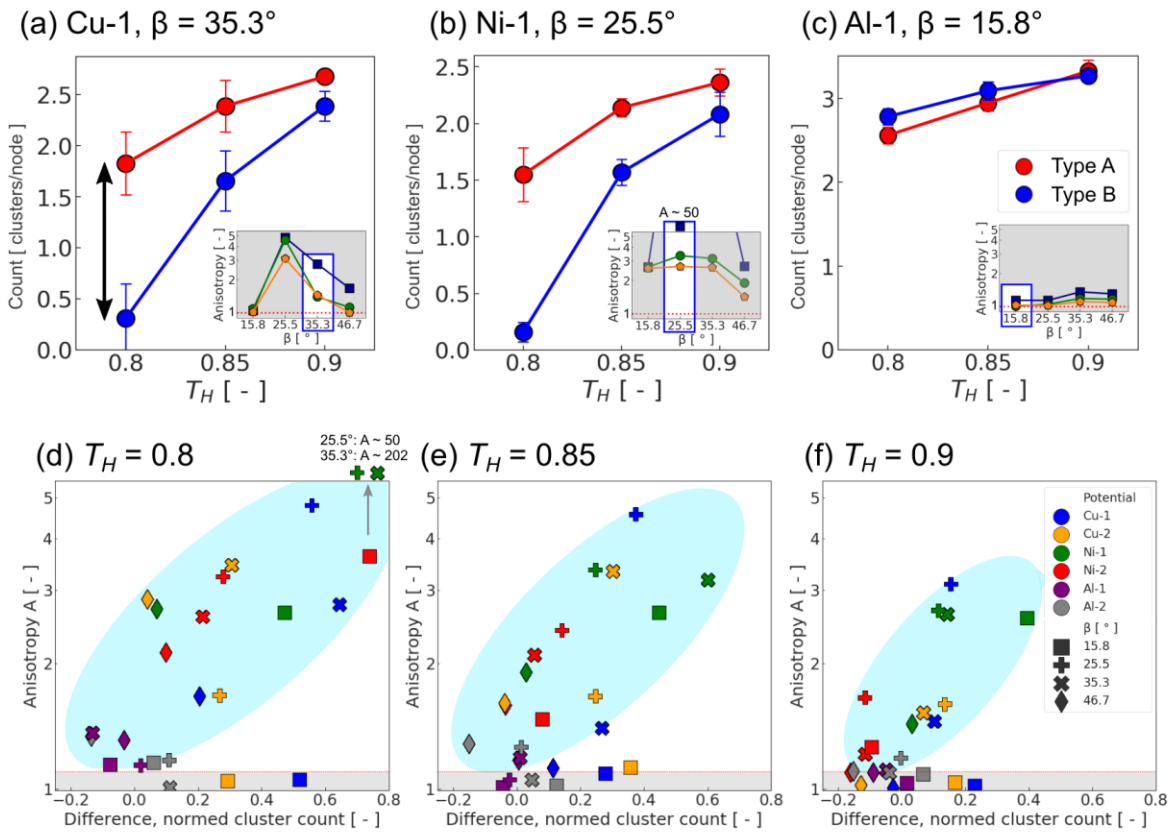

Figure 3.9. Normed disordered cluster counts for Type A (red) and Type B (blue) migration versus homologous temperature in example boundaries from (a) Cu, (b) Ni, and (c) Al. The average cluster counts exhibit a systematic difference between Type A and Type B (black arrow in (a) at T_H = 0.8) which decreases with increasing temperature. The inset shows the anisotropy mobility data for the chosen inclination angle angle (highlighted), showing a corresponding drop in anisotropy at T_H = 0.85 and 0.9. (d-f) Anisotropy versus the normed cluster count differences for each material and inclination angle. Blue regions are provided as a visual aid, enveloping boundaries with significant anisotropy values. The grey region in the bottom contains boundaries with little to no anisotropy (A < 1.1).

cluster counts for Type B migration than Type A, which leads to a decrease in the difference between the cluster counts for the two types of motion (black arrow in Figure 3.9a). The decrease in this difference corresponds to large reductions in the anisotropy ratios for both the Cu-1 and Ni-1 boundaries. In contrast, the Al-1 boundary in Figure 3.9c has little to no difference in its Type A and B disordered cluster counts and, therefore, little to no anisotropy. These trends suggest that the cluster count per node may provide a means of connecting the anisotropy ratio directly to

changes in boundary structure, namely the relative frequencies of Type A and Type B disordered shuffling.

Figures 3.9d-f show the anisotropy plotted against the normalized disordered cluster count differences for each of the three homologous temperatures studied. In order to more clearly compare the difference in cluster counts across all 6 potentials and 4 inclination angles, the cluster counts were normalized against the maximum count for each combination of material, inclination angle, and temperature, yielding values between 0 and 1. Different colored data points indicate the different potentials, while inclination angles are shown using different symbol shapes. The two markers above the Y-axis limits in Figure 3.9d indicate the cluster size differences of the Ni-1 boundaries at 25.5° and 35.3° with anisotropy values of ~ 202 and ~50, respectively. The data indicate that there is a general, temperature-dependent positive correlation between the anisotropy ratio and the Type A/B cluster count differences. This relationship is marked by a light blue oval in each plot, which we note begins above the anisotropy threshold of 1.1 (grey box). As temperature is increased from Figure 3.9d through f, the light blue oval maintains its orientation, but becomes smaller and shorter. This also demonstrates that the cluster count differences are decreasing as the magnitude of anisotropy decreases. We thus conclude that temperature has the overall effect of increasing disordered shuffling at facet nodes, resulting in the corresponding reduction in anisotropy magnitudes.

3.4 Conclusions

The goal of this chapter was to investigate whether the shuffling modes and subsequent directionally-anisotropic mobility in faceted Σ11 <110> tilt grain boundaries, discovered in Chapter 2, is a general property of this boundary type. To accomplish this goal, the initial

migration behavior in a large set of in three different face-centered cubic metals was investigated using a series of molecular dynamics simulations probing different potentials, temperatures, and inclination angles. From these results, the following conclusions can be made:

- Directionally-anisotropic mobility is discovered to not only exist in the Cu boundary of Chapter 2, but also in a variety of different faceted asymmetric Σ11 <110> tilt boundaries in Cu and Ni. Boundaries with this anisotropy also exhibit a lag time before beginning motion, with some Ni boundaries barely moving within 1 ns. Boundaries were found to move up to 5 times faster in one direction than the other in many cases, with a few selected outliers showing high anisotropy ratios.
- Across 6 different materials/potentials, including the two boundaries from Chapter 2, the same two structural units could be consistently identified: C units and E units. The atomic columns in E units can dissociate, forming clusters of disordered atoms at facet nodes. Due to the lower stacking fault energy in Cu and Ni boundaries, E units can also emit Shockley partials, which form E units once more when contracted.
- The results of this chapter allow us to confirm that a low stacking fault energy material is necessary for directionally-anisotropic mobility to occur in these boundaries. In this case, the subjective classification for a "low" stacking fault energy means that a boundary must be able to emit grain boundary stacking faults, which excludes Al. Beyond this cutoff, the relationship between the magnitudes of stacking fault energy and anisotropy is unclear.
- Migration of the faceted boundaries is accomplished through the same three shuffling modes as identified in Chapter 2: disordered shuffling, Shockley shuffling, and slip plane shuffling.

- Disordered shuffling is the only mode which is, in general, directionally-isotropic with respect to mobility. The atoms involved in cluster motion have three degrees of translational motion and their displacements are localized to free volume within facet nodes. In contrast, Shockley shuffling and slip plane shuffling are both dependent on coordinated shifts of coherent atomic columns and thus necessarily involve local planes, which constrain motion in specific ways.
- In Cu and Ni, the rate-limiting mechanism of migration is Shockley partial contraction at facet nodes. If contraction can occur at a higher rate, the rate of node migration is increased. Factors that can increase contraction include increased temperatures (which increases the rate of isotropic disordered shuffling) and slip plane shuffling (which creates more favorable structural conditions for Shockley contraction). Directionally-anisotropic mobility in Cu and Ni can be primarily attributed to the increased node migration rate made possible in Type A motion by the slip plane shuffling mode.

The property of grain boundary mobility is commonly understood through the lens of bicrystallography (the five macroscopic degrees of freedom), which has proven to be an incredibly useful framework to date. However, the divergent mobilities seen in these faceted Σ11 boundaries show that this description is likely not yet sufficient. Though directionally-anisotropic mobility is a phenomenon made possible by the crystallographic properties of the Σ11 misorientation, it is the complex interactions between those properties and the microscopic boundary structure, determined by energetic phenomena such as temperature and stacking fault energy, that ultimately give rise to it. There may be a wide range of yet undiscovered mobility phenomena that similarly arise from unique faceted boundary morphology.

4 Alloying induces directionally-dependent mobility and alters migration mechanisms of faceted grain boundaries

4.1 Introduction

In Chapter 2, the atomistic motion mechanisms of faceted Σ11 boundaries were characterized (shuffling modes) and the phenomenon of directionally-anisotropic mobility was discovered in a single faceted Σ11 boundary in Cu. Chapter 3 expanded on this work, demonstrating that shuffling modes operate in a variety of face-centered cubic materials (Al, Cu, and Ni), and established that directionally-anisotropic mobility is a general property of boundaries in Cu and Ni. As those chapters focused on pure systems, a natural next step is to explore how the addition of solute atoms might affect faceted Σ11 boundary migration.

As a starting point, we choose the β = 15.8° boundary using a Cu-Ag potential developed by Williams et al. [117]. The Cu-Ag binary system is chosen for its positive enthalpy of mixing and for its body of interesting hybrid experimental/computational literature describing complexion transitions, amongst them faceting [41, 55, 118, 119]. The motivation behind the choice of the β = 15.8° boundary is twofold. First, as the smallest inclination angle, it also has the longest facet period of all boundaries studied up to this point. Longer facet periods mean an increase in the lengths both the SBP and IBP facets, making the effects of segregation clearer to observe per facet. Second, though directionally-anisotropic mobility could be predicted for this boundary by the criteria established in Chapter 3, its anisotropy ratios in both Cu and Ni lay solidly at or below the threshold for directionally-anisotropic mobility (Figure 3.9d-f) for unknown reasons.

Through this combination of boundary and material, we first explore the nature of Ag segregation through a range of temperatures and compositions. We then select a temperature-

solute concentration combination that is favorable to migration in order to explore the effect that solute atoms have on shuffling modes.

4.2 Materials and Methods

The simulation parameters used to create the bicrystals in this setup have been defined in detail in Chapter 2.2. All generated bicrystals have dimensions of 180 x 381 x 36.5 Å (X, Y, Z respectively) and ~200,000 atoms. As in previous chapters, the bicrystals are relaxed via an annealing process after creation. A random velocity is assigned to atoms to initialize temperature and the cell is then ramped to the target temperature over approximately 20 ps, to be annealed for a further 100 ps. An EAM potential corresponding to the Cu-Ag [117] system was selected for its positive enthalpy of grain boundary segregation [120] and also because this potential's phase diagram indicates that Ag is in solid solution at the higher temperatures necessary for faceted Σ11 boundary migration. Initial testing confirmed that its pure Cu variant facets very similarly to these boundaries in pure Cu potentials [78, 121]. Two periodically-repeating units of the faceted Σ11 boundary studied here, with a boundary plane inclination angle, β, at 15.8°, are shown in Figure 4.1a. The ascending plane (left-to-right in the positive X-direction) is a facet oriented along the SBP of Σ11, with an accompanying schematic overlay onto one facet period in Figure 4.1b, and the IBP facet makes up the descending plane following it.

To dope the pure Cu bicrystal with Ag, a hybrid Monte Carlo (MC)/MD algorithm was used (see Chapter 1.4.2 for a general overview of this algorithm). Before doping, fully-minimized pure samples were annealed as described above. Configurations of Ag atoms corresponding to the target concentration were then sampled by performing 1 MC step for every 100 MD steps. MC steps were conducted using a variance-constrained semi-grand canonical ensemble [122]. The 20

ps-averaged change in the absolute value of the potential energy gradient was monitored until it reached a value less than 0.1 eV/ps, then run for 1 ns longer to generate different (but energetically equivalent) configurations of the doped bicrystals.

Mobility studies were performed as in previous chapters using the ECO artificial driving force (ADF) code [95], described in Chapter 1.3.1 as well as Chapter 2.2. The growth of Grain A at the expense of Grain B (boundary motion in the negative Y-direction in all snapshots) is once more referred to as Type A migration, and its opposite is Type B migration. For each configuration, 10 unique simulations were run for at least 150 ps using a ΔE value of 25 meV/atom. Doped samples used identical starting configurations, but unique velocity seeds, for Type A/B motion to understand the influence of solutes on directional migration. Because some boundaries exhibited an initial lag time before migrating (especially Type B), all measurements were taken after boundaries had moved at least 3 Å, which is then chosen to represent t = 0 ps. Boundary motion was tracked by first lightly minimizing the bicrystal to remove thermal noise, then locating the mean position of non-crystalline (i.e. grain boundary) atoms.

4.3 Results and Discussion

4.3.1 Structure and properties

The IBP facets have several interesting characteristics that make them suitable segregation sites. For example, have a significant amount of excess free volume compared to the SBP facets, due to the presence of the {001} plane, as can be seen when looking at the mean Voronoi volume (averaged at each X-position) in Figure 4.1c (including FCC atoms). The exploration of free volume in this chapter allows a fresh view of the phenomenon of grain boundary stacking fault emission seen in Chapters 2 and 3. The nature of the Shockley partial dislocations can be observed

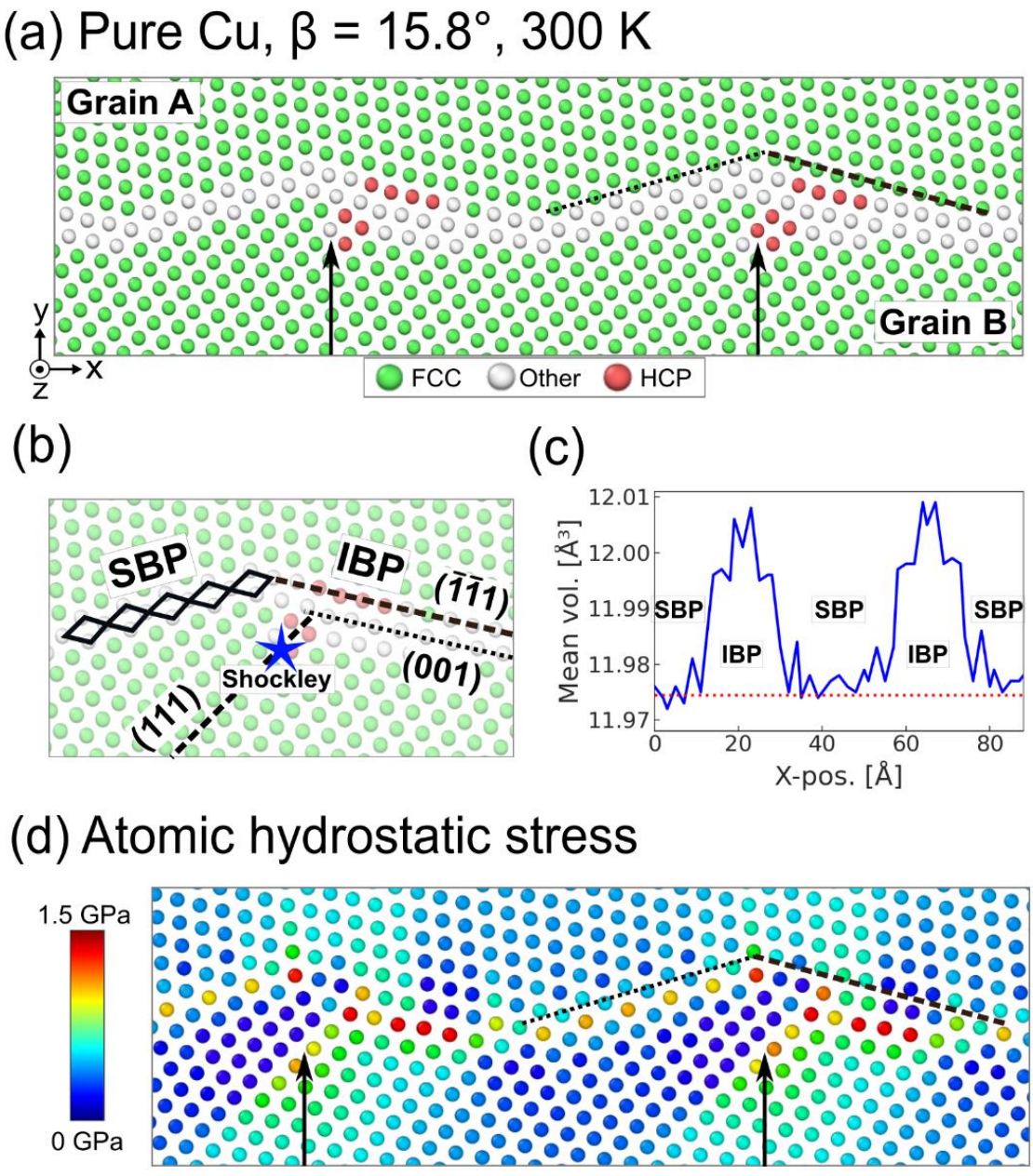

Figure 4.43. (a) The faceted Σ11 boundary in pure Cu at 300 K, where the black arrows indicate the facet nodes. The ascending dotted line shows the facet oriented along the symmetric boundary plane (SBP), and the descending dashed line the faceted oriented along the $\{111\}_A/\{001\}_B$ incommensurate boundary plane (IBP). (b) Schematic overlay showing important structural features of one facet period. The nodes coincide with Shockley partials emitted from the boundary. (c) The mean Voronoi volume as a function of X-position, showing the different volume contributions of each facet. The red dotted line indicates the mean for FCC atoms alone (11.975 $Å^3$). (d) The atomic hydrostatic stress, showing that the IBP facet has the highest tensile stresses (red), and the emitted stacking fault at the node contains the largest stress discontinuity (lacking a smooth gradient in color), characteristic of dislocation cores. The legend has been truncated to increase contrast.

in the hydrostatic stress field in Figure 4.1d, which shows a tension-compression discontinuity (lighter colors to dark blue, respectively) characteristic of dislocation cores. As a reminder, these sites are referred to as nodes due to their distinctive nature and important role in migration. Nodes are also used as landmark in defining the periodicity of the facet pattern.

Figure 4.2a contains a map of the free volume in and around the pure boundary from Figure 4.1, which corresponds well to the hydrostatic stress data of Figure 4.1d. The rows of Figure 4.2b show snapshots of the boundary with increasing Ag concentrations at 300 K, with the boundary plane indicated by dashed lines to guide the eye. At this temperature, virtually no Ag atoms are left in the bulk, consistent with the positive enthalpy of segregation for Ag in Cu [120]. As shown in the snapshot for 0.1 at.% Ag, atoms segregate first to the IBP facet, specifically to sites of highest positive free volume. These are also generally the sites of the largest positive hydrostatic stresses, as shown in Figure 4.1d. This is consistent with the fact that Ag atoms are larger than Cu atoms and therefore prefer to segregate to interfacial sites under tension. Though out of the scope of this study, one unique possibility for modulating the number and strength of site segregation in faceted boundaries such as this one is through the inclination angle β, which as shown in Chapter 3, can lead to significant changes in the facet periodicity and thus overall energy [78, 121].

For concentrations above 0.1 at.-% Ag, it is clear that the IBP facets are the preferred sites of segregation, with SBP facets only being occupied after IBP facets have been saturated. This trend reflects known relationships between grain boundary energy anisotropy and segregation [123] and can also be explained by the positive enthalpy of mixing of Ag in Cu, which promotes clustering of Ag atoms before the filling of other, relatively high-volume sites in the SBP facet. Interestingly, at 2.0 at.-% Ag there remain sites of low or no solute occupation (black arrows) at the regions on the compressive side of the partial dislocation stress field (dark blue in

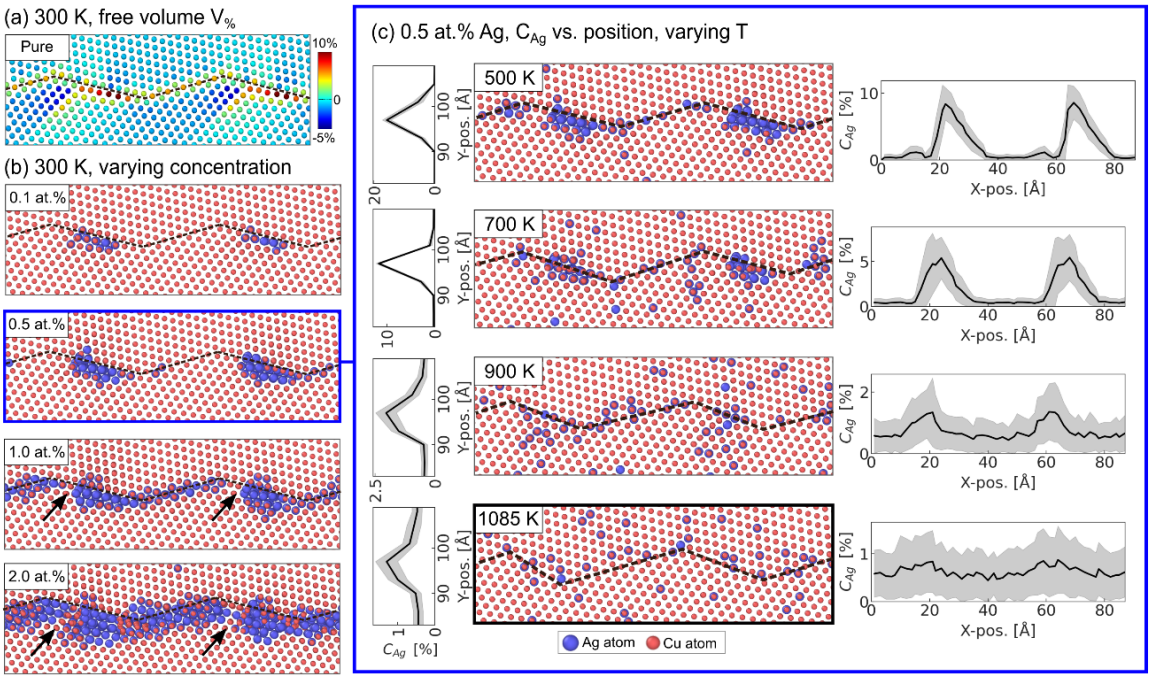

Figure 4.44. (a) Faceted Σ11 boundary at 300 K, colored by free volume, where the dashed lines indicate the boundary position. (b) Atomic images at 300 K with increasing Ag concentration from 0.5 at.% to 2.0 at.% Ag. The sites of largest negative free volume remain relatively free of Ag for 1.0 and 2.0 at.% (black arrows). (c) The effect of increasing temperature for a constant concentration of 0.5 at.% Ag, with spatial composition plots for the Y-direction shown to the left of each snapshot and for the X-direction to the right for each. The final configuration chosen for the mobility studies at 1085 K is outlined in black.

Figure 4.2a). The range of behaviors observed in this boundary underscores the need for nuanced models of interfacial segregation, as mentioned in Chapter 1.2.3. The images of Figure 4.2 are clear example of a case where a single segregation energy for Cu-Ag or even for Σ11 itself is not an adequate description. In the context of a polycrystal, the influence of topologically complex boundaries like these faceted interfaces would be best captured by treating segregation energy as a spectrum, rather than an average, as explored in recent works on Al-Mg polycrystals by Wagih and Schuh [50, 124].

Figure 4.2c shows changes in segregation while varying temperature for the 0.5 at.% Ag sample, with this concentration chosen as it appears to be near the Ag-saturation limit of IBP facets, making the effect of changes in temperature clearer to observe. The rows of Figure 4.2c

present atomic snapshots with local Ag composition along the Y-direction shown to the left and along the X-direction to the right. All spatial composition plots show an average taken over 100 snapshots from different MD steps of energetically equivalent configurations. The data show that dissolution of clustered Ag atoms begins above 500 K. At and below this temperature, samples have peak concentrations of ~20 at.% in the Y-direction, at the grain boundary, and peak concentrations of ~10 at.% in the X-direction, along the IBP facets. An increase in temperature to 700 K begins dissolution of clustered Ag atoms, which reduces the peak in the Y-direction to approximately 11.5 at.% and the IBP facet peaks in the X-direction from approximately 9 at.% to 5 at.% Ag. At 900 K and higher, the Y-axis peak has dropped to under 2.5 at.% Ag and the X-axis peak is only slightly enriched (0.7-1.2 at.% Ag) above the bulk composition of ~0.4 at.% Ag.

4.3.2 Segregation-induced directionally-anisotropic mobility

The complex of faceted boundaries gives them special segregation behavior, just as has been seen with respect to boundary migration in Chapters 2 and 3 (and in some examples from the literature [4, 35, 44]) Since both segregation and migration in faceted boundaries are heavily influenced by local atomic structures, both properties will naturally also heavily influence each other. After escaping initial segregation-induced pinning sites, even the presence of dilute amounts of atoms could affect any of the three shuffling modes described in the previous two chapters (disordered shuffling, Shockley shuffling, and slip plane shuffling). In order to study the nature of interactions between solute atoms (segregated or in the bulk) with shuffling modes, the specimen with 0.5 at.% Ag at 1085 K (corresponding to a homologous temperature of 0.8) was ultimately chosen for mobility studies. As can be seen in the bottom panels of Figure 4.2c (outlined

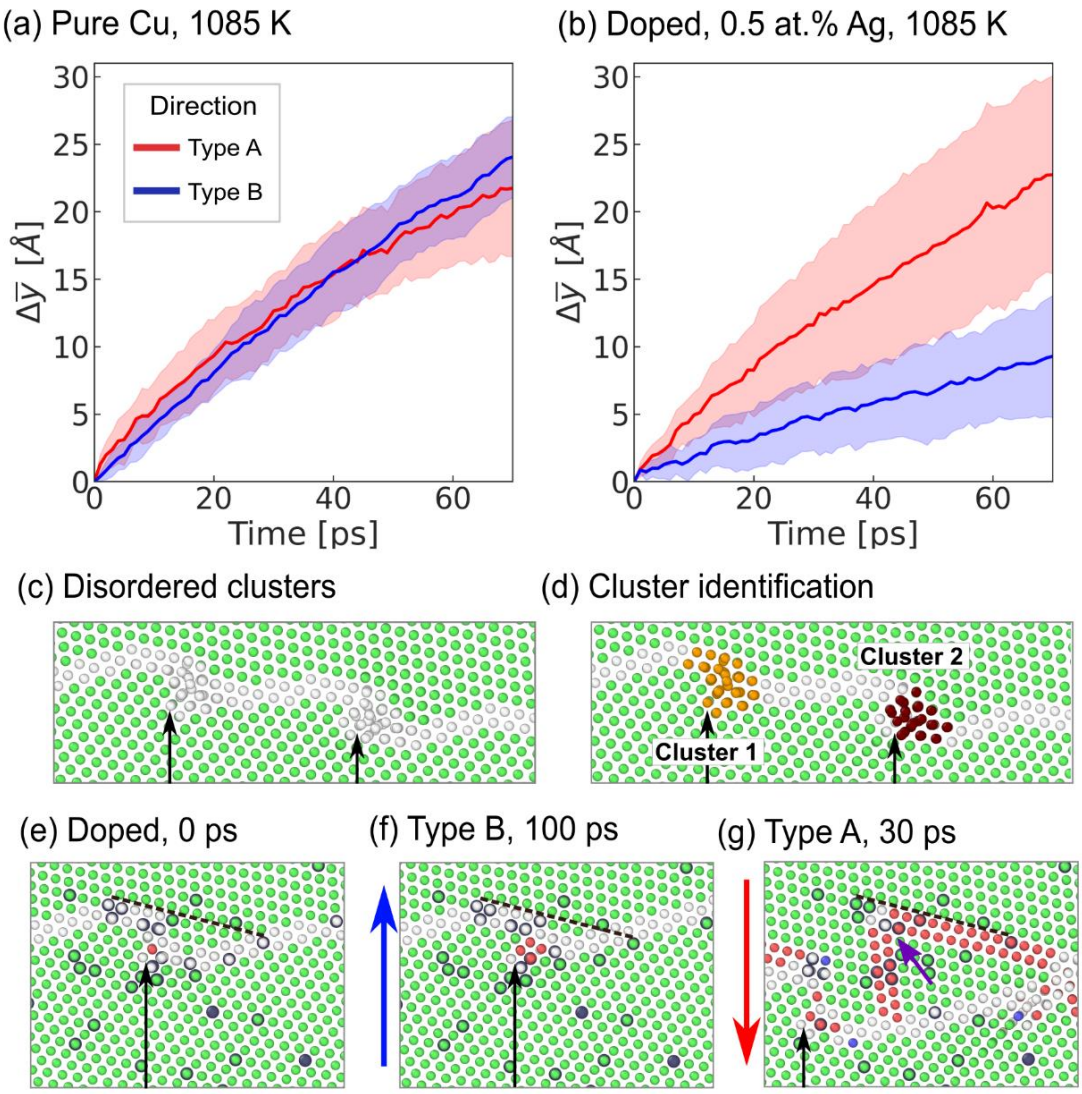

Figure 4.45. (a, b) Mean boundary displacement as a function of time for Type A (red) and Type B (blue) migration for 10 runs each. The two curves of the pure boundaries in (a) overlap, while those in (b) are distinctly different from one another, indicating directionally-anisotropic mobility for the doped samples. (c, d) Examples of disordered clusters that form during node migration. (e) Example of a strongly-pinned facet node before migration, where the dashed black line in Grain A is a fiducial marker oriented along the IBP. (f) Application of the Type B ADF for 100 ps does not result in any node migration. (g) Application of the Type A ADF migrates this segment significantly in 30 ps and also forms a Lomer-Cotrell lock (purple arrow).

in black), this configuration allows for slight boundary segregation (to influence structure) without excessive boundary pinning (which could render the interface immobile). The resulting average trajectories of the pure and doped samples are shown in Figures 3.3a and b, respectively. The

colored regions surrounding each curve shows the standard deviation accounting for the 10 different runs. Mobility, *M*, is calculated from these trajectories using the formula $M = v/P$, where v is velocity and P is the driving force. The pure samples have similar trajectories for Type A (red) and Type B (blue) migration, with average mobilities of 29.2 m·s/GPa and 32.3 m·s/GPa, respectively. In contrast, the doped Type A/B samples have distinctly different trajectories from each other. Compared to the pure Type B boundary, the doped Type B mobility is significantly slower at 12.5 m·s/GPa. The doped Type A mobility, measured at 30.5 m·s/GPa, is approximately the same as that of the pure boundaries, but 2.4 times faster than the doped Type B migration. Although the larger standard deviation in the doped Type A-migrating boundaries compared to the pure Type A indicates that they too are affected by dopants, only the doped Type B-migrating ones appear to be systematically affected.

The significant difference between Type A/B migration means that the doped bicrystals are a further example of directionally-anisotropic mobility. As was thoroughly established in Chapters 2 and 3, the slip plane shuffling mode is ultimately the cause of these differing mobilities in other boundaries. However, since it does not lead to a difference in mobilities in the pure materials, Ag atoms must be affecting slip plane shuffling itself or one of the other two shuffling mechanisms. It was also demonstrated in Chapter 3 that directionally-anisotropic mobility can be well-quantified through analysis of the disordered clusters that are characteristic of the disordered shuffling mechanism. Therefore, in the following section, an exploration of the influence of Ag atoms on slip plane shuffling and disordered shuffling specifically will be undertaken.

4.3.3 Shuffling modes in the presence of Ag

The influence of the slip plane shuffling mode can be illustrated by a node that has been strongly pinned by dopant adsorption, shown in Figure 4.3e. The black arrow indicates the node location, while the dashed black line shows the orientation of the IBP plane and also acts as a fiducial marker in the following panels. As shown in Figure 4.3f, application of the Type B driving force for 100 ps does not result in any node migration. In contrast, the Type A driving force applied to the same structure (Figure 4.3g) results in almost immediate migration. By 30 ps, the node has successfully migrated several Å to the lower left corner, which has in the process lengthened the SBP facet and created two new stacking faults in Grain A. Incidentally, analysis of this defect and very similar ones in pure boundaries with the Dislocation Analysis Algorithm in OVITO [109] reveals them to be Lomer-Cotrell locks, with two stacking faults terminating in a sessile stair rod dislocation (purple arrow). Such Lomer-Cotrell locks provide a feature which will remain in the microstructure and provide a target for experimental characterization in future work. Though this exact example comes from the starting configuration and would not alter the measured Type B mobility, only add a lag time, it is instructive for visualizing slip plane shuffling and this same mechanism is observed to move the boundary past subsequent obstacles during Type A motion through the simulation cell. In contrast, nodes undergoing Type B migration have only movement enabled by disordered clusters and are fully dependent on this mechanism for moving past obstacles. Because these mechanisms operate locally, and nodes migrate generally independently of each other, it suggests that this chemically-induced directionally-anisotropic mobility should operate similarly in many different contexts (i.e., in polycrystalline systems and with variations in solute atom type and concentration) as is the case in similar pure systems [121].

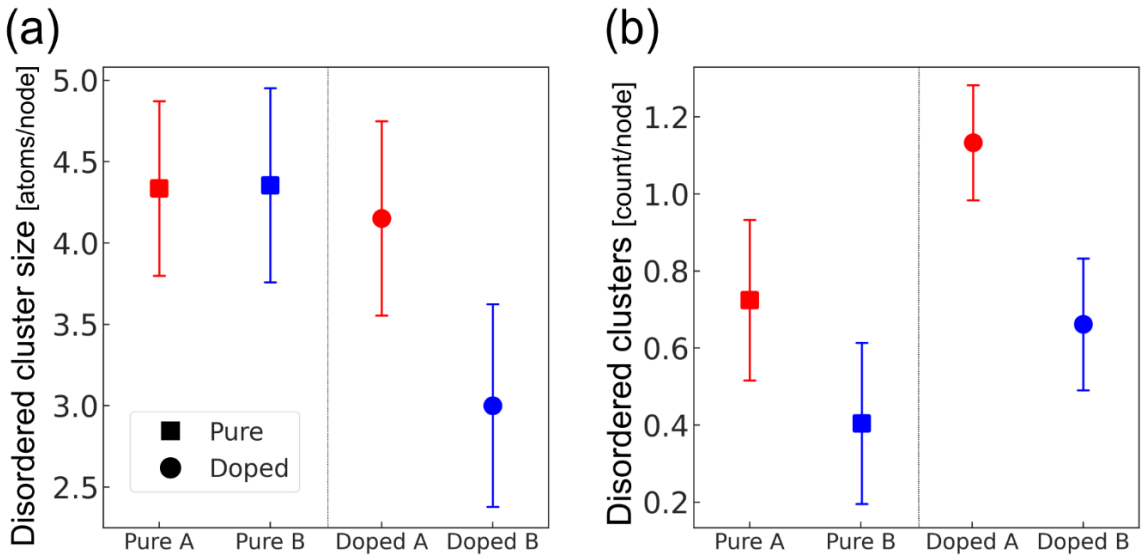

Figure 4.46. (a) The average disordered cluster sizes measured during migration. The pure Type A/B and the doped Type A sizes are very similar to one another, while the clusters in the doped Type B sample are considerably smaller. (b) The average number of disordered clusters counted per node during migration, where a systematic difference between Type A/B counts in both pure and doped boundaries is observed.

To understand whether disordered cluster motion is affected by alloying, the same algorithm from Chapter 3.3.4 for identifying and characterizing disordered clusters during migration was applied (an example of a resulting identification in the doped boundary is shown in Figure 4.3d). The results of this analysis are presented in Figure 4.4, with the data normalized into per node values. Starting with the average cluster size data in Figure 4.4a, disordered clusters during doped Type B motion are significantly smaller than those seen in the other three configurations, which are almost identical to each other, mirroring the mobility values from Figures 3.3a and b. A look at the average number of clusters per node in Figure 4.4b further underscores the importance of disordered cluster size, rather than frequency, for migration. Interestingly, disordered cluster counts are significantly higher for doped boundaries in absolute terms, but doped Type A migration results in very similar mobilities to those of pure Type A/B-

migrating boundaries. Therefore, cluster size is a more important parameter for boundary mobility than the number of clusters formed. Taken together, these plots suggest that dopant atoms act as sites of initial cluster nucleation (hence the higher overall counts in Figure 4.4b) but may also interrupt mechanisms that would increase their size, for example, by interfering with the transport of excess free volume within the cluster [23, 125, 126].

4.4 Conclusions

In summary, we have explored the effects of Ag segregation on the structure and migration of a faceted $\Sigma 11$, $\beta = 15.8^{o}$ boundary in Cu. It is shown that segregation to the facet with more free volume is preferred, with solute atoms remaining concentrated at those sites even up to homologous temperatures of 0.8. Migration studies at high temperature reveal that solute atoms strongly affect boundary velocity only in one motion direction, leading to directionally-anisotropic mobility. This behavior arises from the operation of slip plane shuffling, which is confirmed here as only possible during Type A motion. Once more, it allows the migrating facets, and thus the boundary overall, to initially escape solute pinning. Slip plane shuffling also results in grain boundary migration-generated Lomer-Cotrell locks in both pure and doped boundaries at this inclination angle. This study demonstrates that grain boundary segregation can lead to unexpected migration behavior, even in highly dilute alloys.

5 Emergence of near-boundary segregation zones in face-centered cubic multi-principal element alloys

5.1 Introduction

In previous chapters, we have investigated the behavior of a variety of faceted Σ11 boundaries across a range of temperatures and FCC materials, including a binary alloy (Cu-Ag). To further our understanding of faceted Σ11 boundaries, this chapter explores the effects of segregation in two different FCC MPEA (again, mutli-principal element alloy) variants: a quinary (CuNiCoFeCr) and a quaternary (NiCoFeCr). As described briefly in Chapter 1.2.3, MPEAs are an exciting new class of alloys that hold great promise as advanced engineering materials and are currently only in the very beginning stages of nanoscale interfacial research.

This chapter departs from the study of mobility to focus exclusively on segregation for several reasons. Our preliminary studies of faceted Σ11 mobility in MPEAs revealed that directionally anisotropic mobility and the three shuffling modes are present in the *random solid solution* (RSS), which is a state of the alloy in which all elements are perfectly mixed. However, to induce boundary motion using the ADF, the temperatures and the magnitudes of ΔE needed to be extremely high (T > 90% of melting and ΔE > 0.4 eV/atom). It was also not surprising, as research generally shows sluggish grain growth in these materials. We found that those magnitudes limited our ability to fairly compare the MPEA results with those of Chapters 2-4. Additionally, and arguably more important, is the noted inherent tendencies towards grain boundary segregation. As will be demonstrated in an upcoming section, the dominant segregants in both the quinary and quaternary materials are present in appreciable amounts up to approximately 90% of the melting temperature, which renders the faceted Σ11 virtually immobile.

This pinning was described in a recent study by Utt et al. [127] on a non-faceted Σ11 boundary in a related quaternary alloy (CuNiCoFe).

For the above reasons, this chapter shifts in focus from mobility to the nature of facet segregation in these materials. As of this writing, it is unclear whether or how faceted boundary structure and properties could change in the context of MPEAs. On one hand, the preservation of crystalline order in HEAs implies that many boundaries, including the faceted Σ11s, should maintain important similarities to their counterparts in simpler alloys. Some evidence to date shows that several boundaries in random solid solution (i.e., without segregation) have generally similar morphologies to their pure counterparts [127, 128]. On the other hand, as described in detail in Section 1.2.3, segregation has been demonstrated to induce structural transformations. In this chapter, we test these assumptions, along with reporting on the general segregation tendencies across a range of temperatures.

We finally note that this chapter will involve a minor but important change in terminology with respect to the facets. Because this chapter is focused heavily on segregation over other properties, the naming convention facet's specific plane orientation – the SBP and IBP acronyms – will no longer be used. Instead, attention will be brought to these planes' relative energetic relationships. The SBP facet will be referred to as the *low energy facet*, and the IBP facet will be renamed the *high energy facet*.

5.2 Methods

Atomic interactions for all samples (pure, quinary MPEA, and quaternary MPEA) were modeled with the embedded-atom method potential created by Farkas and Caro [2] for the CuNiCoFeCr system. This interatomic potential was designed with the goal of forming stable,

	Cu	Ni	Co (FCC)	Fe (FCC)	Cr (FCC)
a_0 [Å]	3.52	3.52	3.55	3.56	3.53
$E_{vacancy}$ [eV/atom]	1.19	1.61	1.36	1.61	1.41
E_{110} [J/m^2]	1.31	2.05	2.08	2.00	2.02
E_{100} [J/m^2]	1.25	1.88	1.90	1.86	1.88
E_{111} [J/m^2]	1.24	1.75	1.60	1.70	1.65
Relaxed SFE [mJ/m^2]	43	125	15	43	24

Table 1. Selected properties of the interatomic potential by Farkas and Caro [2]. For each element listed, a_0 is the lattice parameter (FCC), $E_{vacancy}$ is the vacancy formation energy, the E_{001}, E_{110}, and E_{111} are the surface energies for the {001}, {110}, and {111} planes respectively, and the relaxed SFE is the relaxed stacking fault energy.

Material	Pair	ΔH_{A-B}, RSS [2], T = 0 K [kJ/mol]	ΔH_{A-B}, MC/MD, T = 1000 K [kJ/mol]	ΔH_{A-B}, experimental [129] T = 300 K [kJ/mol]
Quinary only	Cu-Cr	0.521	0.337	12
	Cu-Ni	0.703	0.339	4
	Cu-Co	0.428	0.073	6
	Cu-Fe	0.374	-1.008	13
Quinary and quaternary	Co-Ni	0.135	1.359	0
	Fe-Ni	0.176	0.470	-2
	Cr-Fe	0.393	0.375	-1
	Co-Fe	0.109	0.182	-1
	Co-Cr	0.144	0.133	-4
	Ni-Cr	0.095	0.060	-7

Table 2. Enthalpies of mixing ΔH_{A-B} for binary alloy A-B, each of which is present in the quinary and quaternary alloys.

single-phase FCC structures through all temperatures below its melting point. To accomplish this, the potential fitting procedure minimized the total heat of mixing of the random solid solution, leading to pairwise enthalpies of mixing that are also close to zero at 0 K. This design also means that all elemental properties are calculated based on the FCC crystal structure. Of the five elements in this MPEA, only Cu and Ni are natively FCC. At low temperatures, Co has a HCP crystal structure, and both Cr and Fe have BCC. This means that properties such as lattice constants are described in terms of FCC crystal structure. Table 1 contains selected properties with this fact noted for Co, Fe, and Cr.

In this chapter, the potential is used to emulate the eponymous quinary alloy, as well as a quaternary variant with the elements NiCoFeCr. Table 2 includes the reported enthalpies of mixing, along with similar calculations extracted from each equiatomic binary alloy after 0.5 ns of MC/MD simulation at 1000 K. These values are also comparatively low, with a maximum magnitude of +1.359 kJ/mol for the pair Ni-Co (it should be noted that both the reported and calculated values deviate significantly from reported experimental values [129], also included in Table 2 for T = 300 K. Using the melt interface tracking method outlined by Wang et al. [101], the melting temperatures for the quinary and quaternary alloys were determined to be approximately 2090 K and 2040 K respectively, with an error of ±20 K each.

This chapter focuses on the faceted Σ11 boundary with the longest facet period in this dissertation, with an inclination angle of $\beta = 10.2°$. This variant in pure Cu is shown in Figure 1(a) and (b). Figure 1(a) presents a map of the potential energy (eV/atom) of this boundary, highlighting the positions of the low and high energy facets (again in previous chapters, named the SBP and IBP facets, respectively). Dark blue coloring indicates atoms with potential energies near the average energy of cohesion E_{coh} for Cu in this potential (-3.54 eV/atom, Table 1) and corresponds to bulk atoms. The high energy facets are quickly identified by regions of orange and red colored atoms (averaging around -3.37 eV/atom), while the atoms of the low energy facets remain in the light blue to medium blue color range of the potential energy spectrum. Figure 1(b) highlights this boundary's structural order using the same CNA coloring as seen in previous chapters, with solid and dashed lines included to indicate the low and high energy facets' plane orientations, respectively.

In order to make use of the insights into faceted Σ11 boundaries gained in the previous chapters, we opted to remain with our initial bicrystal creation methodology (the reader is referred

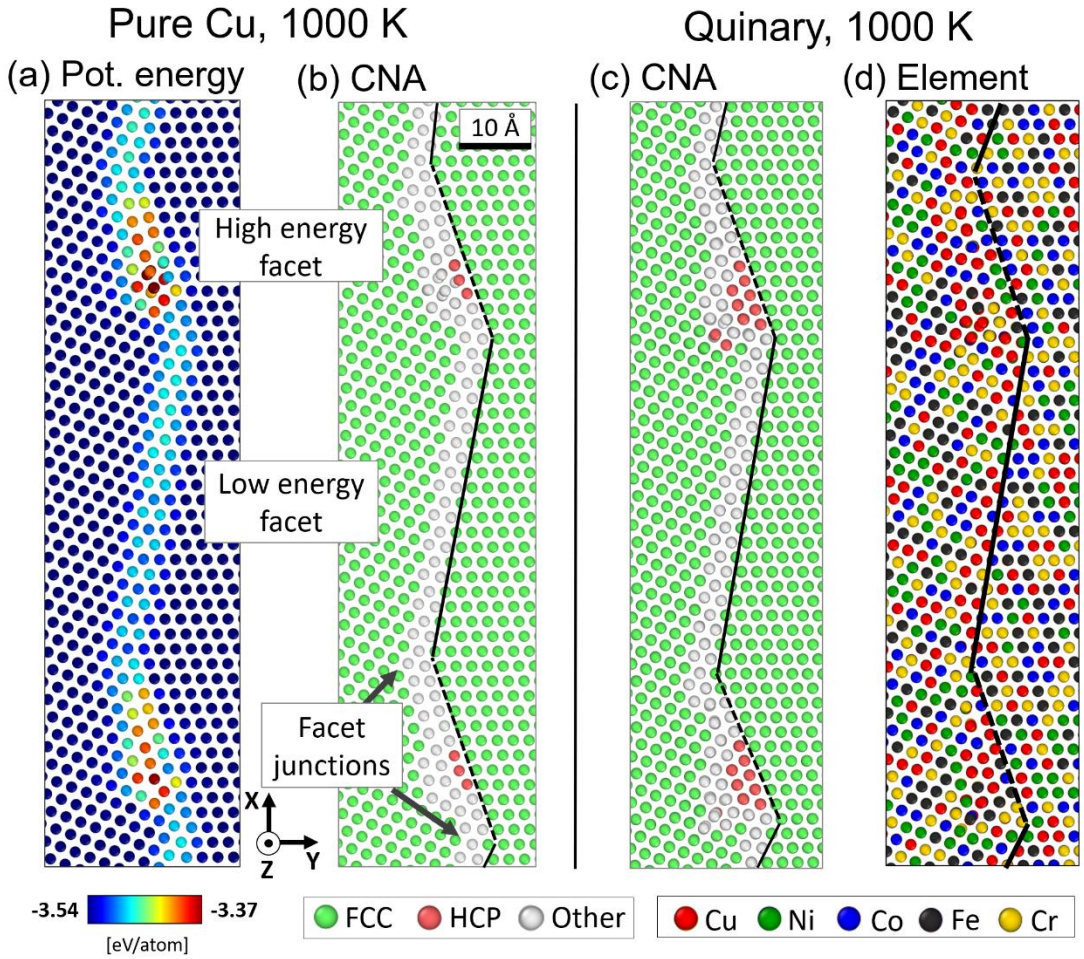

Figure 47. Examples of the faceted Σ11 boundary morphology. (a, b) The boundary in pure Cu, with atoms colored by potential energy (eV/atom) in (a) and colored by Common Neighbor Analysis (CNA) in (b). The high energy facets have groupings of yellow to red colored atom (high potential energy) and are outlined with a dashed line in (b), and the low energy facets have light blue to dark blue atoms in (a) and are outlined with a solid line in (b). (c) The same boundary in the quinary MPEA (CuNiCoFeCr) after 1 ns (50,000 MC steps) of MC/MD simulation. (d) An example of the elemental makeup of the boundary in (c).

to Chapter 2.2 for the detailed description). Since the algorithm from Ref. [85] is designed to generate pure crystals, the initial faceted bicrystal must also be created from a single element. Though all elements of this potential were fit to have an FCC crystal structure through all temperatures, only Cu and Ni are natively FCC. Thus, they were chosen as initial candidates for cell generation. A previous study on faceted Σ11 boundaries using six different FCC potentials showed the influence of stacking fault energy on faceted boundary morphology and

properties [130]. Between the two elements, pure Cu (from the same interatomic potential) has the closest relaxed stacking fault energy to the reported average for CuNiCoFeCr (50 mJ/m^2). Cu was therefore chosen to generate the initial bicrystal at T = 0 K, which at T = 0 K had the cell dimensions of L_x, L_y, L_z ~ 270 Å, 200 Å, 36 Å containing 162,288 atoms.

To create the fully segregated quinary and quaternary alloys, a hybrid MD/Monte Carlo (MC) algorithm was applied to the RSS bicrystals. To control temperature and maintain vacuum pressure for all parts of the simulation, a Nosé-Hoover thermostat and barostat were applied to the cell using the NPT ensemble with a timestep of 1 fs. To initiate annealing, kinetic energy equivalent to approximately half the target temperature was added to the cell and temperature was ramped over 20 ps up to the target value. The structure was then annealed for a further 30 ps. After annealing, the hybrid MC/MD method was applied to the structure to allow segregation to the grain boundaries. To regulate the pair swaps for atoms i and j in the semi-grand canonical ensemble, the difference in pair-wise chemical potential energies, $\Delta\mu_{ij}$, were found for each temperature using an iterative algorithm optimizing the acceptance rate of atom swaps and potential energy reduction. The variance constraint parameter κ was set to 10^3, which keeps the standard deviation of concentration values beneath approximately 0.05% beneath the target concentration. For every 20 MD steps, one MC step was performed, which randomly selected 25% of the atoms in the cell to swap. Each simulation was run for 1 ns, leading to a total of 50,000 MC steps. At least three runs were completed for each material, boundary, and temperature combination, initiated using three unique numerical seeds for kinetic energy randomization. All data represent samples from every 100 ps of MD simulation time (alternatively, every 5,000 MC steps) starting from 400 ps of each MC/MD run, giving a total of 21 samples per combination.

Boundary snapshots of the segregated structures are taken from the final timestep (that is, the segregated state at 1 ns) unless otherwise indicated.

Figure 1(c) and (d) show an example of the CNA structure and elemental distribution, respectively, of one boundary after 1 ns of MCMD simulation. Since grain boundary segregation in traditional alloys has been demonstrated to induce structural transitions [54], the preservation of faceted grain boundary structure after segregation is important to establish for faceted boundaries in MPEAs. In a hybrid experimental/computational study, Priedeman and Thompson [54] showed how Au segregation to faceted Pt boundaries can alter facet periodicity, a fundamental structural property of faceted boundaries in pure materials. As can be seen by comparing the pure Cu boundary in Figure 1(a) to the fully segregated quinary shown in Figure 1(c) and (d), there is no evidence of structural transformation in the Σ11 boundary studied here, Though not shown, the same can be said for quaternary alloy (not shown), which in general strongly resembles the example shown in Figure 1(c).

5.3 Results and discussion

5.3.1 Segregation trends in the quinary and quaternary

The composition per element, C (in at.%), versus position of the quinary boundaries at 1000 K is shown in Figure 2(a). The center of the plot is centered around the mean boundary position, with data captured for both the upper and lower boundaries in the bicrystal. A small schematic of the binning direction is included as an inset. The thicker colored lines indicate the average fraction for each element, and the shaded bands around them show the standard deviation. At this temperature, Cu is clearly the dominant segregating element, with maximum average values of 29.4 at.% as compared to the initial concentration of 20 at.% for all components. Of the four

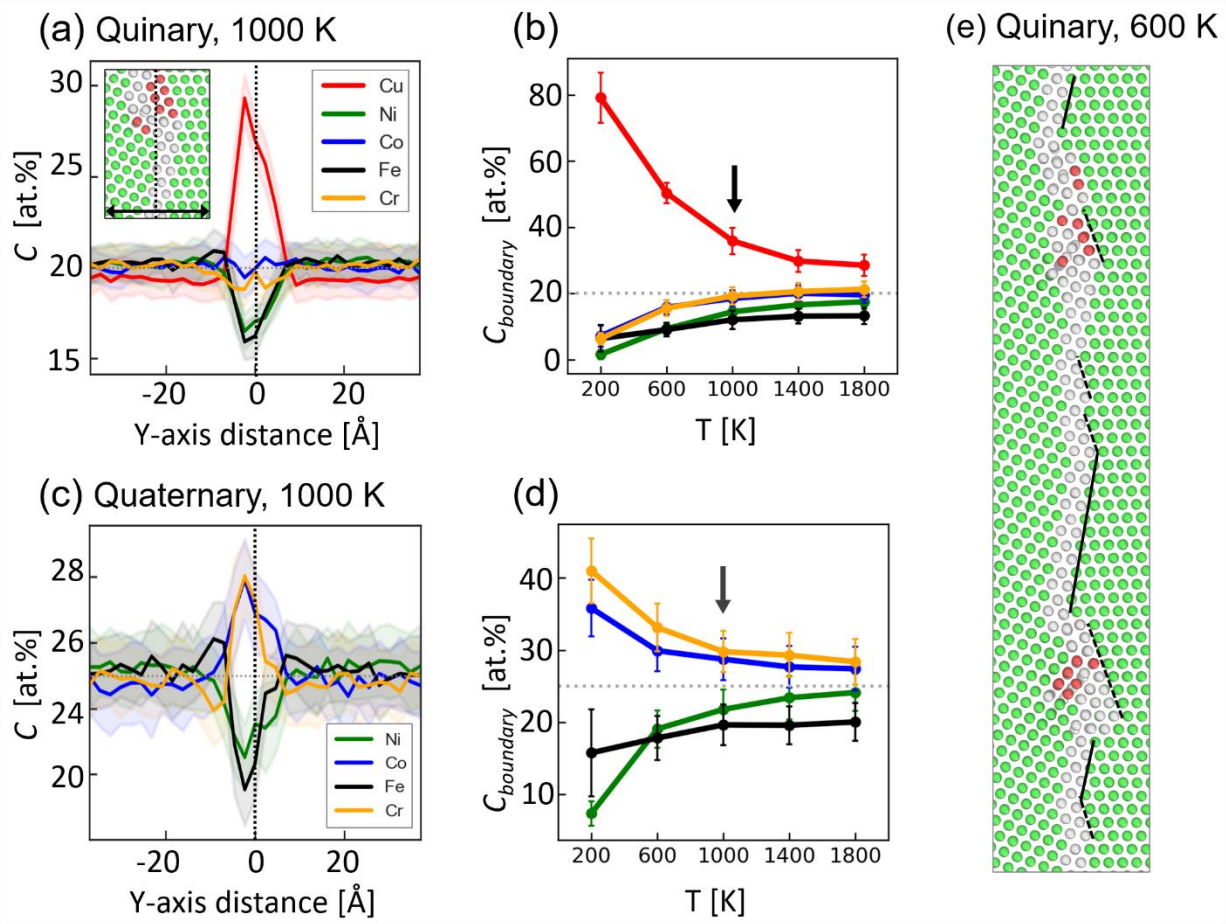

Figure 48. All error bars/shaded bands in this and following figures show the standard deviation of each measurement. (a) Composition as a function of Y-position data reflecting the aggregated segregated state of both grain boundary and surrounding bulk in the quinary material. The inset provides an orientation for the direction of measurement. (b) Composition vs. temperature data for the grain boundary atoms (non-FCC-ordered) alone. The arrow points to the temperature shown in (a). (c) Composition vs. Y-position for the quaternary alloy, NiCoFeCr (without Cu). (d) Composition vs. temperature data for the grain boundary atoms of the quinary material. (e) An example of a partially de-faceted boundary at 600 K. To avoid de-faceting, the remaining visualizations and analyses were run on boundaries at 1000 K (see Figure 1(c) and (d)).

remaining elements, only Co remains near the initial concentration within the boundary. Cr, Ni, and Fe are depleted from the boundary, with the latter two being depleted most strongly. The strong Cu segregation has led to mild depletion of Cu in the bulk (approximately 19.4 at.% on

average), a phenomenon predicted by the model of Wynblatt and Chatain [74] for alloys with strongly-segregating elements in polycrystals with grain sizes beneath 100 nm.

Figure 2(b) shows the grain boundary composition as a function of temperature from 200 K to 1800 K, which correspond respectively to homologous temperatures of approximately 0.1 to 0.9. Note that, in contrast to the binned data of Figure 2(a) which tracks both FCC and non-FCC atoms, the composition-temperature analysis in this figure only tracks non-FCC (i.e., grain boundary) atoms. Increasing temperature decreases the amount of segregation, with the steepest decreases in Cu segregation occurring from 200 K to 1000 K. These decreases become significantly pronounced between 1000 K and 1800 K, indicating that changes in solubility are non-linear. Notably, even at the highest temperature of 1800 K, there is still significant enrichment of Cu of approximately 5.1 at.% over that of the bulk. Also notable is the slight boundary enrichment of Cr occurring at 1800 K, by approximately 1 at.%.

The dominance of Cu adsorption at the boundaries in Figure 2(a) and (b) is consistent with what has been reported about elemental segregation in this material and variants. Several experimental studies of heat-treated CuNiCoFeCr indicate that this material separates from an initially-homogeneous mixture into two FCC phases, one Cu-rich and the other Cu-lean [131–133]. Atomistic studies of a related quaternary material, CuNiCoFe (using the interatomic potential from Zhou et al. [134]), also exhibited significant Cu segregation to irradiation-induced defects [71] as well as to a non-faceted Σ11 grain boundary [127]. The fact that Cu segregation remains strong and consistent with other experimental and computational results, despite the noted discrepancies in mixing enthalpies, suggests that the elastic and energetic terms play a larger role in those MPEAs than alloy interactions in grain boundary segregation as well.

A common equation describing the enthalpy of grain boundary segregation, developed by Wynblatt and Ku [77, 135], provides a useful qualitative framework for understanding the behavior of segregants such as Cu in this work. It has three terms: the boundary energy term, the alloy interaction term, and the strain energy term:

$$\Delta H_{seg} = -\frac{24\pi B\mu r_I r_M (r_I - r_M)^2}{3Br_I + 4\mu r_M} + (\sigma_I - \sigma_M)A^{\phi} - \frac{2\Delta H_{mix}}{ZX_I X_M}\left[Z_L\left(X_I^{\phi} - X_M\right) + Z_P\left(X_I - \frac{1}{2}\right)\right] \quad (1)$$

In all parts, the subscripts I and M denote the solute and solvent contributions, respectively, and terms without those subscripts refer to properties of the solvent element. The first term describes the strain energy contribution to the segregation enthalpy, defined in terms of the solvent's bulk modulus *B*, the solvent's shear modulus μ, and the differences in atomic radii between the pair of elements. The second term in Equation 1 describes the driving force for segregation induced by the difference in grain boundary energy σ for the solute and solvent, multiplied by the interfacial area per volume A^{ϕ}. The remaining third term quantifies the influence of alloy interactions, or in other words, the driving force contribution due to the chemical interactions of elemental pairs. In this formulation, there are several variables. ΔH_{mix} is the enthalpy of mixing for solute-solvent (I-M) pairs, X_i describes the concentration of a component at the interface, X_I^{ϕ} describes the concentration of the solute within the boundary, Z is the total coordination number per atom, and Z_i represents the coordination number in different regions (L within its own plane and P across-plane).

With respect to the first two terms of Equation 1 above, Cu is by far the most favored element for segregation in the quinary alloy. Starting with the strain energy term, Cu atoms have by far the largest lattice parameter a_0 for the FCC structure of any element in this potential (Table 1), meaning Cu also has the largest atomic radius. Therefore, Cu atoms will yield the largest

negative strain energy term for segregation enthalpy, and consequently relieve the most strain per atom after segregating. The basic energetic properties of Cu atoms also promote its segregation. Though clearly surfaces and vacancies are different structures than grain boundaries, they are all expressions of the energy penalties resulting from dangling bonds. Because Cu has by far the lowest average values for $E_{vacancy}$,, E_{100}, E_{110}, and E_{111} (Table 1), defects with aggregations of Cu atoms will also tend to have lower energy penalties as well. Thus, Cu as the dominant boundary segregant is consistent with the second segregation enthalpy term as well.

The final term of Equation 1, that describing alloy interaction, is likely less influential than the first two terms. As described in the Methods section and shown in Table 2, the enthalpies of mixing in this interatomic potential were kept deliberately very low, and the values measured for pairs in solid solution at 1000 K are also low. However, it should be noted that three of the four pairings have positive enthalpies of mixing and would thus promote Cu segregation, even if weakly. The major exception to this is the pair Cu-Fe, which has the only calculated negative value of -1.008 kJ/mol, indicating interatomic attraction. Other elemental interactions not described by Equation 1, such as site competition, could explain the apparent discrepancy, and will be explored in upcoming sections.

Segregation trends in the quinary resemble the behavior seen in strongly-segregating binary alloys. To study a similar MPEA with more complex trends in segregation, the same simulations and analyses performed on the quinary alloy were also completed for the Σ11 boundary in a quaternary variant without Cu, namely, NiCoFeCr. The composition versus position data is shown Figure 2(c) (note that the equiatomic bulk composition for this material is 25.0 at.%). Cr and Co both become roughly equally enriched, while Ni and Fe maintain their roles as the most heavily depleted elements as in the quinary alloy. As a pair, Co and Cr play a similar role as Cu does in

the quinary with respect to the boundary energy term. The two co-dominant segregating elements in the quaternary, Cr and Co, have lower energies for both vacancy formation and {111} plane energies than those of Fe and Ni by a significant margin. These energy trends suggest that segregation would be favored for Cr and Cu over Ni and Fe, which is exactly what is observed in the quaternary. Additionally, the segregation of Cr is consistent with the first-principles calculations on this quaternary alloy conducted by Middleburgh et al. [136], who found that Cr is not thermodynamically stable in solution and would have a tendency to segregate.

Interestingly, there appear to be couplings of the composition curves of the element pairs Co/Ni and Fe/Cr. The strong depletion of Fe and Ni appears to be characteristic for both materials, and the anti-symmetric pairings of Co/Ni and Fe/Cr indicate an inverse coupling of these elements' compositions. These pairs tend to trend in anti-symmetric fashion in a way not seen in the quinary material and appear to extend outside of the boundary plane, especially on the left side of the plot (dotted vertical line). As in the quinary, there is a region of mild but noticeable Fe enrichment (26.3 at.% on the left side and 25.6 at.% on the right) at the outside of each facet junction. These regions suggest that segregation trends beyond simply the grain boundary itself may need to be considered in MPEAs. This topic will be explored further in an upcoming section.

Though segregation does not appear to affect the faceted Σ11 boundaries' structure, changes in temperature do have a documented effect. The pure Cu boundary undergoes a faceting/defaceting transition between approximately 825 and 955 K. Below this temperature, there is still a periodic repeat of the high-energy facets' defect structures, recognizable by clusters of HCP atoms. However, the low energy facets decompose into irregular, unpredictable groupings of low and high energy facet segments (i.e., the symmetric plane orientation and the incommensurate one), an example of which is included in Figure 2(e). For this reason, all

boundary snapshots and detailed structural analyses are conducted at a temperature of 1000 K (a homologous temperature of approximately 0.5), where the vast majority of the low energy facets for all runs are at a maximum length. It should also be noted that this behavior has been noted in faceted Σ11 boundaries in Al in experiment [29].

5.3.2 Spatial variations in composition for different facets

The two methods used in Figure 2 to obtain boundary composition data, namely binning atoms by position or extracting only non-FCC atoms, are useful for a general overview of segregation tends. However, these methods obscure the individual contributions of the low and high energy facets to overall boundary enrichment and depletion. As described in the Introduction, there is increasing evidence that understanding site-specific segregation tendencies [50], including those to facet planes and junctions [53–55] is critical and will be an important consideration in future alloy development. There is also evidence from traditional alloys that regions near grain boundaries may also play an important role in microstructure evolution. Zhao et al. [137] et al. demonstrated in an Al-Zn-Mg-Cu alloy that solute-enriched grain boundary regions lead to the creation of depletion zones directly adjacent to them, altering the kinetics of precipitate formation in fundamental ways. For these reasons, an analysis of each facet type (low and high energy) as well as the regions near them was conducted.

Though a similar spatial binning technique as used in the composition-position data of Figure 2(a) and (c) could also be conducted for each facet type, atomistic simulations also allow a study of the properties of individual atomic planes. This kind of analysis is especially suited to high symmetry boundaries such as the low energy facet in the Σ11 boundary under study. To conduct such a plane-by-plane analysis on a faceted boundary, it is necessary to rotate the original

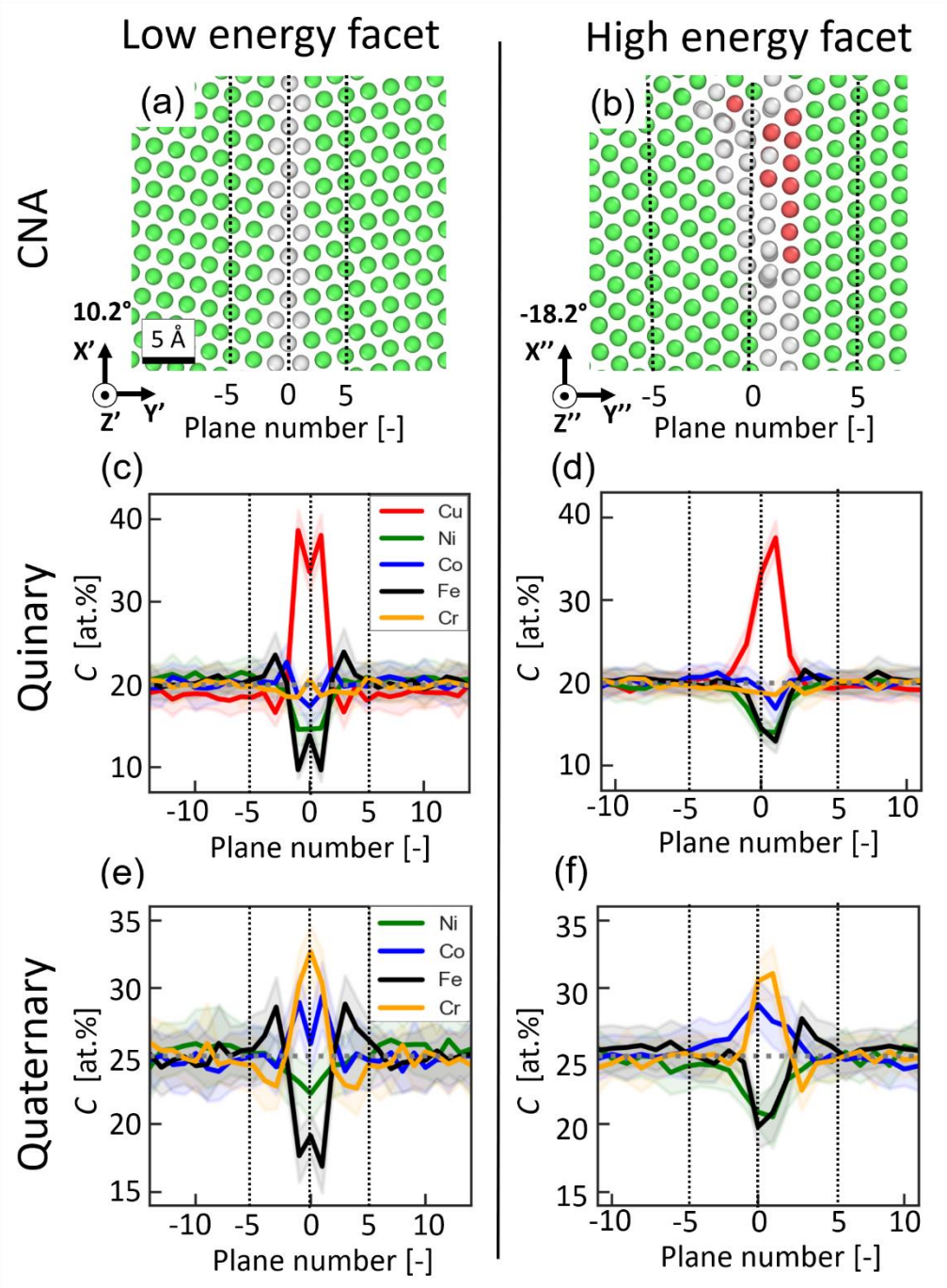

Figure 3. Plane-by-plane analysis of the two different facets from Figure 1 at T = 1000 K. In the first row, an example of how the (a) low energy facets and (b) high energy facets were rotated for plane-by-plane analysis. Plane numbers -5 and 5 are shown on both for reference. (c, d) Composition vs. plane number for the quinary facets. The dotted vertical lines are shown for reference and correspond to the plane numbers shown in (a) and (b). (e, f) The same analysis done on the facets in the quaternary material.

coordinate system (denoted with X, Y, Z) used in Figure 1(a) to align one axis parallel to the facet. For the low energy facets, this required a rotation of approximately 10.2° (X', Y' Z'), resulting in the orientation shown in Figure 3(a). Starting with the central plane marked as Plane 0, each neighboring plane is numbered with a positive or negative integer indicating its relative position, shown for Planes -5 and 5. A similar procedure was performed for the high energy facets, using a coordinate system rotation of -18.2° (X'', Y'', Z''), shown in Figure 3(b). Because the high energy facet is asymmetric, its planes are not perfectly perpendicular with the facet norm direction Y'', and it also contains some irregular defects on its left side. To account for these features, each plane was measured not directly parallel to the coordinate system, but at with a slight angle (~3°). It is also important to note that the plane numbers between the low and high energy facets correspond to different distances in space. For example, the region between Planes -5 and 5 in the low energy facet spans ~11 Å, while the same plane number range in the high energy facet spans ~17 Å.

The resulting analysis of elemental composition versus plane number for the quinary and the quaternary alloys at T = 1000 K are shown in Figure 3(c-f). The quinary data for the low energy facets is presented in Figure 3(c). While the overall trends from the boundary composition data from the previous analysis in Figure 2(a) are the same, one clear difference is the highly symmetric and ordered patterns of enrichment and depletion corresponding to each plane. Though examples can be found for each element, these patterns are especially clear in the elemental pair Cu/Fe. Cu enrichment reaches its maximum of ~39% at Plane -1 and Plane 1 and Fe its lowest value of approximately 10% at those same planes. Interestingly, the Cu/Fe pair simultaneously experience a small dip/increase in their compositions in Plane 0. This pair also swaps roles in the FCC-ordered Planes -3 and 3, where Fe becomes lightly enriched (~23%) and Cu mildly depleted (~18%). This pattern of segregation outside of the grain boundary is reminiscent of the trends in

segregation near facet junctions observed in Figure 2(a) and (c). The data for the high energy facet is shown in Figure 3(d). As it is overall less ordered in its structure than the low energy facet, there are correspondingly fewer clear changes in composition. The more heavily defected right side of the facet appears to resemble the aggregated Y-position data from Figure 2(a). However, Plane 0 and Plane 1 are more ordered on average and have only slightly lower maximum Cu enrichment values than seen in the low energy facet, and similar Cu/Fe coupling is also evident.

The same analysis for the low energy facet of the quaternary alloy is shown in Figure 3(e). The same symmetric patterning of composition as seen in the low energy facet of the quinary is evident in this facet as well. Cr is the dominant grain boundary segregant, reaching its maximum enrichment at Plane 0, followed by Co, which has its highest values at Planes -1 and 1 of around 29%. Fe depletion is also strongest at Planes -1 and 1 (between 16-17%). Compared to the low energy facet, the high energy facet in Figure 2(f) has significantly less ordered trends in enrichment and depletion. Cr is once more the strongest segregant, followed by Co. Both Ni and Fe are more equally depleted, reaching minimums of approximately 19 and 20 at.%, respectively. In both the low and high energy facets of the quaternary alloy, the pairing of Cr/Fe appears to be coupled to some extent, similar to the trends noted in the description of Figure 2(c) and (d). This enrichment/depletion relationship is especially obvious in the regions outside of the boundary, specifically beginning at Planes -3 and 3 and extending through at least Planes -5 and 5, and even to approximately Plane 7 or 8 on the right side of the low energy facet.

On balance, two important trends emerge from the plane-by-plane analysis of elemental segregation. First, in the two highly symmetric low energy facets of Figure 2(a) and (c), there are clear tendencies towards plane-based enrichment and depletion of certain elements within the grain boundary itself, such as that observed with the pair Cu/Fe. Such tendencies underscore findings

that grain boundary character is an important factor in segregation in MPEAs [75, 76]. Second, there are consistent regions of Fe enrichment of Planes -3 and 3 in three out of four examples (Figures 3(c) and 3(e-f)), as well as weaker but still significant Fe enrichments near the facet junctions in Figure 2(a) and (c). Important to note is that these regions could be easily missed if using the wrong analysis technique. Planes -3 and 3 as well as the edges of facet junctions are in FCC-coordinated regions, they would be missed by methods such as CNA which only capture non-FCC atoms.

5.3.3 Atomic volume and segregation trends

The presence of segregation in FCC-ordered regions near the facets implies that there may be local structural deviations that influence local atomic ordering, very similar to how the grain boundary itself induces segregation. Thus, the same tools that are used to analyze grain boundary segregation could also be applied to FCC regions to understand the source of Fe enrichment. One way to analyze segregation tendencies of grain boundaries in terms of structure is through an analysis of atomic volume. As a parameter, atomic volume (or a related parameter of atomic density) is useful for understanding trends in boundary structure in general [119, 138] as well as in MPEAs. As an example, Figure 4 shows the relationships between grain boundary structure and atomic volume in the low energy facet in the quaternary material at T = 1000 K. Figure 4(a) shows a segment of these facets in detail. Low energy facets consist of three plane layers, labeled with the plane numbers corresponding to those of Figure 3. They can also be seen as a chain of diamond-like structures, two examples of which are outlined in the middle of the snapshot. The vertices on the diamonds' long axis are linked to each other and together, form Plane 0 (dotted lines), while the outer two corners of each diamond touch Planes -1 and 1 (dashed lines).

In terms of atomic volume, the symmetry of the diamond shape means that atoms in Planes -1 and 1 are structurally most similar to each other, and correspondingly distinct from Plane 0.

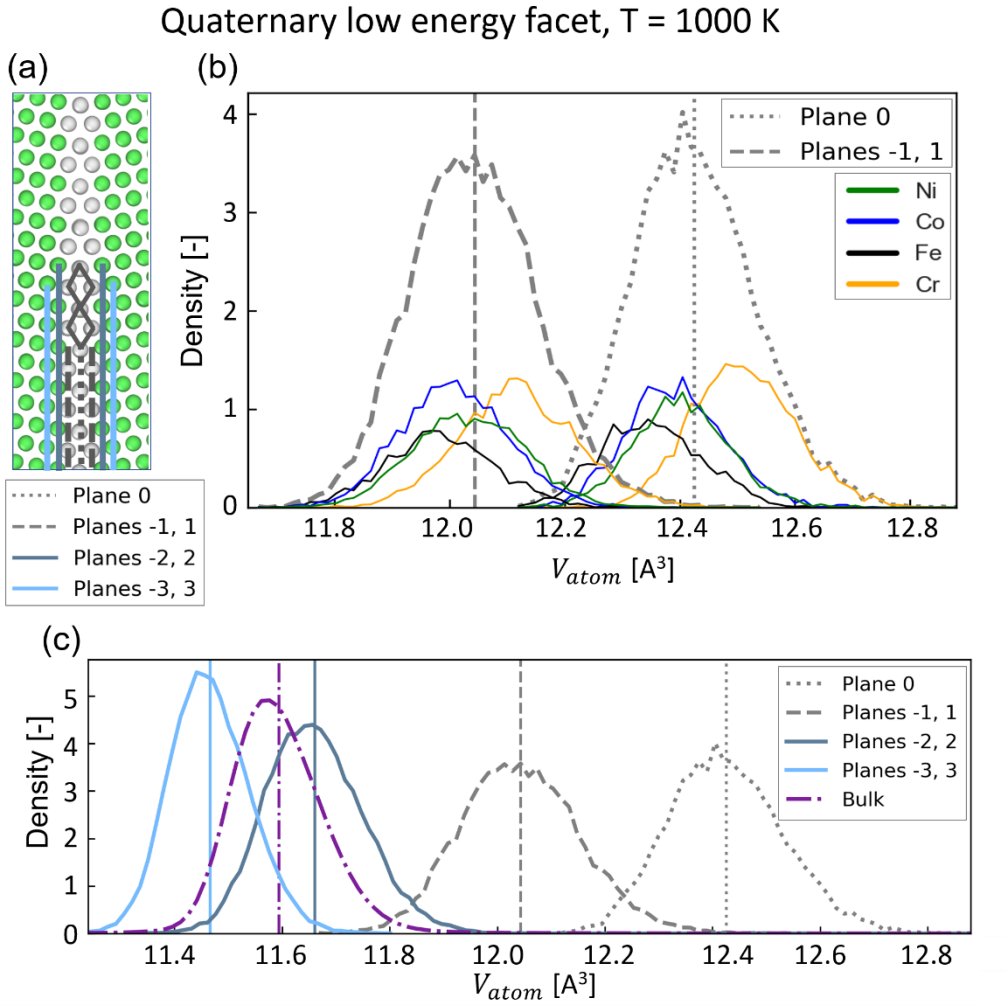

Figure 4. Histograms showing the atomic volume distributions for the low energy facet and surrounding FCC-ordered planes in the quaternary alloy at 1000 K. Because planes have varying numbers of atoms, distributions have been normalized so that their cumulative area is equal to one. The mean of each distribution is shown with a vertical line. (a) Details on the structure of this facet. It can be characterized as a chain of diamond-shaped units (gray outline). Lines indicating the position of various planes are shown on the facet snapshot as well as in a legend beneath it. (b) The volume distributions for atoms in Plane 0 (dotted line) and Planes -1 and 1 (dashed lines). (c) The volume distributions for Planes 0 through -3 and 3, as well as for the bulk crystal (purple). Unexpectedly, Planes -3 and 3 have volumes lower than that of the bulk crystal.

These relationships are detailed in Figure 4(b), which shows a histogram of atomic volume data (bin width: 0.015 Å^3). The three distinct gray curves (dotted, dashed, and solid) corresponding to

each plane type (Plane 0, Plane -1/1) show the cumulative atomic volume data for that type, and the colored curves encompassed by them show the per-element breakdown. The vertical lines for each plane type indicate each of their mean atomic volumes. To compare plane types to each other, the distributions are normalized by density, so that the areas beneath each gray curve (or the sum of their per-element distributions) equals one. There is a clear delineation between the atomic volumes of Plane 0 atoms versus those found in Planes -1 and 1, with the latter being consistently significantly larger than the former.

As noted in Figure 3, Planes -3 and 3 in several configurations exhibit an unexpected enrichment of Fe atoms. For that reason, Figure 4 includes an analysis of two layers of FCC-ordered planes adjacent to the boundary. The positions of Planes -2 and 2 (gray solid lines) and Planes -3 and 3 (light blue solid lines) are shown in both Figure 4(a) in the boundary snapshot, and their cumulative atomic volume distributions (without per-element breakdown) are shown in Figure 4(c). For comparison, the cumulative data for Planes 0 and -1 and 1 as well as the volume distribution for atoms in the bulk crystal regions is also shown (colored purple, dash-dot pattern). An unexpected trend in the volumes of the atoms in Planes -3 and 3 emerges when comparing to the other planes and bulk. Given the thinness of the low energy facet and the large difference between the peak value at Plane 0 and the bulk mean (~0.86 $Å^3$), it is not unreasonable to expect a few FCC planes neighboring the boundary might have elevated atomic volumes. This is true for Planes -2 and 2, whose mean rests at approximately 11.66 $Å^3$, which is smaller than that of Planes -1 and 1 (12.05 $Å^3$), but still larger than the average for atoms in the bulk crystal regions. However, at 11.46 $Å^3$, the mean volume of atoms in Planes -3 and 3 is significantly lower than the bulk. That the volumes of FCC-ordered atoms drop from being elevated relative to the bulk to values beneath

the bulk within one plane distance is surprising and provides a starting point to investigate structural connections between Fe enrichment in FCC-ordered regions from Figure 3.

The next step is to investigate whether the reduced volumes of Plane -3 and 3 in the quaternary low energy facet are also present in the other configurations. Because MPEAs are chemically complex, it is also important to establish whether this drop is present in chemically inert structural reference state, after which the effects of multiple components can be better understood. These relationships are explored in Figure 5(a) and (b) for the boundary in pure Cu, which shows a plane-by-plane analysis of the average atomic volumes, $\bar{V}_{atom}$ (units of Å^3), for each facet. The grain boundary planes (again, those identified with a majority of non-FCC atoms by CNA), are indicated using a shaded gray box. Note that, for the high energy facets, the defects on their left side make an exact cutoff somewhat, though on average the defects were found to extend to approximately Plane -2. Dotted lines indicate the average atomic volume per element measured on atoms in FCC regions at least ±25 planes away from facets.

Figure 5(a) shows the per-plane volume data for pure Cu atoms in the low energy facet. As seen with composition, the high symmetry of these facets is demonstrated again in the atomic volume data, which peaks at Plane 0 and drops rapidly until Planes -3 and 3. Interestingly, at these planes, the average volume value (12.55 Å^3, the mean of both sides) is lower than the bulk atomic average (12.62 Å^3), with a difference of approximately 0.07 Å^3. The volume then increases gradually over the following five or six planes, where it converges to the bulk average. The same general pattern can be observed in the high energy facet data of Figure 5(b) in both grains, despite this facet's less consistent structure (reflected in the much larger error bands of the high energy facet). For all facets, volumes converge to the pure Cu bulk value by approximately Plane -8 and

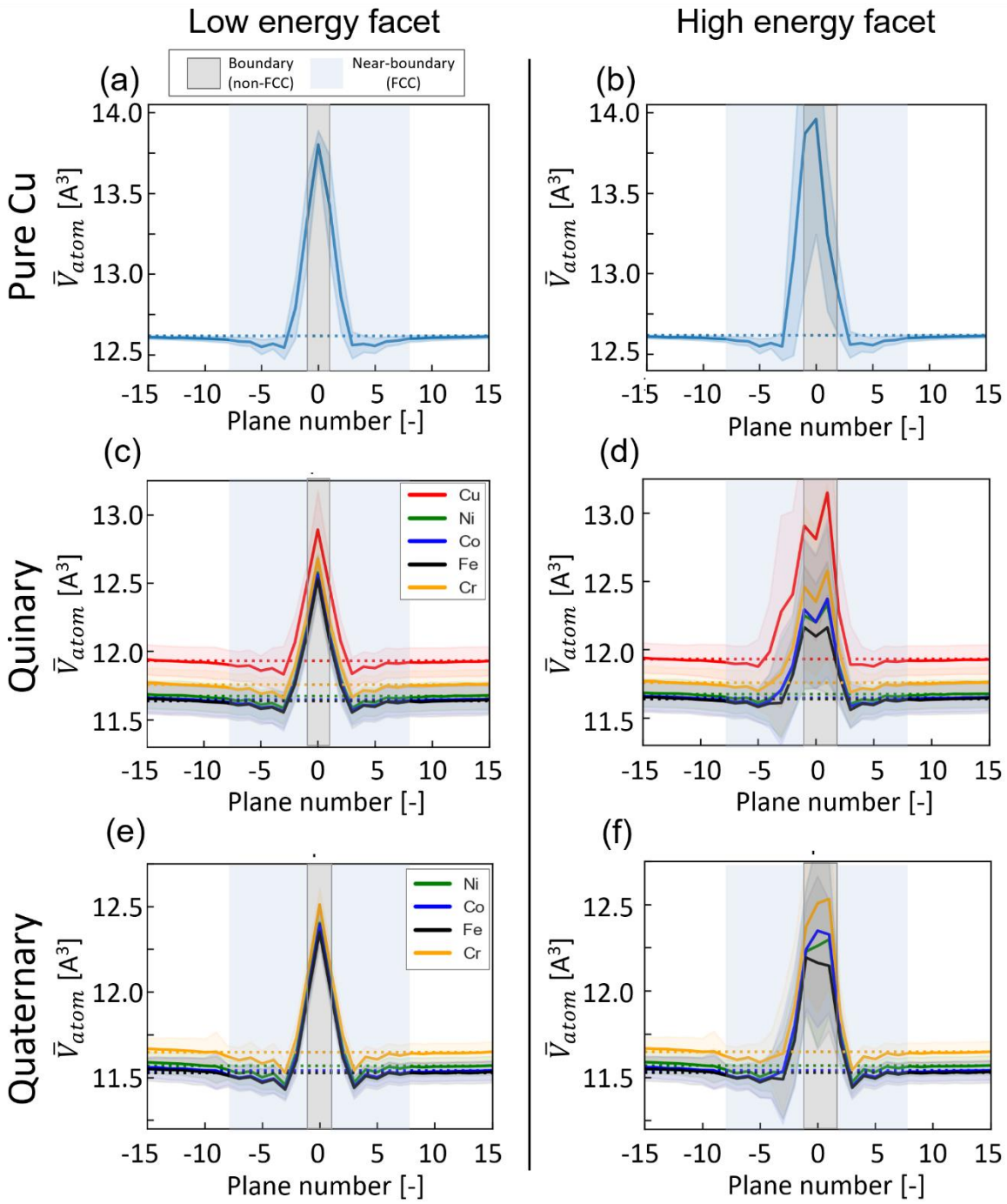

Figure 5. The atomic volume plotted as a function of plane number for both facets at T = 1000 K. Dotted lines indicate the bulk average volume for each element. Gray shaded boxes outline the boundary (non-FCC) planes, and the blue shaded boxes define the near-boundary region (FCC), in which average atomic volumes are reduced relative to bulk values. Data is shown for both facets of (a, b) the pure Cu boundary, (c, d) the quinary alloy, and (e, f) the quaternary alloy.

8 on average. As a whole, it can be stated that the presence of the grain boundary introduces a physically distinct zone of non-homogenous atomic volume in the FCC-ordered planes neighboring the boundaries. For the remainder of this work, this specific area will be referred to as the near-boundary region. In Figure 5, they are indicated by light blue shading.

To explore the effect of the grain boundary structure on the near-boundary regions in MPEAs, the same volume versus plane analysis was performed on the quinary and quaternary alloys for each facet, shown in Figure 5(c-f). Each element is indicated by different colors, and the dotted lines of the same colors indicate the average bulk volume for that element. Starting with Figure 5(c) and (e), which show the data for the low energy facets in the quinary and quaternary alloys respectively, it is first notable that all elements follow the contours of the atomic volumes seen in the pure Cu facets. All per-element volumes reach their peak at Plane 0 in both alloys and have near-boundary regions with reduced atomic volumes. This trend indicates that elements respond to the structural changes introduced by the boundary in a relatively uniform manner, including in the near-boundary regions. The same appears to be generally true in the high energy facets of Figure 5(d) and (f), with some important caveats. Unlike the high energy facet of the pure Cu boundary in Figure 5(b), the volume contours of the left and right near-boundary regions are significantly different. The right side, which is in general far more structured (see e.g. Figures 1(c) and 3(b)), has its minimum volume value at Plane 3, which strongly resembles the pattern seen in the ordered low energy facets. In contrast, the near-boundary regions on the left side are more curved, reaching their minimums at approximately Plane -5 in both alloys.

The purpose of studying atomic volume was to isolate potential mechanisms behind the enrichment and depletion of Fe/Cu or Fe/Cr seen in the composition versus plane data of Figure 3. To better enable comparison between changes in atomic volume in the near-boundary region

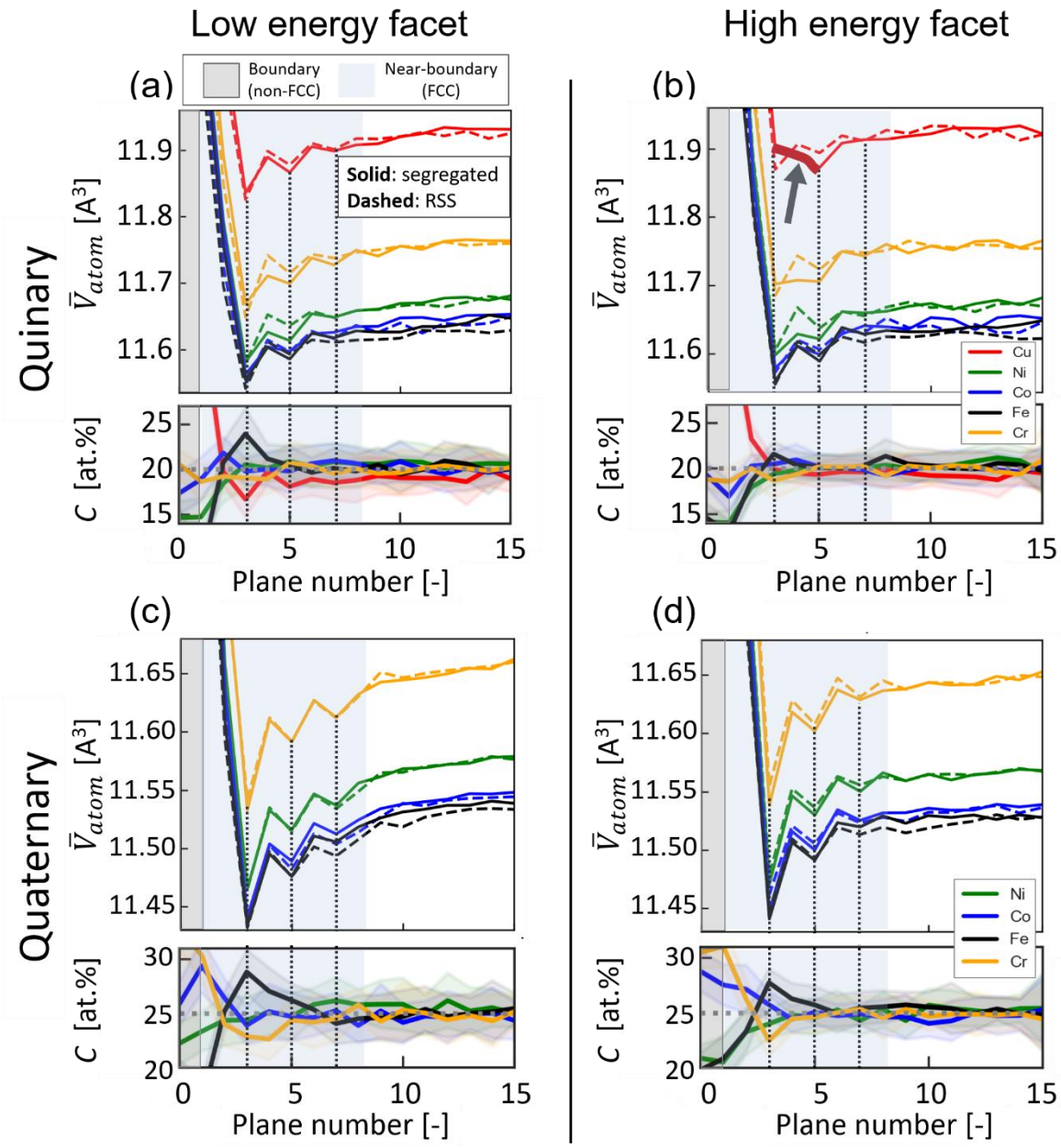

Figure 6. Magnified view of the average per-element volumes per plane in the near-boundary regions from Figure 4 at T = 1000 K. Dashed colored lines show data for the random solid solution (RSS), and solid-colored lines show trends for the segregated state. Beneath each volume-plane plot is a truncated reference to the composition-plane data from Figure 3 for each material and facet. The dotted vertical gray lines act as guidelines to compare trends in composition with those of RSS/segregated volume.

with changes in composition, magnified views of the volume contours (solid lines) of the near-boundary regions of Figure 5(c-f) are shown in Figure 6 for each facet and alloy. Because the high energy facets have higher symmetry on the right sides of their faces, those sides are also featured in Figure 6 (the shaded error bands and the dotted horizontal lines showing per-element atomic volumes from Figure 5 have been removed for clarity). Beneath each volume plot are truncated versions of the composition versus plane plots of Figure 3, with dotted black lines on Planes 3, 5, and 7 to guide the eye to points of intersection.

Plane 3 is the site of both maximum Fe enrichment and minimum average atomic volumes for three out of four cases, namely in the low energy facets of both alloys (Figures 6(a) and 6(c)) and the high energy facet of the quaternary alloy (Figure 6(d)). These enrichments extend beyond Plane 3 to Plane 5 in the low energy facet of the quinary alloy, and into approximately Plane 7 in both facets of the quaternary alloy. In contrast, the near-boundary region of high energy facet of the quinary alloy in Figure 6(b) does not follow the trends of the other three near-boundary regions. That facet has only slight enrichment of Fe (~1.7 at.%) and essentially no depletion of Cu. More strikingly, though four of the five components have their minimum values at Plane 3, Cu has its minimum volume instead at Plane 5. This means that, instead of following the same contour as all other elements and facets, which increase on average between Planes 3 and 5, the Cu volume decreases. This discrepancy is highlighted with the addition of a dark gray arrow and the thickening the red curve between Planes 3 and 5 in Figure 6(b).

The decrease in atomic volume raises a question about the evolution of segregation in this particular near-boundary region. Recall from the Methods section that, after generating the initial faceted structure in pure Cu, the RSS is created by randomizing the atom types in the Cu simulation cell. In the RSS state, the reduced volume of the near-boundary region is preserved from the pure

Cu boundary structure, but the elemental atomic volumes will be unrelaxed. MCMD is then applied to induce segregation. As shown in Figure 3 and the other subfigures of Figure 6, the atomic volumes in near-boundary regions are remarkably synchronized in terms of following the contours of volume introduced by the presence of the grain boundary. However, it is possible that the decrease in this region was present already in the high energy facet of the quinary RSS. To check for this possibility, the per-element atomic volume curves are included in each subplot of Figure 6. To distinguish them from the segregated data, which has solid lines, the RSS curves have dashed lines. The RSS data indicates that the unrelaxed state of the Cu atoms followed the same trend as the other four elements, namely with Plane 3 as the minimum. The shift to having Plane 5 as the minimum is thus a result of relaxation from MCMD.

Taken as a whole, the trends in near-boundary region described above provide one potential explanation for Fe enrichment in and beyond Plane 3, as well as the relative lack of enrichment in the high energy quinary facet of Figure 6(b). Just as the free volume available at grain boundaries encourages segregation, regions of reduced volume can also encourage anti-segregation of elements. Starting with the quinary low energy facet in Figure 6(a), Plane 3 is the site of maximum Fe enrichment, minimum Cu depletion, and minimum average atomic volume for both elements. As the element with the largest average atomic volume (as well as largest atomic radius) in this study, Cu is a likely candidate to anti-segregate from near-boundary regions, especially from the lowest-volume site at Plane 3. The departure of Cu atoms in turn increases the average amount of locally available volume. Fe is well-suited both physically (in terms of having the smallest average atomic volume) and chemically (it depletes strongly from grain boundary sites) to take up the extra atomic volume made available in Plane 3 by Cu anti-segregation. This implies that the extra Fe seen in the planes nearest each facet would be a second order effect of the departure of Cu atoms.

Importantly, this anti-segregation explanation works just as well for Cr atoms, which have the second-largest atomic volumes in the quinary alloy and the largest by far in the quaternary. This explanation is also consistent with what is observed in the high energy facet of the quinary alloy (Figure 6(b)). Its exceptionally higher average atomic volume of Cu in Plane 3 in this framework would reflect its ~4 at.% higher composition relative to Cu in the low energy facet (Figure 6(a)).

Further atomistic study of grain boundaries in MPEAs may reveal near-boundary segregation to be ubiquitous. If so, this suggests that that grain boundaries might be better modeled as more diffuse entities in MPEAs than how they are traditionally treated in chemically simpler materials. Support for this idea can be found in the models correlating segregation trends with a parameter that characterizes the degree of grain boundary disorder, utilized by Hu and Luo [139]. This disorder parameter can account for regions outside of what would traditionally be identified as the grain boundary when using methods such as Common Neighbor Analysis. Another interesting implication of near-boundary segregation is that it may provide an explanation for the origin of larger-scale phenomena, such as the strong near-boundary depletion observed in the Zhao et al. [137] study described above. It is possible that small but detectable changes in composition in the proximity of boundaries could act as chemical signals indicating potential sites of compositional transformation, such as the nanoclustering of Cr and Ni at grain boundaries observed in the Cantor alloy by Ming et al. [73].

5.3.4 Chemical short-range order

Important in the study of any single-phase MPEA is an understanding of its chemical short-range order (CSRO), a property of complex alloys that can have large impacts on material properties [67–69, 140]. For three-dimensional models in complex alloys, one commonly-used

tool is a variant on the Warren-Cowley equation [141], which counts the relative frequency α_n^{ij} of atom pairs using the nth nearest-neighbor shells of a material as follows:

$$\alpha_n^{ij} = 1 - \frac{P_n^{ij}}{c_j} \quad (2)$$

The subscript *i* refers to the center atom's element, the subscript *j* refers to an element type present in the shell of atom *i*, the subscript *n* refers to the neighbor shell of interest (here, always the 1st), the term P_n^{ij} describes the probability of finding an atom of type *j* in the shell of an atom of type *i*, and the term c_j denotes the concentration of atoms of type *j*. A value of zero corresponds to a material resembling an ideal random solid solution. Negative values indicate that pairs are more likely to be found in each other's *n*-th nearest-neighbor shell (i.e., clustering behavior), while positive values reflect a lower frequency of pairs in the same *n*-th shell (i.e., anti-clustering).

Figure 7 shows the α_1 values for the first nearest-neighbor shells for the bulk material (gray bars) and for the Σ11 boundary atoms (colored bars). The results for the quinary sample are in Figure 7(a) (top) and those for the quaternary are beneath it in Figure 7(b) (bottom). The bulk values indicate that almost all values outside the boundaries have α_1 values very close to 0 overall at 1000 K, indicating that bulk atoms do approximate a random solid solution in this system. As can be seen in the temperature vs. CSRO data included in the Supplemental Material (S4), the only exceptions to this in the bulk can be found at 200 K, where several Cu pairings have significantly larger magnitudes. In contrast, the CSRO values for the grain boundary atoms are far larger in magnitude than those of the bulk. With the exception of the quinary Cu-Cu pair (which has a mean value of -0.51), the α_1 values for atoms in the grain boundary fall within the range of -0.2 to +0.3.

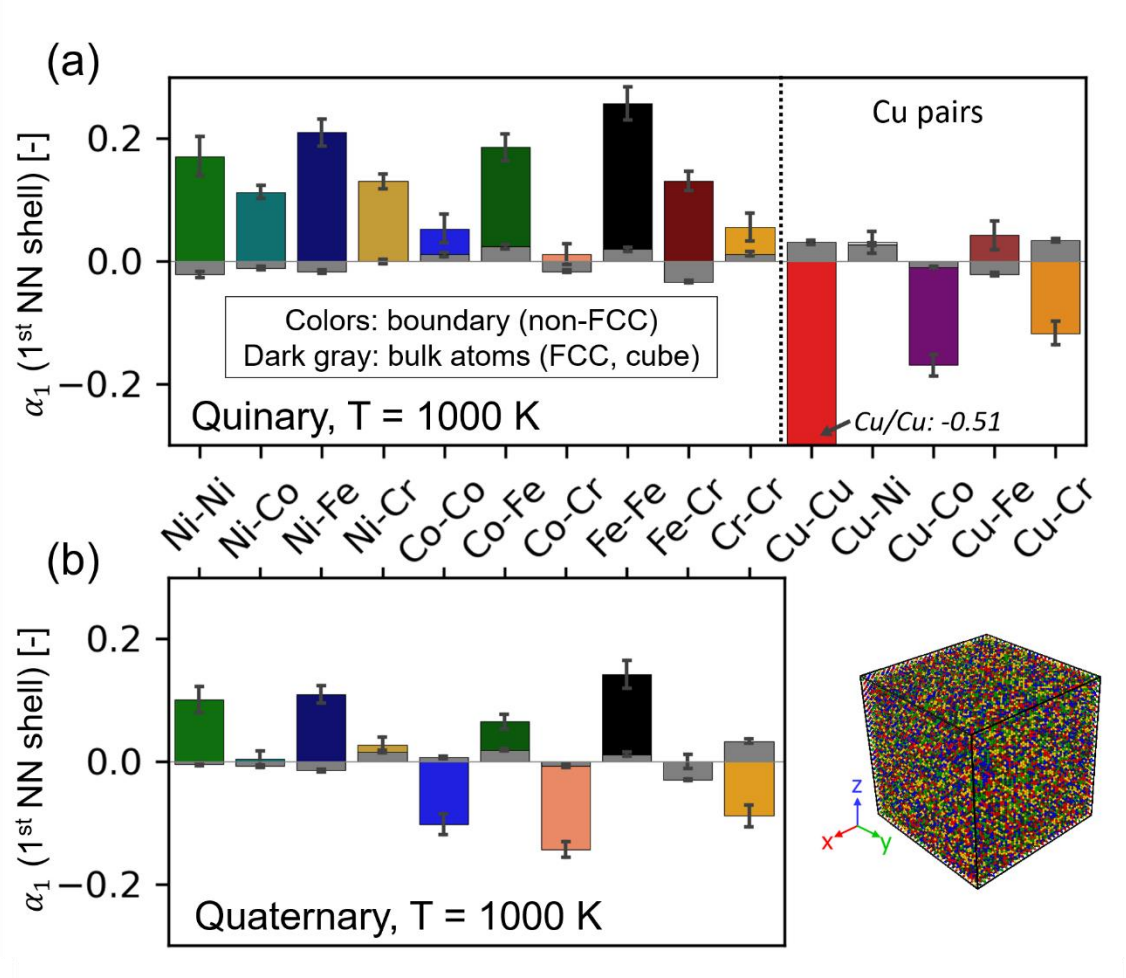

Figure 7. Results of chemical short-range order (CSRO) analysis conducted on a bulk cube (gray bars) and the grain boundary/non-FCC atoms (colored bars), showing the first nearest-neighbor α_1 values for the Warren-Cowley parameter (Equation 2). (a) Data for the quinary material. (b) Data for the quaternary material.

Though typically, larger magnitudes of CSRO might indicate chemically-induced local ordering of atoms, a closer look at the CSRO trends at the boundaries suggests that not to be the case here. Regardless of the breakdown (by grain boundary, by facet, or by plane), the changes in CSRO at the grain boundary relative to the bulk mirror quite directly the trends in grain boundary segregation. There do not appear to be any special changes in CSRO outside of those introduced by changes in composition. Elements and element pairs that are enriched at the grain boundaries have correspondingly more negative α_1 values, and those that deplete have more positive ones.

This implies that trends in CSRO are not actually chemical in nature in the two alloys under study, but are instead structural. The clearest examples of this can be seen in the quinary, where Cu, the most dominant segregating species by far, also has the most negative value of α_1 = -0.51 on average. The only other pairs that are clearly positive are Cu-Co and Cu-Cr, the second- and third-most common element retained at the boundary at T = 1000 K. Almost all other pairs are relatively strongly positive, indicating a less frequent counting of elemental pairs. In Figure 7(b), the same pattern is reflected in the quaternary pairs, where only Co and Cr pairs have significantly negative values. In both the quinary and the quaternary, Fe-Fe pairs have the most positive values, reflecting Fe's status as the most depleted element within grain boundaries. All others remain close to their bulk values or are somewhat positive. An example of the mean α_1 values per plane for the quinary low energy facet is shown in Figure 8(a-c). The data for same-element pairs in Figure 8(a) is a rough mirror image of the composition versus plane number plots from Figure 3(a) and (c), lacking the structural detail but maintaining the same (reflected) contours. The other two plots show the planar data for inter-elemental plots, showing the same trend. An example for the same facet in the quaternary alloy is shown in Figure 8(d-f).

The apparent lack of any special CSRO is not surprising, given the low enthalpies of mixing characteristic of this potential. In fact, this potential's weakness highlights an important issue to consider with respect to grain boundaries, CSRO, and MPEAs more generally. While this parameter may accurately reflect chemical ordering in structurally and compositionally homogeneous regions of material, it becomes less accurate in inhomogeneous ones. This is because, as seen in Figure 7 and 8, α_1 can become coupled with the spatial nature of composition changes. Because the enthalpies of mixing in this potential are relatively low, the relationship between calculated CSRO and boundary segregation is clear in this potential (with Cu pairs as the

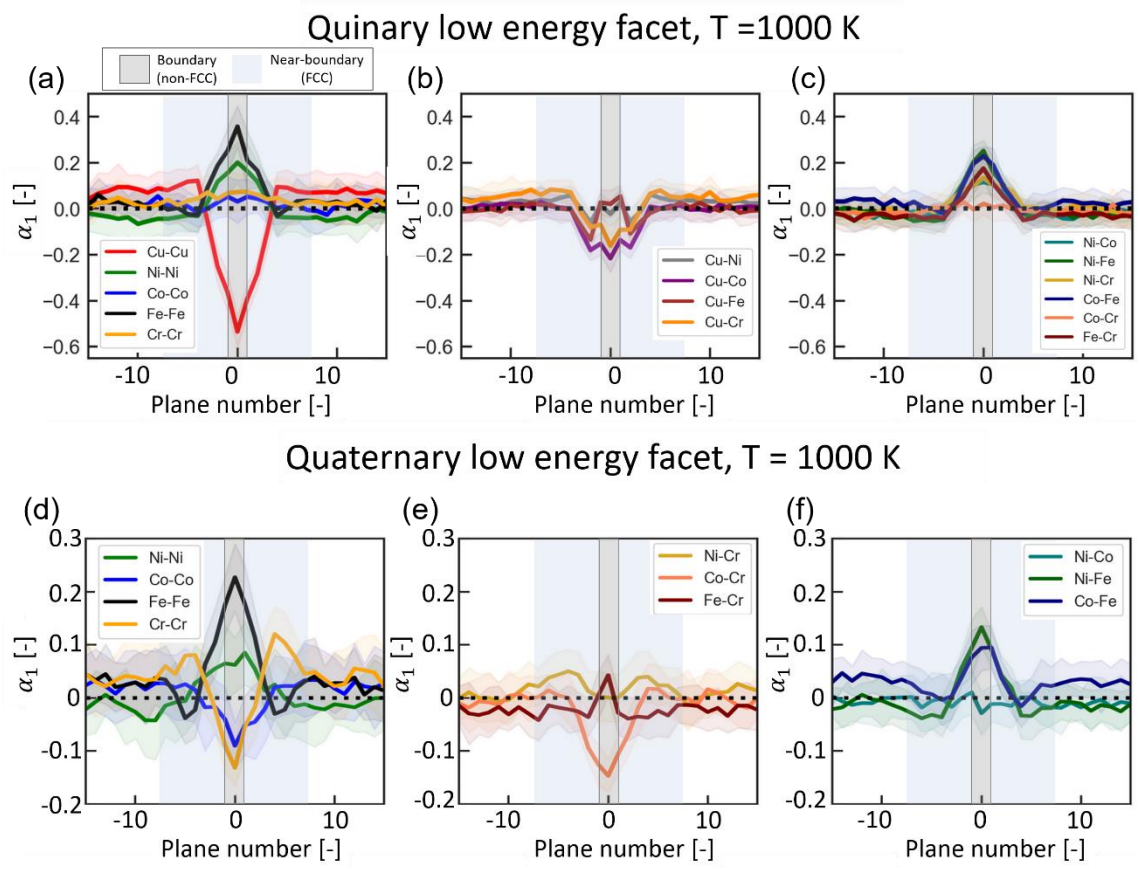

Figure 8. Analysis of CSRO trends for α_1 as a function of plane number for the low energy facet only. As in previous figures, the boundary planes (non-FCC) are indicated with a gray line, and the near-boundary regions (FCC) with blue shading. The top row shows the data for the quinary alloy, with (a) same-element pairs, (b) Cu-based pairs, and (c) all other pairs. The bottom row shows the quaternary alloy data, with (d) same-element pairs, (e) Cr-based pairs, and (f) all other pairs.

primary example). However, when using potentials with larger magnitude enthalpies of mixing, it would be very challenging to decompose α_1 into a spatial versus a chemical contribution. For this reason, the terminology used to describe CSRO in inhomogeneous regions of material may also be inaccurate. Commonly, negative values of α_1 are said to reflect inter-elemental attractions, and positive values repulsions. Again, those terms would be accurate assuming they reflect purely (or at least mostly) chemically influenced behavior. In this example, it is more accurate to say that the α_1 values may signify a higher or lower frequency of spatial occurrence, rather than attractions

or repulsions specifically. The same is true for any MPEA whose initial composition is non-equiatomic, or for MPEAs exhibiting significant phase segregation. The development of new CSRO parameters that can take these differences into account would be a powerful tool in MPEA research moving forward.

5.4 Conclusion

The analysis of the segregation patterns of a faceted Σ11 boundary in two equiatomic MPEAs (CuNiCoFeCr and NiCoFeCr) allows the following conclusions to be made:

- Segregation does not appear to alter fundamental faceted boundary characteristics such as periodicity or preferred low and high energy facet orientations, suggesting that crystallography may play a greater role in faceting behavior than the elemental composition.
- The quinary alloy is an example of an MPEA with one very strongly segregating element, namely Cu. Its segregation is driven by a reduction in strain energy relative to the bulk as well as Cu's favorable surface and vacancy energies. The low enthalpies of mixing modeled in this potential reduce the effect of mixing enthalpy on segregation, yet yield similar results to other studies where Cu has very positive mixing enthalpies with other elements. This suggests that the elastic and energetic contributions to Cu's segregation energy are equally as important.
- The quaternary alloy has two strongly segregating elements, Cr and Co. This suggests that their relative depletion in the quinary may be due to site competition with Cu. Ni and Fe are strongly depleted at the grain boundaries in both materials.

- Increasing temperature decreases overall segregation to the boundaries in both materials, consistent with higher temperatures increasing solubility in general. Some elemental enrichment and depletion are evident even at the highest temperatures studied here (90% of the melting temperature).
- Significant segregation of Fe is observed in the FCC-ordered planes adjacent to both low and high energy facets. Atomic volume analysis reveals this segregation to be correlated with a structurally distinct region of atomic volumes that are lower than the bulk. These near-boundary regions are present in pure Cu bicrystals as well, indicating that they are not unique to MPEA interfaces.
- In the near-boundary regions, sites with the lowest atomic volume correlate to Fe enrichment and Cu and Cr depletion in the quinary and quaternary alloys, respectively. The enrichment appears to be a secondary effect of depletion of Cu and Cr.
- Analysis of the chemical short-range order shows that all atom pairs in the bulk have near-random chemical ordering after MC/MD simulation. Similar analysis of grain boundaries and near-boundary regions did not reveal any special ordering that could not be attributed to elemental composition changes due to segregation. Both results reflect the low enthalpies of mixing characteristic of this potential. This indicates that near-boundary segregation is a purely structure-induced process.

The results from this study highlight an important gap in understanding segregation behavior, both in MPEAs as well as in more traditional alloy systems. Regions of crystal not traditionally identified as belonging to grain boundaries could impact microstructure evolution in ways not currently understood. Though near-boundary segregation zones may be especially

obvious in the case of chemically complex MPEAs, they may have also been playing underappreciated roles in other alloys, for example in ternary systems or even binary alloys beyond the dilute limit. In addition to providing fundamental insight into segregation behavior, such regions could in theory be utilized in the tuning of material properties.

6 Conclusions

In many ways, the faceted Σ11 boundaries are an ideal set of interfaces to study. In addition to having an interesting set of structures and defects in and of themselves (Chapter 1), the dynamic interactions between their seemingly simple C and E structural units lead to complex and unexpected migration behavior (Chapters 2 and 3). They also provide an interesting energetic backdrop from which to understand trends in segregation (Chapters 4 and 5). In these ways, these boundaries inform fundamental models of grain boundary structure, thermodynamics and kinetics, while simultaneously providing insights into topics critical to metallurgical engineering such as abnormal grain growth and anisotropic segregation. In this dissertation, our aim was to expand and deepen knowledge in this field through the analysis of migration and segregation behaviors of faceted Σ11 <110> tilt boundaries in FCC metals and alloys. Our conclusions are summarized below.

- In Chapter 2, using insights the existing literature on the static structures of faceted Σ11 boundaries, we studied the migration behavior of one faceted Σ11 boundary using two different face-centered cubic EAM potentials (Al, Cu). We discovered a new and unexpected migration mechanism in Cu that is strongly dependent on the direction of boundary migration, which we called directionally-anisotropic mobility. Through detailed analysis of the static and dynamic boundary structure, we were able to characterize the three most dominant atomistic migration mechanisms, called shuffling modes. One of these, namely slip plane shuffling, was found to be responsible for this unique mobility trend.
- Chapter 3 expanded the results of Chapter 2 from one boundary inclination angle to four, and from two interatomic potentials to six (two each of Al, Cu, and Ni). It was found that

the same shuffling modes observed in the boundaries of Chapter 2 are also active in the broader dataset of this chapter. These results allowed us to establish directionally-anisotropic mobility as a general property of faceted Σ11 boundaries in Cu and Ni, with strong correlations to temperature, stacking fault energy, boundary inclination angle, and elemental properties. A model of shuffling mode competition was proposed and successfully connected directionally-anisotropic mobility to the most general atomistic migration mechanism of disordered shuffling.

- In Chapter 4, the effect of alloying on the structure and migration of a long-period faceted Σ11 boundary was studied, with a focus on dilute Cu-Ag solutions. We first explored the segregation behavior of this boundary through different temperatures and solute concentrations. We found that Ag atoms consistently favored segregation sites within IBP facets, which have higher average atomic volumes and tensile hydrostatic atomic stresses. These results are consistent with literature indicating strongly anisotropic segregation in faceted boundaries in general. Migration studies of a low-concentration, high-temperature configuration were also performed. It was found that the addition of Ag atoms disrupts disordered shuffling, which in turn results in directionally-anisotropic mobility. These results demonstrate that this mobility phenomenon can be induced by alloying.
- Chapter 5 focused on understanding faceted Σ11 structure and segregation behavior in a pair of related multi-principal element alloys, the quinary CuNiCoFeCr and a related quaternary NiCoFeCr. It is first determined that, even with strong segregation to boundaries at lower temperatures, there are no major structural changes. An investigation of connections between temperature, relative levels of elemental segregation, and atomic volume was conducted for each facet. Though no major differences in average segregation

between facets were found in these materials, an intriguing trend of Fe enrichment in bulk regions neighboring facet planes was also uncovered. Investigation of this phenomenon revealed a further unexpected finding, namely a structurally distinct zone of reduced atomic volume between the boundary and crystal bulk regions. This special near-boundary region was found to exist in a pure system, the RSS, and both MPEAs. Distinct relationships between these regions and the unusual Fe segregation were found. The results of this chapter suggest that near-boundary segregation zones may be ubiquitous in MPEAs and further research into this phenomenon is warranted.

Taken as a whole, the results of this dissertation further demonstrate the utility of studying faceted grain boundaries. It is remarkable that the choice of a single subset of these interfaces can yield such a rich variety of practical and scientific insights.

7 Future Work

Through the lens of the unique Σ11 faceted boundaries, this dissertation advances the field's understanding of faceted boundary migration and segregation in a variety of different contexts. The results presented here also present opportunities for further research:

- *Fundamental kinetic descriptions of shuffling modes:* The results in this study provide a broad overview of the primary migration mechanisms in these boundaries and an exploration of their expression through a range of different materials. However, a thorough characterization of the fundamental kinetics of each shuffling mode is lacking. Such a description would connect the results of this dissertation to more general models of boundary motion and grain growth. It could also provide an explanation for other interesting phenomenon, such as the grain growth-generated Lomer-Cotrell locks observed in Chapter 4.3.2. The experimental evidence of Shockley shuffling by Bowers et al. [23] provides a good starting point for studies of the IBP alone, or the IBP facet. Additionally, analysis of shuffling modes through the framework of grain boundary disconnection modes proposed by Han, Thomas, and Srolovitz [42] could be highly effective in elucidating the physical origins of directionally-anisotropic mobility, potentially enabling a prediction of this property in special or even general grain boundaries.
- *Experimental validation of slip plane shuffling and directionally-anisotropic mobility:* Our results combined with other studies of stacking fault emission [10, 81, 84, 142], most notably the experimental work of Bowers et al. [23], strongly suggest that Shockley shuffling and disordered shuffling could also be observed occurring in physical samples of migrating Σ11 boundaries. However, there is not yet experimental evidence of slip plane shuffling, the mode found to be responsible for directionally-anisotropic mobility in this

work. MD and TEM results are often in strong agreement structurally, suggesting that the mechanism itself could be observed physically. Whether it would have as strong an impact on overall mobility as it does in simulations is an open question.

- *The effect of boundaries exhibiting directionally-anisotropic mobility on grain boundary network evolution:* The mechanisms behind directionally-anisotropic mobility are extremely local, operating on the individual IBP facet level. Collectively, local anisotropies also results in divergent mobility values within the bicrystal studies conducted here. However, it is unclear whether or how directionally-anisotropic mobility would affect the evolution of a grain boundary network. To investigate, we propose the use of non-atomistic grain growth, with a focus on topological modeling [143–145].
- *Incorporation of boundary mobility as a design variable, tunable by alloying:* Chapter 4 demonstrated the viability of controlling mobility trends in boundary through the addition of a low concentration of dopant atoms. In this specific case, it was the induction of directionally-anisotropic mobility through alloying, which could have some interesting potential applications. A very theoretical example would be using the boundary in Chapter 4 to move the boundary increments at a time. Since the faceted Σ11 is self-locking in one direction, one has considerable control over its position. Once a desired grain boundary position is reached, additional dopants could be added to pin it in place. The existence of this alloying-induced mobility trend is intriguing because it opens the possibility of sophisticated means of controlling boundary migration beyond simple pinning.
- *Exploration of near-boundary segregation phenomena in multi-principal element alloys:* Further atomistic study of grain boundaries in MPEAs may reveal near-boundary segregation to be ubiquitous. Near-boundary segregation suggests that that grain

boundaries at the atomic scale might be better modeled as more diffuse entities in HEAs than how they are traditionally treated in chemically simpler materials. It is possible that small but detectable changes in composition in the proximity of boundaries could act as chemical signals indicating potential sites of compositional transformation, such as complexion transitions or precipitate formation.

References

[1] E. R. Homer, E. A. Holm, S. M. Foiles, and D. L. Olmsted, *Trends in Grain Boundary Mobility: Survey of Motion Mechanisms*, JOM **66**, 114 (2014).

[2] D. Farkas and A. Caro, *Model Interatomic Potentials and Lattice Strain in a High-Entropy Alloy*, J. Mater. Res. **33**, 3218 (2018).

[3] G. S. Rohrer, *Grain Boundary Energy Anisotropy: A Review*, J. Mater. Sci. **46**, 5881 (2011).

[4] J. Humberson, I. Chesser, and E. A. Holm, *Contrasting Thermal Behaviors in Σ3 Grain Boundary Motion in Nickel*, Acta Mater. **175**, 55 (2019).

[5] K. L. Merkle, *Atomic Structure of Grain Boundaries*, J. Phys. Chem. Solids **55**, 991 (1994).

[6] K. L. Merkle, L. J. Thompson, and F. Phillipp, *In-Situ HREM Studies of Grain Boundary Migration*, Interface Sci. **12**, 277 (2004).

[7] A. P. Sutton and R. W. Balluffi, *Interfaces in Crystalline Materials* (OUP Oxford, 2006).

[8] G. Gottstein and L. S. Shvindlerman, *Grain Boundary Migration in Metals: Thermodynamics, Kinetics, Applications* (CRC press, 2009).

[9] L. Priester, *Grain Boundaries: From Theory to Engineering* (Springer Netherlands, 2013).

[10] M. A. Tschopp, G. J. Tucker, and D. L. McDowell, *Structure and Free Volume of ⟨110⟩ Symmetric Tilt Grain Boundaries with the E Structural Unit*, Acta Mater. **55**, 3959 (2007).

[11] M. A. Tschopp and D. L. McDowell, *Structural Unit and Faceting Description of Σ3 Asymmetric Tilt Grain Boundaries*, J. Mater. Sci. **42**, 7806 (2007).

[12] J. Han, V. Vitek, and D. J. Srolovitz, *The Grain-Boundary Structural Unit Model Redux*, Acta Mater. **133**, 186 (2017).

[13] V. Randle, *Role of Grain Boundary Plane in Grain Boundary Engineering*, Mater. Sci. Technol. **26**, 774 (2010).

[14] U. Wolf, F. Ernst, T. Muschik, M. W. Finnis, and H. F. Fischmeister, *The Influence of Grain Boundary Inclination on the Structure and Energy of σ = 3 Grain Boundaries in Copper*, Philos. Mag. A **66**, 991 (1992).

[15] M. A. Tschopp and D. L. Mcdowell, *Asymmetric Tilt Grain Boundary Structure and Energy in Copper and Aluminium*, Philos. Mag. **87**, 3871 (2007).

[16] D. L. Olmsted, S. M. Foiles, and E. A. Holm, *Survey of Computed Grain Boundary Properties in Face-Centered Cubic Metals: I. Grain Boundary Energy*, Acta Mater. **57**, 3694 (2009).

[17] E. R. Homer, S. Patala, and J. L. Priedeman, *Grain Boundary Plane Orientation Fundamental Zones and Structure-Property Relationships*, Sci. Rep. **5**, 1 (2015).

[18] F. Abdeljawad, S. M. Foiles, A. P. Moore, A. R. Hinkle, C. M. Barr, N. M. Heckman, K. Hattar, and B. L. Boyce, *The Role of the Interface Stiffness Tensor on Grain Boundary Dynamics*, Acta Mater. **158**, 440 (2018).

[19] J. Li, S. J. Dillon, and G. S. Rohrer, *Relative Grain Boundary Area and Energy Distributions in Nickel*, Acta Mater. **57**, 4304 (2009).

[20] H. Beladi, A. Ghaderi, and G. S. Rohrer, *Five-Parameter Grain Boundary Characterisation of Randomly Textured AZ31 Mg Alloy*, Philos. Mag. **100**, 456 (2020).

[21] A. H. King and S. Shekhar, *What Does It Mean to Be Special? The Significance and Application of the Brandon Criterion*, J. Mater. Sci. **41**, 7675 (2006).

[22] K. L. Merkle and D. Wolf, *Quasiperiodic Features in the Atomic Structure of Long-Period Grain Boundaries*, Mater. Lett. **17**, 217 (1993).

[23] M. L. Bowers, C. Ophus, A. Gautam, F. Lançon, and U. Dahmen, *Step Coalescence by Collective Motion at an Incommensurate Grain Boundary*, Phys. Rev. Lett. **116**, 106102 (2016).
[24] T. Radetic, F. Lançon, and U. Dahmen, *Chevron Defect at the Intersection of Grain Boundaries with Free Surfaces in Au*, Phys. Rev. Lett. **89**, 085502 (2002).
[25] A. Gautam, C. Ophus, F. Lançon, V. Radmilovic, and U. Dahmen, *Atomic Structure Characterization of an Incommensurate Grain Boundary*, Acta Mater. **61**, 5078 (2013).
[26] B. Kuhr and D. Farkas, *Dislocation Content in Random High Angle Grain Boundaries*, Model. Simul. Mater. Sci. Eng. **27**, 045005 (2019).
[27] S. T. Chui, *Grain Boundary Roughening Transitions*, EPL Europhys. Lett. **87**, 66001 (2009).
[28] D. L. Olmsted, S. M. Foiles, and E. A. Holm, *Grain Boundary Interface Roughening Transition and Its Effect on Grain Boundary Mobility for Non-Faceting Boundaries*, Scr. Mater. **57**, 1161 (2007).
[29] T. E. Hsieh and R. W. Balluffi, *Observations of Roughening/de-Faceting Phase Transitions in Grain Boundaries*, Acta Metall. **37**, 2133 (1989).
[30] S. B. Lee, D. Y. Yoon, N. M. Hwang, and M. F. Henry, *Grain Boundary Faceting and Abnormal Grain Growth in Nickel*, Metall. Mater. Trans. A **31**, 985 (2000).
[31] S. B. Lee, W. Sigle, and M. Rühle, *Faceting Behavior of an Asymmetric SrTiO3 Σ5 [001] Tilt Grain Boundary Close to Its Defaceting Transition*, Acta Mater. **51**, 4583 (2003).
[32] D. L. Medlin, K. Hattar, J. A. Zimmerman, F. Abdeljawad, and S. M. Foiles, *Defect Character at Grain Boundary Facet Junctions: Analysis of an Asymmetric Σ = 5 Grain Boundary in Fe*, Acta Mater. **124**, 383 (2017).
[33] J. C. Hamilton, D. J. Siegel, I. Daruka, and F. Léonard, *Why Do Grain Boundaries Exhibit Finite Facet Lengths?*, Phys. Rev. Lett. **90**, 246102 (2003).
[34] Z. X. Wu, Y. W. Zhang, and D. J. Srolovitz, *Grain Boundary Finite Length Faceting*, Acta Mater. **57**, 4278 (2009).
[35] R. Hadian, B. Grabowski, M. W. Finnis, and J. Neugebauer, *Migration Mechanisms of a Faceted Grain Boundary*, Phys. Rev. Mater. **2**, 043601 (2018).
[36] F. Abdeljawad, D. L. Medlin, J. A. Zimmerman, K. Hattar, and S. M. Foiles, *A Diffuse Interface Model of Grain Boundary Faceting*, J. Appl. Phys. **119**, 235306 (2016).
[37] B. B. Straumal, S. A. Polyakov, and E. J. Mittemeijer, *Temperature Influence on the Faceting of Σ3 and Σ9 Grain Boundaries in Cu*, Acta Mater. **54**, 167 (2006).
[38] B. B. Straumal, A. S. Gornakova, and V. G. Sursaeva, *Reversible Transformation of a Grain-Boundary Facet into a Rough-to-Rough Ridge in Zinc*, Philos. Mag. Lett. **88**, 27 (2008).
[39] B. B. Straumal, O. A. Kogtenkova, A. S. Gornakova, V. G. Sursaeva, and B. Baretzky, *Review: Grain Boundary Faceting–Roughening Phenomena*, J. Mater. Sci. **51**, 382 (2016).
[40] I. Daruka and J. C. Hamilton, *Atomistic and Lattice Model of a Grain Boundary Defaceting Phase Transition*, Phys. Rev. Lett. **92**, 246105 (2004).
[41] P. R. Cantwell, T. Frolov, T. J. Rupert, A. R. Krause, C. J. Marvel, G. S. Rohrer, J. M. Rickman, and M. P. Harmer, *Grain Boundary Complexion Transitions*, Annu. Rev. Mater. Res. **50**, 465 (2020).
[42] J. Han, S. L. Thomas, and D. J. Srolovitz, *Grain-Boundary Kinetics: A Unified Approach*, Prog. Mater. Sci. **98**, 386 (2018).

[43] C. Günster, D. A. Molodov, and G. Gottstein, *Migration of Grain Boundaries in Zn*, Acta Mater. **61**, 2363 (2013).
[44] J. Humberson and E. A. Holm, *Anti-Thermal Mobility in the Σ3 [111] 60° {11 8 5} Grain Boundary in Nickel: Mechanism and Computational Considerations*, Scr. Mater. **130**, 1 (2017).
[45] S.-M. An, B.-K. Yoon, S.-Y. Chung, and S.-J. L. Kang, *Nonlinear Driving Force–Velocity Relationship for the Migration of Faceted Boundaries*, Acta Mater. **60**, 4531 (2012).
[46] V. G. Sursaeva, B. B. Straumal, A. S. Gornakova, L. S. Shvindlerman, and G. Gottstein, *Effect of Faceting on Grain Boundary Motion in Zn*, Acta Mater. **56**, 2728 (2008).
[47] V. G. Sursaeva and S. I. Prokofiev, *Faceting of a Moving Grain Boundary and Its Effect on the Kinetic Properties of Grain Boundaries*, Bull. Russ. Acad. Sci. Phys. **81**, 1370 (2017).
[48] J. L. Bair and E. R. Homer, *Antithermal Mobility in Σ7 and Σ9 Grain Boundaries Caused by Stick-Slip Stagnation of Ordered Atomic Motions about Coincidence Site Lattice Atoms*, Acta Mater. **162**, 10 (2019).
[49] P. R. Cantwell, E. A. Holm, M. P. Harmer, and M. J. Hoffmann, *Anti-Thermal Behavior of Materials*, Scr. Mater. **103**, 1 (2015).
[50] M. Wagih and C. A. Schuh, *Spectrum of Grain Boundary Segregation Energies in a Polycrystal*, Acta Mater. **181**, 228 (2019).
[51] H. Zhao, L. Huber, W. Lu, N. J. Peter, D. An, F. De Geuser, G. Dehm, D. Ponge, J. Neugebauer, B. Gault, and D. Raabe, *Interplay of Chemistry and Faceting at Grain Boundaries in a Model Al Alloy*, Phys. Rev. Lett. **124**, 106102 (2020).
[52] C. J. O'Brien and S. M. Foiles, *Hydrogen Segregation to Inclined Twin Grain Boundaries in Nickel*, Philos. Mag. **96**, 2808 (2016).
[53] C. H. Liebscher, A. Stoffers, M. Alam, L. Lymperakis, O. Cojocaru-Mirédin, B. Gault, J. Neugebauer, G. Dehm, C. Scheu, and D. Raabe, *Strain-Induced Asymmetric Line Segregation at Faceted Si Grain Boundaries*, Phys. Rev. Lett. **121**, 015702 (2018).
[54] J. L. Priedeman and G. B. Thompson, *The Influence of Alloying in Stabilizing a Faceted Grain Boundary Structure*, Acta Mater. **201**, 329 (2020).
[55] N. J. Peter, T. Frolov, M. J. Duarte, R. Hadian, C. Ophus, C. Kirchlechner, C. H. Liebscher, and G. Dehm, *Segregation-Induced Nanofaceting Transition at an Asymmetric Tilt Grain Boundary in Copper*, Phys. Rev. Lett. **121**, 255502 (2018).
[56] Z. Yu, P. R. Cantwell, Q. Gao, D. Yin, Y. Zhang, N. Zhou, G. S. Rohrer, M. Widom, J. Luo, and M. P. Harmer, *Segregation-Induced Ordered Superstructures at General Grain Boundaries in a Nickel-Bismuth Alloy*, Science **358**, 97 (2017).
[57] D. Raabe, M. Herbig, S. Sandlöbes, Y. Li, D. Tytko, M. Kuzmina, D. Ponge, and P.-P. Choi, *Grain Boundary Segregation Engineering in Metallic Alloys: A Pathway to the Design of Interfaces*, Curr. Opin. Solid State Mater. Sci. **18**, 253 (2014).
[58] B. Gludovatz, A. Hohenwarter, D. Catoor, E. H. Chang, E. P. George, and R. O. Ritchie, *A Fracture-Resistant High-Entropy Alloy for Cryogenic Applications*, Science **345**, 1153 (2014).
[59] B. Gludovatz, A. Hohenwarter, K. V. S. Thurston, H. Bei, Z. Wu, E. P. George, and R. O. Ritchie, *Exceptional Damage-Tolerance of a Medium-Entropy Alloy CrCoNi at Cryogenic Temperatures*, Nat. Commun. **7**, 1 (2016).
[60] D. B. Miracle, *High Entropy Alloys as a Bold Step Forward in Alloy Development*, Nat. Commun. **10**, 1 (2019).

[61] E. P. George, D. Raabe, and R. O. Ritchie, *High-Entropy Alloys*, Nat. Rev. Mater. **4**, 8 (2019).
[62] F. Wang, G. H. Balbus, S. Xu, Y. Su, J. Shin, P. F. Rottmann, K. E. Knipling, J.-C. Stinville, L. H. Mills, O. N. Senkov, I. J. Beyerlein, T. M. Pollock, and D. S. Gianola, *Multiplicity of Dislocation Pathways in a Refractory Multiprincipal Element Alloy*, Science **370**, 95 (2020).
[63] R. Pasianot and D. Farkas, *Atomistic Modeling of Dislocations in a Random Quinary High-Entropy Alloy*, Comput. Mater. Sci. **173**, 109366 (2020).
[64] D. Utt, S. Lee, A. Stukowski, S. H. Oh, G. Dehm, and K. Albe, *Jerky Motion of Dislocations in High-Entropy Alloys: The Linkage between Local Peierls Stress Fluctuations and Dislocation Mobility*, ArXiv200711489 Cond-Mat Physicsphysics (2020).
[65] Q.-J. Li, H. Sheng, and E. Ma, *Strengthening in Multi-Principal Element Alloys with Local-Chemical-Order Roughened Dislocation Pathways*, Nat. Commun. **10**, 1 (2019).
[66] E.-W. Huang, H.-S. Chou, K. N. Tu, W.-S. Hung, T.-N. Lam, C.-W. Tsai, C.-Y. Chiang, B.-H. Lin, A.-C. Yeh, S.-H. Chang, Y.-J. Chang, J.-J. Yang, X.-Y. Li, C.-S. Ku, K. An, Y.-W. Chang, and Y.-L. Jao, *Element Effects on High-Entropy Alloy Vacancy and Heterogeneous Lattice Distortion Subjected to Quasi-Equilibrium Heating*, Sci. Rep. **9**, 1 (2019).
[67] R. Zhang, S. Zhao, J. Ding, Y. Chong, T. Jia, C. Ophus, M. Asta, R. O. Ritchie, and A. M. Minor, *Short-Range Order and Its Impact on the CrCoNi Medium-Entropy Alloy*, Nature **581**, 7808 (2020).
[68] E. Antillon, C. Woodward, S. I. Rao, B. Akdim, and T. A. Parthasarathy, *Chemical Short Range Order Strengthening in a Model FCC High Entropy Alloy*, Acta Mater. **190**, 29 (2020).
[69] C. Tang and C. H. Wong, *Formation of Chemical Short Range Order and Its Influences on the Dynamic/Mechanical Heterogeneity in Amorphous Zr–Cu–Ag Alloys: A Molecular Dynamics Study*, Intermetallics **70**, 61 (2016).
[70] M. A. Cusentino, M. A. Wood, and R. Dingreville, *Compositional and Structural Origins of Radiation Damage Mitigation in High-Entropy Alloys*, J. Appl. Phys. **128**, 125904 (2020).
[71] L. Koch, F. Granberg, T. Brink, D. Utt, K. Albe, F. Djurabekova, and K. Nordlund, *Local Segregation versus Irradiation Effects in High-Entropy Alloys: Steady-State Conditions in a Driven System*, J. Appl. Phys. **122**, 105106 (2017).
[72] C. M. Barr, J. E. Nathaniel, K. A. Unocic, J. Liu, Y. Zhang, Y. Wang, and M. L. Taheri, *Exploring Radiation Induced Segregation Mechanisms at Grain Boundaries in Equiatomic CoCrFeNiMn High Entropy Alloy under Heavy Ion Irradiation*, Scr. Mater. **156**, 80 (2018).
[73] K. Ming, L. Li, Z. Li, X. Bi, and J. Wang, *Grain Boundary Decohesion by Nanoclustering Ni and Cr Separately in CrMnFeCoNi High-Entropy Alloys*, Sci. Adv. **5**, eaay0639 (2019).
[74] P. Wynblatt and D. Chatain, *Modeling Grain Boundary and Surface Segregation in Multicomponent High-Entropy Alloys*, Phys. Rev. Mater. **3**, 054004 (2019).
[75] L. Li, R. D. Kamachali, Z. Li, and Z. Zhang, *Grain Boundary Energy Effect on Grain Boundary Segregation in an Equiatomic High-Entropy Alloy*, Phys. Rev. Mater. **4**, 053603 (2020).
[76] L. Li, Z. Li, A. Kwiatkowski da Silva, Z. Peng, H. Zhao, B. Gault, and D. Raabe, *Segregation-Driven Grain Boundary Spinodal Decomposition as a Pathway for Phase Nucleation in a High-Entropy Alloy*, Acta Mater. **178**, 1 (2019).

[77] P. Wynblatt and R. C. Ku, *Surface Energy and Solute Strain Energy Effects in Surface Segregation*, Surf. Sci. **65**, 511 (1977).
[78] J. A. Brown and Y. Mishin, *Dissociation and Faceting of Asymmetrical Tilt Grain Boundaries: Molecular Dynamics Simulations of Copper*, Phys. Rev. B **76**, 134118 (2007).
[79] L. Zhang, C. Lu, K. Tieu, G. Michal, J. Zhang, and G. Deng, *Tension/Compression Asymmetry of Grain Boundaries with Non-Planar Structure*, Mater. Res. Express **3**, 085025 (2016).
[80] L. Smith and D. Farkas, *Non-Planar Grain Boundary Structures in Fcc Metals and Their Role in Nano-Scale Deformation Mechanisms*, Philos. Mag. **94**, 152 (2014).
[81] J. D. Rittner, D. N. Seidman, and K. L. Merkle, *Grain-Boundary Dissociation by the Emission of Stacking Faults*, Phys. Rev. B **53**, R4241 (1996).
[82] D. L. Medlin, S. M. Foiles, and D. Cohen, *A Dislocation-Based Description of Grain Boundary Dissociation: Application to a 90° 〈110〉 Tilt Boundary in Gold*, Acta Mater. **49**, 3689 (2001).
[83] R. G. Hoagland and S. M. Valone, *Emission of Dislocations from Grain Boundaries by Grain Boundary Dissociation*, Philos. Mag. **95**, 112 (2015).
[84] J. D. Rittner and D. N. Seidman, *〈110〉 Symmetric Tilt Grain-Boundary Structures in Fcc Metals with Low Stacking-Fault Energies*, Phys. Rev. B **54**, 6999 (1996).
[85] M. A. Tschopp, S. P. Coleman, and D. L. McDowell, *Symmetric and Asymmetric Tilt Grain Boundary Structure and Energy in Cu and Al (and Transferability to Other Fcc Metals)*, Integrating Mater. Manuf. Innov. **4**, 176 (2015).
[86] K. L. Merkle and D. Wolf, *Low-Energy Configurations of Symmetric and Asymmetric Tilt Grain Boundaries*, Philos. Mag. A **65**, 513 (1992).
[87] O. H. Duparc, S. Poulat, A. Larere, J. Thibault, and L. Priester, *High-Resolution Transmission Electron Microscopy Observations and Atomic Simulations of the Structures of Exact and near Σ = 11, 332 Tilt Grain Boundaries in Nickel*, Philos. Mag. A **80**, 853 (2000).
[88] G. J. Tucker, M. A. Tschopp, and D. L. McDowell, *Evolution of Structure and Free Volume in Symmetric Tilt Grain Boundaries during Dislocation Nucleation*, Acta Mater. **58**, 6464 (2010).
[89] J. F. Panzarino, Z. Pan, and T. J. Rupert, *Plasticity-Induced Restructuring of a Nanocrystalline Grain Boundary Network*, Acta Mater. **120**, 1 (2016).
[90] H. Zhang, M. Upmanyu, and D. J. Srolovitz, *Curvature Driven Grain Boundary Migration in Aluminum: Molecular Dynamics Simulations*, Acta Mater. **53**, 79 (2005).
[91] M. Upmanyu, R. W. Smith, and D. J. Srolovitz, *Atomistic Simulation of Curvature Driven Grain Boundary Migration*, Interface Sci. **6**, 41 (1998).
[92] D. L. Olmsted, E. A. Holm, and S. M. Foiles, *Survey of Computed Grain Boundary Properties in Face-Centered Cubic Metals—II: Grain Boundary Mobility*, Acta Mater. **57**, 3704 (2009).
[93] M. I. Mendelev, C. Deng, C. A. Schuh, and D. J. Srolovitz, *Comparison of Molecular Dynamics Simulation Methods for the Study of Grain Boundary Migration*, Model. Simul. Mater. Sci. Eng. **21**, 045017 (2013).
[94] K. G. F. Janssens, D. Olmsted, E. A. Holm, S. M. Foiles, S. J. Plimpton, and P. M. Derlet, *Computing the Mobility of Grain Boundaries*, Nat. Mater. **5**, 2 (2006).

[95] F. Ulomek, C. J. O\textquotesingleBrien, S. M. Foiles, and V. Mohles, *Energy Conserving Orientational Force for Determining Grain Boundary Mobility*, Model. Simul. Mater. Sci. Eng. **23**, 025007 (2015).
[96] A. Stukowski, *Visualization and Analysis of Atomistic Simulation Data with OVITO–the Open Visualization Tool*, Model. Simul. Mater. Sci. Eng. **18**, 015012 (2009).
[97] A. Stukowski, *Structure Identification Methods for Atomistic Simulations of Crystalline Materials*, Model. Simul. Mater. Sci. Eng. **20**, 045021 (2012).
[98] C. H. Rycroft, *VORO++: A Three-Dimensional Voronoi Cell Library in C++*, Chaos Interdiscip. J. Nonlinear Sci. **19**, 041111 (2009).
[99] Y. Mishin, D. Farkas, M. J. Mehl, and D. A. Papaconstantopoulos, *Interatomic Potentials for Monoatomic Metals from Experimental Data and Ab Initio Calculations*, Phys. Rev. B **59**, 3393 (1999).
[100] Y. Mishin, M. J. Mehl, D. A. Papaconstantopoulos, A. F. Voter, and J. D. Kress, *Structural Stability and Lattice Defects in Copper: Ab Initio, Tight-Binding, and Embedded-Atom Calculations*, Phys. Rev. B **63**, 224106 (2001).
[101] L. G. Wang, A. van de Walle, and D. Alfè, *Melting Temperature of Tungsten from Two Ab Initio Approaches*, Phys. Rev. B **84**, 092102 (2011).
[102] S. Plimpton, *Fast Parallel Algorithms for Short-Range Molecular Dynamics*, J. Comput. Phys. **117**, 1 (1995).
[103] R. Hadian, B. Grabowski, C. P. Race, and J. Neugebauer, *Atomistic Migration Mechanisms of Atomically Flat, Stepped, and Kinked Grain Boundaries*, Phys. Rev. B **94**, 165413 (2016).
[104] Y. Deng and C. Deng, *Size and Rate Dependent Grain Boundary Motion Mediated by Disconnection Nucleation*, Acta Mater. **131**, 400 (2017).
[105] C. P. Race, J. von Pezold, and J. Neugebauer, *Role of the Mesoscale in Migration Kinetics of Flat Grain Boundaries*, Phys. Rev. B **89**, 214110 (2014).
[106] C. P. Race, R. Hadian, J. von Pezold, B. Grabowski, and J. Neugebauer, *Mechanisms and Kinetics of the Migration of Grain Boundaries Containing Extended Defects*, Phys. Rev. B **92**, 174115 (2015).
[107] J. Wang, N. Li, and A. Misra, *Structure and Stability of Σ3 Grain Boundaries in Face Centered Cubic Metals*, Philos. Mag. **93**, 315 (2013).
[108] L. Zhang, C. Lu, and K. Tieu, *Atomistic Simulation of Tensile Deformation Behavior of ∑5 Tilt Grain Boundaries in Copper Bicrystal*, Sci. Rep. **4**, 1 (2014).
[109] A. Stukowski, V. V. Bulatov, and A. Arsenlis, *Automated Identification and Indexing of Dislocations in Crystal Interfaces*, Model. Simul. Mater. Sci. Eng. **20**, 085007 (2012).
[110] F. Sansoz and J. F. Molinari, *Mechanical Behavior of Σ Tilt Grain Boundaries in Nanoscale Cu and Al: A Quasicontinuum Study*, Acta Mater. **53**, 1931 (2005).
[111] J. L. Priedeman, D. L. Olmsted, and E. R. Homer, *The Role of Crystallography and the Mechanisms Associated with Migration of Incoherent Twin Grain Boundaries*, Acta Mater. **131**, 553 (2017).
[112] C. J. O'Brien and S. M. Foiles, *Exploration of the Mechanisms of Temperature-Dependent Grain Boundary Mobility: Search for the Common Origin of Ultrafast Grain Boundary Motion*, J. Mater. Sci. **51**, 6607 (2016).
[113] H. W. Sheng, M. J. Kramer, A. Cadien, T. Fujita, and M. W. Chen, *Highly Optimized Embedded-Atom-Method Potentials for Fourteen Fcc Metals*, Phys. Rev. B **83**, 134118 (2011).

[114] V. Borovikov, M. I. Mendelev, A. H. King, and R. LeSar, *Effect of Stacking Fault Energy on Mechanism of Plastic Deformation in Nanotwinned FCC Metals*, Model. Simul. Mater. Sci. Eng. **23**, 055003 (2015).
[115] Y. Zhang, R. Ashcraft, M. i. Mendelev, C. Z. Wang, and K. F. Kelton, *Experimental and Molecular Dynamics Simulation Study of Structure of Liquid and Amorphous Ni62Nb38 Alloy*, J. Chem. Phys. **145**, 204505 (2016).
[116] A. Stukowski, *Computational Analysis Methods in Atomistic Modeling of Crystals*, JOM **66**, 399 (2014).
[117] P. L. Williams, Y. Mishin, and J. C. Hamilton, *An Embedded-Atom Potential for the Cu–Ag System*, Model. Simul. Mater. Sci. Eng. **14**, 817 (2006).
[118] T. Frolov, S. V. Divinski, M. Asta, and Y. Mishin, *Effect of Interface Phase Transformations on Diffusion and Segregation in High-Angle Grain Boundaries*, Phys. Rev. Lett. **110**, 255502 (2013).
[119] T. Frolov, M. Asta, and Y. Mishin, *Segregation-Induced Phase Transformations in Grain Boundaries*, Phys. Rev. B **92**, 020103 (2015).
[120] H. A. Murdoch and C. A. Schuh, *Estimation of Grain Boundary Segregation Enthalpy and Its Role in Stable Nanocrystalline Alloy Design*, J. Mater. Res. **28**, 2154 (2013).
[121] M. J. McCarthy and T. J. Rupert, *Shuffling Mode Competition Leads to Directionally Anisotropic Mobility of Faceted Σ11 Boundaries in Fcc Metals*, Phys. Rev. Mater. **4**, 113402 (2020).
[122] B. Sadigh, P. Erhart, A. Stukowski, A. Caro, E. Martinez, and L. Zepeda-Ruiz, *Scalable Parallel Monte Carlo Algorithm for Atomistic Simulations of Precipitation in Alloys*, Phys. Rev. B **85**, 184203 (2012).
[123] P. Wynblatt and D. Chatain, *Anisotropy of Segregation at Grain Boundaries and Surfaces*, Metall. Mater. Trans. A **37**, 2595 (2006).
[124] M. Wagih and C. A. Schuh, *Grain Boundary Segregation beyond the Dilute Limit: Separating the Two Contributions of Site Spectrality and Solute Interactions*, Acta Mater. **199**, 63 (2020).
[125] H. Zhang and D. J. Srolovitz, *Simulation and Analysis of the Migration Mechanism of Σ5 Tilt Grain Boundaries in an Fcc Metal*, Acta Mater. **54**, 623 (2006).
[126] H. Zhang, D. J. Srolovitz, J. F. Douglas, and J. A. Warren, *Characterization of Atomic Motion Governing Grain Boundary Migration*, Phys. Rev. B **74**, 115404 (2006).
[127] D. Utt, A. Stukowski, and K. Albe, *Grain Boundary Structure and Mobility in High-Entropy Alloys: A Comparative Molecular Dynamics Study on a Σ11 Symmetrical Tilt Grain Boundary in Face-Centered Cubic CuNiCoFe*, Acta Mater. **186**, 11 (2020).
[128] D. Farkas, *Grain Boundary Structure in High-Entropy Alloys*, J. Mater. Sci. **55**, 9173 (2020).
[129] M. A. Atwater and K. A. Darling, *A Visual Library of Stability in Binary Metallic Systems: The Stabilization of Nanocrystalline Grain Size by Solute Addition: Part 1*.
[130] M. J. McCarthy and T. J. Rupert, *Shuffling Mode Competition Leads to Directionally Anisotropic Mobility of Faceted \ensuremath{\Sigma}11 Boundaries in Fcc Metals*, Phys. Rev. Mater. **4**, 113402 (2020).
[131] B. Wu, Z. Xie, J. Huang, J. Lin, Y. Yang, L. Jiang, J. Huang, G. Ye, C. Zhao, S. Yang, and B. Sa, *Microstructures and Thermodynamic Properties of High-Entropy Alloys CoCrCuFeNi*, Intermetallics **93**, 40 (2018).

[132] Y. F. Ye, Q. Wang, Y. L. Zhao, Q. F. He, J. Lu, and Y. Yang, *Elemental Segregation in Solid-Solution High-Entropy Alloys: Experiments and Modeling*, J. Alloys Compd. **681**, 167 (2016).
[133] N. Park, I. Watanabe, D. Terada, Y. Yokoyama, P. K. Liaw, and N. Tsuji, *Recrystallization Behavior of CoCrCuFeNi High-Entropy Alloy*, Metall. Mater. Trans. A **46**, 1481 (2015).
[134] X. W. Zhou, R. A. Johnson, and H. N. G. Wadley, *Misfit-Energy-Increasing Dislocations in Vapor-Deposited CoFe/NiFe Multilayers*, Phys. Rev. B **69**, 144113 (2004).
[135] P. Wynblatt and D. Chatain, *Anisotropy of Segregation at Grain Boundaries and Surfaces*, Metall. Mater. Trans. Phys. Metall. Mater. Sci. **37**, 2595 (2006).
[136] S. C. Middleburgh, D. M. King, G. R. Lumpkin, M. Cortie, and L. Edwards, *Segregation and Migration of Species in the CrCoFeNi High Entropy Alloy*, J. Alloys Compd. **599**, 179 (2014).
[137] H. Zhao, F. De Geuser, A. Kwiatkowski da Silva, A. Szczepaniak, B. Gault, D. Ponge, and D. Raabe, *Segregation Assisted Grain Boundary Precipitation in a Model Al-Zn-Mg-Cu Alloy*, Acta Mater. **156**, 318 (2018).
[138] B. P. Uberuaga, L. J. Vernon, E. Martinez, and A. F. Voter, *The Relationship between Grain Boundary Structure, Defect Mobility and Grain Boundary Sink Efficiency*, Sci. Rep. **5**, 1 (2015).
[139] C. Hu and Luo, Jian, *Deciphering Grain Boundary Properties in High-Entropy Alloys in a 5D Space Coupled Segregation and Disordering*, 2021 (n.d.).
[140] A. Ferrari, B. Dutta, K. Gubaev, Y. Ikeda, P. Srinivasan, B. Grabowski, and F. Körmann, *Frontiers in Atomistic Simulations of High Entropy Alloys*, J. Appl. Phys. **128**, 150901 (2020).
[141] J. M. Cowley, *An Approximate Theory of Order in Alloys*, Phys. Rev. **77**, 669 (1950).
[142] G. J. Tucker and D. L. McDowell, *Non-Equilibrium Grain Boundary Structure and Inelastic Deformation Using Atomistic Simulations*, Int. J. Plast. **27**, 841 (2011).
[143] M. Syha and D. Weygand, *A Generalized Vertex Dynamics Model for Grain Growth in Three Dimensions*, Model. Simul. Mater. Sci. Eng. **18**, 015010 (2010).
[144] M. Syha and D. Weygand, *Conditions for the Occurrence of Abnormal Grain Growth Studied by a 3 D Vertex Dynamics Model*, https://doi.org/10.4028/www.scientific.net/MSF.715-716.563.
[145] D. Weygand, Y. Bréchet, J. Lépinoux, and W. Gust, *Three-Dimensional Grain Growth: A Vertex Dynamics Simulation*, Philos. Mag. B **79**, 703 (1999).